The Report Committee for Adam James McMullen
Certifies that this is the approved version of the following report:

Study of Liquid-Coupled Ultrasonic Techniques to Evaluate Elastic Wave Propagation in Rocks

APPROVED BY
SUPERVISING COMMITTEE:

Supervisor:

Carlos Torres-Verdín

D. Nicolas Espinoza

Study of Liquid-Coupled Ultrasonic Techniques to Evaluate Elastic Wave Propagation in Rocks

by

Adam James McMullen

Report

Presented to the Faculty of the Graduate School of

The University of Texas at Austin

in Partial Fulfillment

of the Requirements

for the Degree of

Master of Science in Engineering

The University of Texas at Austin

August 2017

Dedication

Dedicated to my parents and sister, for their continuous love and support.

Acknowledgements

I would like to sincerely thank my supervisor, Dr. Carlos Torres-Verdín, for his sage advice and imparted wisdom throughout these past two years. Every weekly meeting has been a thought-provoking reflection into my own work and others, and his guidance was imperative to my continued intellectual development.

I would also like to thank Dr. Nicolas Espinoza for providing me with access to his laboratory equipment and for advising me along the way. You have helped me look at problems in a new light and provided the tools to my success.

Furthermore, I would like to thank Reynaldo Casanova for his very helpful logistical support. Many thanks for helping me with lab equipment acquisition and other administrative tasks.

Additionally, thanks to Amy Stewart for helping me with graduate timeline logistics. Thanks to Glen Baum, Gary Miscoe, and Daryl Nygaard for laboratory assistance and advice.

Special thanks to my peers in Dr. Torres-Verdín's group for their support and friendship. Thanks to Elsa Maalouf, Mohammed Bennis, Joshua Bautista, Colin Schroeder, Wilberth Herrera, Mathilde Luycx, David Medellin, Hyungjoo Lee, and others. Thanks to Roger Terzian for your excellent technical support.

And finally, thanks to my family and friends who have supported me along the way.

Abstract

Study of Liquid-Coupled Ultrasonic Techniques to Evaluate Elastic Wave Propagation in Rocks

Adam James McMullen

The University of Texas at Austin, 2017

Supervisor: Carlos Torres-Verdín

The development of new methods to measure core acoustic properties will improve understanding of reservoir geomechanical properties. Conventional acoustic analysis under triaxial press is often infeasible or impractical to perform along the entire core. Unconsolidated core samples in liners or cores extracted with pressure coring techniques present additional challenges. This work explores ultrasonic analysis of core samples subject to the previously mentioned constraints by immersing samples in liquid (water) and placing transducers adjacent to the sample at a given distance.

Modern pressure-coring ultrasonic sensors are capable of measuring P-wave velocity across the core diameter. This research explores this type of analysis with a focus on quality control effects of transducer-sample alignment. Further, this report studies a dual transducer array adjacent to the core sample to measure refracted P and S-wave velocities simultaneously. The methods are corroborated with forward models assuming a simplified 2D geometry to better understand the constraints of both systems and assist in data analysis.

Experiments are performed on cylindrical samples of aluminum, Berea sandstone, and Texas Cream limestone, with the rock samples studied while dry and fully water saturated.

The data for the cross-diameter P-wave analysis suggest that there is a minimum amount of fluid required to couple the energy to the sample and highlight the need to use transducers with small effective measurement areas to reduce the effects of sample curvature. Measurements on both dry and fully water saturated core samples agree with Gassmann's fluid substitution theory within a 2% error margin. Results from the refracted wave tests agree with the forward model, with all P and S-wave velocity estimates below 6% error. A second receiver spaced further away from the source simplifies isolation of relevant wave modes. Overall, forward model predictions agree with experimental results and show the potential of simultaneous P and S-wave measurement in the laboratory.

Table of Contents

List of Tables x

List of Figures xi

Chapter 1: Introduction 1

1.1 Motivation 1

1.2 Outline 3

Chapter 2: Literature Review 4

2.1 Elastic Properties and Gassmann's Equations 4

2.2 Ultrasonic Standards for Rock Measurements 6

2.3 Acoustic Measurement Techniques 8

Chapter 3: Laboratory Setup 11

3.1 Hardware 11

3.2 Quality Control 12

3.3 Prototype No. 1 – Transducer Pair Through Transmission 17

3.4 Prototype No. 2 – Transducer Pair Refraction 19

3.5 Prototype No. 3 – Array Refraction 20

3.6 Sample Preparation 22

Chapter 4: Numerical Modeling 25

4.1 Prototype No. 1 Model 25

4.2 Prototype No. 2 and 3 Model 31

Chapter 5: Experimental Results and Discussion 37

5.1 Prototype No. 1 – Aluminum Control 37

5.2 Prototype No. 1 – Dry and Water Saturated Cores 42

5.3 Prototype No. 3 – Aluminum Control 50

5.4 Prototype No. 3 – Dry and Water Saturated Cores 52

Chapter 6: Conclusions and Future Work 64

6.1 Conclusions 64

6.2 Future Work 65

Appendices....68
Appendix A: Aluminum waveforms, 2 in OD....68
Appendix B: Aluminum waveforms, 4 in OD....69
Appendix C: Dry Berea sandstone waveforms, 2 in OD....70
Appendix D: Dry Berea sandstone waveforms, 4 in OD....71
Appendix E: Saturated Berea sandstone waveforms, 2 in OD....72
Appendix F: Saturated Berea sandstone waveforms, 4 in OD....73
Appendix G: Dry Texas Cream limestone waveforms, 2 in OD....74
Appendix H: Dry Texas Cream limestone waveforms, 4 in OD....75
Appendix I: Saturated Texas Cream limestone waveforms, 2 in OD....76
Appendix J: Saturated Texas Cream limestone waveforms 4 in OD....77
References....78

List of Tables

Table 3.1: Summary of 2 in OD core porosity calculation parameters. 24

Table 5.1: Relevant experimental constants for Gassmann's equation application.....47

Table 5.2: Forward model inputs for 2 in and 4 in OD aluminum samples. 50

Table 5.3: Forward model inputs for 2 in and 4 in OD Berea sandstone cores. 53

Table 5.4: Forward model inputs for 2 in and 4 in OD Texas Cream limestone cores. 56

List of Figures

Figure 1.1: P-wave velocity analysis for pressure-cores using rolling transducers. The red transducer element is housed in an oil-filled elastic diaphragm that rotates and contours to the curvature of the core sample (Geotek). 2

Figure 2.1: Ultrasonic Testing equipment. Dashed boxed elements are optional (ASTM).7

Figure 2.2: Seismic Refraction survey and wireline acoustic logging tool diagrams (Stokoe et al., 2004). 8

Figure 2.3: Snell's Law at the borehole-formation interface (Haldorsen et al., 2006). 9

Figure 3.1: Test Setup with [1] Waveform Generator, [2] Optional Pulser, [3] Oscilloscope, [4] Optional Pre-Amplifier, and [5] P-Transducers. 11

Figure 3.2: Diagram explaining the importance of square signal pulse width. 13

Figure 3.3: P (a) and S-waves (b) as a function of pulse-width for one aluminum sample. The boxed plots show the optimal pulse-width selection. 13

Figure 3.4: P (a) and S (b) waveforms from 2 in OD aluminum samples of various length. Black and red dotted lines indicate P and S arrival times. 16

Figure 3.5: P and S-wave arrival time calibration data on aluminum. 17

Figure 3.6: Components of prototype No. 1. 18

Figure 3.7: Fully assembled prototype No. 1 with (a) 2 in sample holder and (b) an aluminum sample. 19

Figure 3.8: Prototype No. 2 (a) individual parts, (b) assembled and rotated 20°, and (c) with a 2 in OD aluminum sample. 20

Figure 3.9: Components of prototype No. 3 detailing the new brackets and base. 21

Figure 3.10: Assembled prototype No. 3 depicting 20° rotation with (a) no sample and (b) 2 in OD x 8 in long aluminum sample. 22

Figure 3.11: Aluminum 2024, Berea sandstone, and Texas Cream limestone samples. ...23
Figure 4.1: Prototype No. 1 experiment iteration showing both the general height offset axis H , and the transducer center height offset (independent variable) H_C 25
Figure 4.2: Prototype No. 1 (a) diagram indicating modeled quadrant and (b) forward model schematic.....26
Figure 4.3: Transducer separation (x_T) vs. center height offset for 2 in (a) and 4 in (b) OD samples. Separation is constant under 0.6 in of center height offset. 27
Figure 4.4: Travel time vs. height offset for (a) 2 in and (b) 4 in OD aluminum. 29
Figure 4.5: P-wave velocity estimation for aluminum as a function of height offset and center height offset for (a) 2 and (b) 4 in OD samples. 30
Figure 4.6: Aerial view of prototype No. 3 with dual receivers showing sketched refraction ray-traces and the constant transducer center distance.....32
Figure 4.7: Prototype No. 2 and 3 diagram (a) and schematic (b) for refracted wave modeling as a function of angle. 33
Figure 4.8: Arrival time vs. transducer angle for refracted P and S-waves in aluminum. The direct fluid arrival between the transducers is also shown. 34
Figure 4.9: Forward model velocity estimate vs. transducer angle for aluminum. Estimate is accurate between $\pm 3°$ of the critical angle. 35
Figure 5.1: Waveforms for 2 in OD aluminum as a function of center height offset (in). 37
Figure 5.2: Waveforms for 4 in OD aluminum as a function of center height offset (in). 38
Figure 5.3: Estimated P-wave velocity as a function of transducer center height offset for aluminum. 38
Figure 5.4: Forward model comparison of P-wave velocity estimate as a function of transducer height offset for (a) 2 and (b) 4 in OD aluminum. 40
Figure 5.5: Modeled origin of the first arrival energy from the transducer. 41

Figure 5.6: Dry (a) and fully water saturated (b) P-waveforms for 2 in OD Berea sandstone as a function of center height offset (in). 43
Figure 5.7: Dry (a) and fully water saturated (b) P-waveforms for 4 in OD Berea sandstone as a function of center height offset (in). 44
Figure 5.8: Dry (a) and fully water saturated (b) P-waveforms for 2 in OD Texas Cream limestone as a function of center height offset (in).....45
Figure 5.9: Dry (a) and fully water saturated (b) P-waveforms for 4 in OD Texas Cream limestone of center height offset (in). 46
Figure 5.10: Comparison of P-wave velocity estimate vs. center height offset for 2 and 4 in OD Berea sandstone (a) and Texas Cream limestone (b) cores. 48
Figure 5.11: Gassmann fluid substitution estimates from dry (air saturated) to fully water saturated for Berea sandstone (a) and Texas Cream limestone (b). 49
Figure 5.12: 2 in OD aluminum waveforms. P: Black, S: Red, Direct: Blue. 51
Figure 5.13: 4 in OD aluminum waveforms. P: Black, S: Red, Direct: Blue. 52
Figure 5.14: 2 in OD dry Berea waveforms. P: Black, S: Red, Direct: Blue.....53
Figure 5.15: 4 in OD dry Berea waveforms. P: Black, S: Red, Direct: Blue.....54
Figure 5.16: 2 in OD saturated Berea waveforms. P: Black, S: Red, Direct: Blue. 55
Figure 5.17: 4 in OD saturated Berea waveforms. P: Black, S: Red, Direct: Blue. 55
Figure 5.18: 2 in OD dry Texas Cream limestone waveforms. P: Black, S: Red, Direct: Blue. 56
Figure 5.19: 4 in OD dry Texas Cream limestone waveforms. P: Black, S: Red, Direct: Blue. 57
Figure 5.20: 2 in OD saturated Texas Cream limestone waveforms. P: Black, S: Red, Direct: Blue. 58

Figure 5.21: 4 in OD saturated Texas Cream limestone waveforms. P: Black, S: Red, Direct: Blue. 59
Figure 5.22: Comparison of the actual sample velocity with the experimental velocity acquired with prototype No. 3 using receiver one (a) and two (b).....61
Figure 5.23: Velocity estimate vs. arrival time error for all samples for both P and S-waves at each receiver. All measurements and velocity estimates are approximately within 5% of the true parameters. 63
Figure 6.1: Attenuation corrected reflection coefficient, R_P ,vs. incidence angle with Aki-Richards Approximation for 4 in OD (+) and 2x2x3 in rectangular prism (x) samples.....67

Chapter 1: Introduction

1.1 Motivation

Laboratory mechanical measurements characterize core sample dynamic elastic properties and improve understanding of reservoir mechanical properties. This is especially important for unconventional reservoirs, wherein completion design via hydraulic fracturing relies heavily upon the knowledge of the rocks stress state and elastic properties. Conventional ultrasonic testing is performed concurrently with triaxial stress testing in order to evaluate both the static and dynamic elastic properties of the sample. This type of testing requires the use of small core plugs, typically 1.5 inches in diameter by 3 inches in length (Kovari et al., 1983). Studying a small core plug from an already biased core sample with the intent to model reservoir scale properties is challenging. For this reason, downhole acoustic data is often the preferred method to estimate dynamic elastic properties, as the data better reflect the in-situ conditions that triaxial presses try to recreate. However, core data present the unique opportunity to improve insight into the dynamic elastic properties, as ultrasonic transducers allow for increased resolution of the acoustic properties. This is critical for understanding formation anisotropy and heterogeneity, which is often overlooked due to averaging effects present in downhole acoustic data, especially in thinly bedded formations. Thus, there is a need to evaluate the entire core sample non-destructively at the surface to provide detailed elastic property estimation. Systems already exist to evaluate the entire core sample P-wave velocity, such as in pressure-coring applications.

Pressure-coring technology, such as the HYACINTH system, allows for the study of samples at the surface while retaining in-situ pressures and temperatures (Schultheiss et al., 2008). This largely prevents degassing and fluid expansion, which preserves the samples in-situ state. Pressure coring techniques have also been applied to shale-gas

reservoirs to better evaluate total gas in place estimates (Cerri et al., 2015). At the surface, the system is able to measure gamma density, P-wave (primary or compressional) velocity, and take X-ray images. Of particular interest is that the P-wave measurements are taken tangent to the cylindrical core sample using complex rolling transducers. See Figure 1.1 for a depiction and description of modern acoustic rolling contact transducers used by Geotek Ltd.

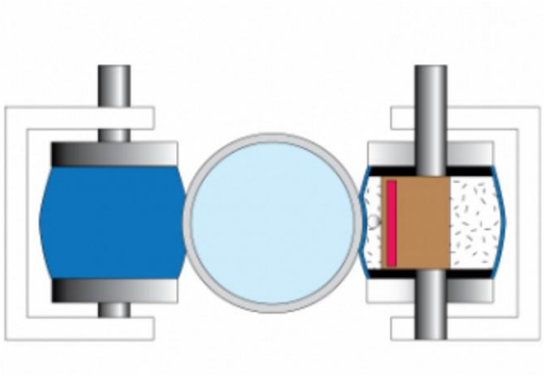

Figure 1.1: P-wave velocity analysis for pressure-cores using rolling transducers. The red transducer element is housed in an oil-filled elastic diaphragm that rotates and contours to the curvature of the core sample (Geotek).

P-wave analysis of cores in this geometry is non-standard, as most cylindrical cores handled at atmospheric conditions are analyzed with the transducers on the flat ends of the core plug (from here on referred to as conventional analysis). The pressure-coring setup allows for measurements to be made along the entire length of the core to generate a core log of P-wave velocity measurements.

The main goal of this research is to further probe the potential for ultrasonic velocity analysis of full cores. Not only will this complement the existing suite of acoustic core data, but also it may be applied to cores that are difficult to study conventionally. For example, conventional ultrasonic analysis is impractical inside a pressure coring vessel or

along an unconsolidated core in a liner. The transducers must be adjacent to the core for full core analysis (Yun et al., 2006).

First, the experiments analyze the accuracy of the aforementioned P-wave velocity analysis technique by changing the transducer height with respect to the sample. Second, the work explores an alternative method using multiple rotatable transducers in a dual receiver array to analyze the critically refracted P and converted S (shear) modes in the sample. Results of both are compared to a forward model simulation of arrival times based on the setup geometry and associated acoustic velocities of the samples.

1.2 Outline

Chapter 1 describes the initial motivation for the research. Chapter 2 consists of a literature review of pertinent information on the research topic. Chapter 3 details the laboratory setup and sample preparation methods. Chapter 4 discusses the numerical simulation methods for the forward models. Chapter 5 explains the experimental results. Chapter 6 concludes the work and highlights opportunities for future work.

Chapter 2: Literature Review

In this chapter, the homogenous, isotropic relations between acoustic velocity and dynamic elastic properties are presented. The difference between static and dynamic elastic moduli is explained, and Gassmann's equations are detailed to relate elastic properties of dry and water saturated rocks. Further, conventional ultrasonic analysis methodology and standardizations are shown, and the differences between laboratory and field acoustic data acquisition methods are highlighted.

2.1 Elastic Properties and Gassmann's Equations

Ultrasonic transducers allow for acoustic velocity and associated dynamic elastic properties estimation, such as the bulk modulus and shear modulus. Acoustic velocities measured in this work are the primary or compressional mode (P-wave) and secondary or shear mode (S-wave). P and S-wave particle displacement travel parallel and perpendicular to the direction of wave propagation, respectively. For an isotropic medium, these velocities are a function of the material density (ρ), bulk modulus (K), and shear modulus (μ), as shown below:

$$V_P = \sqrt{\frac{K + \frac{4}{3}\mu}{\rho}}, \tag{2.1}$$

$$V_S = \sqrt{\frac{\mu}{\rho}}. \tag{2.2}$$

The primary elastic properties of interest are the bulk modulus, shear modulus, and Poisson's ratio (ν) which are shown as functions of material density and acoustic velocity on the next page:

$$K = \rho\left(V_P^2 - \frac{4}{3}V_S^2\right), \tag{2.3}$$

$$\mu = \rho V_S^2, \tag{2.4}$$

$$\nu = \frac{V_P^2 - 2V_S^2}{2(V_P^2 - V_S^2)}. \tag{2.5}$$

These relations are often used to analyze the multitude of sources of acoustic data from the field, including seismic, wireline, and laboratory ultrasonic data.

Estimating rock elastic properties with acoustic measurements will result in dynamic elastic moduli. This refers to moduli estimates made using a high frequency (10^4 to 10^6 Hz) of stress excitation in the material. Static elastic moduli, for comparison, refer to moduli measured during a constant strain-rate loading experiment. Static moduli are measured at very low frequency (10^{-4} to 10^{-2} Hz). Typically, dynamic moduli over-estimate static moduli; this is likely due to changes in viscoelastic effects between the two frequency domains (Yale et al., 1994). This is not ideal, as static moduli better represent the true rock properties. However, dynamic estimates remain an effective way to estimate true static rock elastic moduli, and understanding their relation remains an active field of research.

In this work, various dry and water saturated cores are tested, with results corroborated using Gassmann's equations. Gassmann's equations assume that the rock is isotropic and homogenous, that there are no chemical effects between the pore fluid and matrix, and that the excitation frequency is low (10-100 Hz) (Berryman, 1999). The relations are as follows:

$$\frac{K_{sat}}{K_{\min} - K_{sat}} = \frac{K_{dry}}{K_{\min} - K_{dry}} + \frac{K_{fl}}{\phi(K_{\min} - K_{fl})}, \tag{2.6}$$

$$\mu_{sat} = \mu_{dry}\,. \tag{2.7}$$

The equations model the saturated rock bulk modulus as a coupling between the dry rock bulk modulus and porosity-weighted fluid bulk modulus. Further, they indicate that the shear modulus should be independent of the saturation. The dry rock properties refer to a rock with no fluid (liquid nor gas) in the pore space. Considering the difficulty and minimal benefit of measuring acoustic velocities in a vacuum chamber to eliminate adsorbed gas in the rock, this work assumes that air saturated rocks are dry. The rocks studied in this report are Berea sandstone and Texas Cream limestone. This work does neglect the low frequency assumption. Providing insight into the elastic moduli changes via Gassmann's equations is nevertheless a useful approximation.

2.2 Ultrasonic Standards for Rock Measurements

Conventional ultrasonic laboratory measurements are performed by attaching either P or S transducers to the flat faces of cylindrical core samples. Measurements of acoustic travel time are made via a through-transmission acoustic pulse that travels through the rock from the transmitter to receiver transducer. The American Section of the International Association for Testing Materials (ASTM) D2845 documentation provides a standardization for these type of measurements. Figure 2.1 displays the necessary hardware components for a standard test setup. The main components required are a pulse or signal

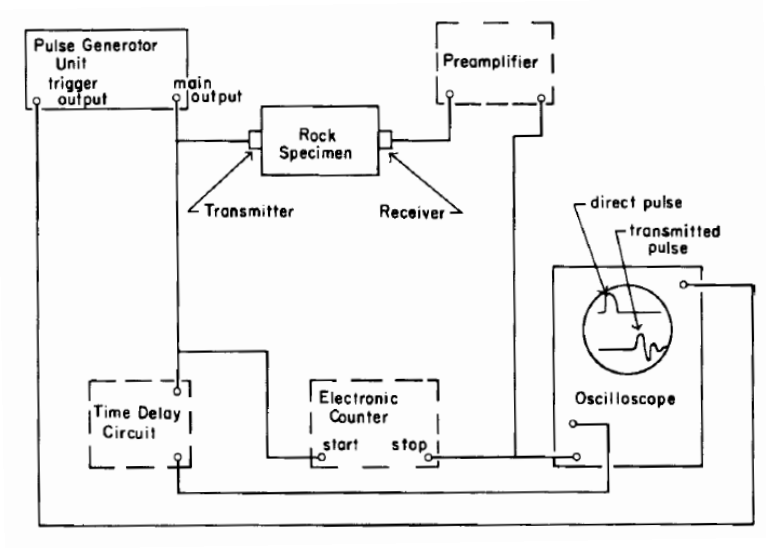

Figure 2.1: Ultrasonic Testing equipment. Dashed boxed elements are optional (ASTM).

The ASTM standardization provides guidelines on the relative size of the sample and incident wavelength of investigation. It states that the ratio of the sample length (L) to diameter (D) must be less than or equal to four, and that the sample diameter must be greater than five times the wavelength (λ) of propagation. And generally, the wavelength is equal to the speed of sound in the media ($c - V_P$ or V_S) divided by the frequency (f). The final relation is a fundamental aspect of the physics of wave propagation. These may be shown as:

$$\frac{L}{D} \leq 4, \tag{2.8}$$

$$D \geq 5\lambda, \tag{2.9}$$

$$\lambda = \frac{c}{f}. \tag{2.10}$$

These constraints are easily met for most standardized core sizes and ultrasonic transducer frequency ranges. However, lower frequency (larger wavelength) transducers may require larger diameter samples. These constraints are not directly applicable for non-conventional measurement techniques, but it is important to understand the interplay between the wavelength of investigation and sample size. Namely, that often times a larger sample is the preferred sample to test.

2.3 Acoustic Measurement Techniques

The focus of this work is on developing new laboratory techniques to analyze rock P and S-wave velocities. One way to accomplish this is to study measurement techniques that are often used in the field, but seldom in the laboratory. For instance, seismic surveys and wireline logging are dissimilar to conventional through-transmission ultrasonic analysis. Consider refraction surveys and multiple receiver acoustic logging techniques. Both methods utilize the physics of refraction and mode conversion, which occurs at the interface between different media. In a refraction survey, the interfaces refer to those between the multitude of subsurface layers that may be resolved using low frequency seismic measurements, so long as the subsequent layer velocity is faster.

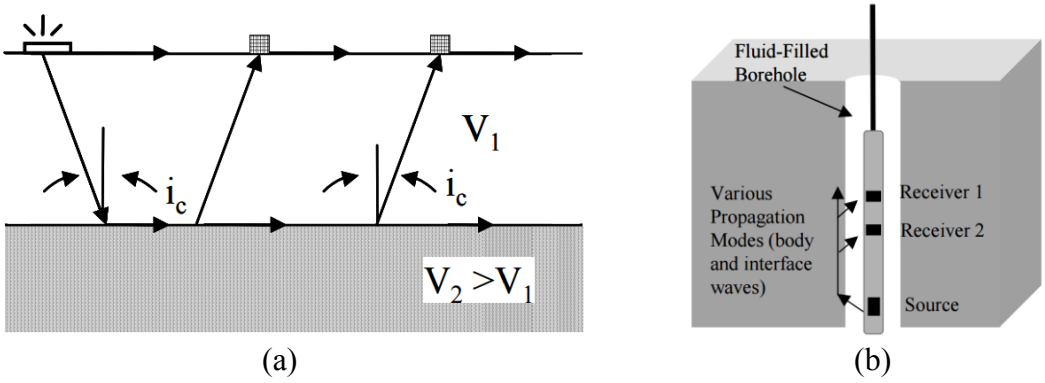

Figure 2.2: Seismic Refraction survey and wireline acoustic logging tool diagrams (Stokoe et al., 2004).

Figure 2.2a details the critically refracted P-wave travelling approximately along the interface between the two media. In reality, the critically refracted mode will travel within the second layer.

In a wireline tool (Figure 2.2b), the interface is between a fluid-filled borehole and the formation. This introduces refracted, reflected, surface, and direct modes. In both systems, interactions are governed by Snell's Law, which explains how the source P-wave will refract in the formation at specific angles as a function of the layer velocities and incident angle. Figure 2.3 illustrates this phenomenon in a borehole environment, with the Snell's Law relation on the bottom of the figure. The diagram is a two-dimensional simplification of borehole acoustics and intends to represent the idealized plane-waves that would exist at a perfectly flat interface.

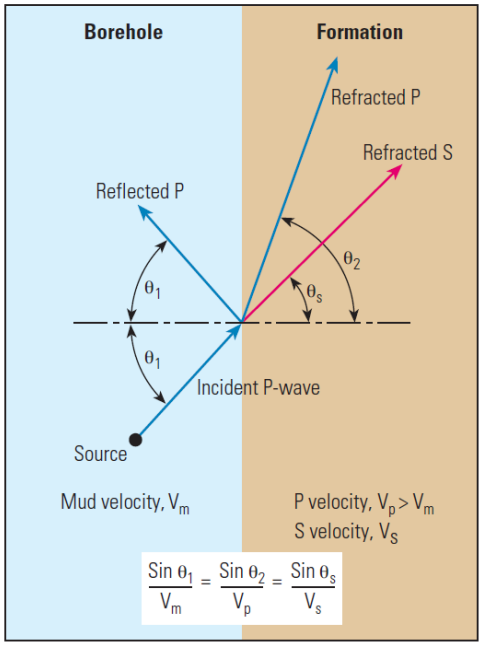

Figure 2.3: Snell's Law at the borehole-formation interface (Haldorsen et al., 2006).

In terms of arrival times, the P-wave will arrive first, followed by the S-wave. Various borehole guided modes may exist after S-wave arrivals. These refer to the reflected

(borehole guided) and direct mode in the fluid. These modes are not always seen on conventional logs, as they depend on borehole conditions. Next, leaky surface waves, known as Stoneley waves, propagate along the borehole wall and arrive after the S-wave. The Stoneley wave is not typically used to estimate formation velocities, and is of minimal relevance to this work.

To capitalize on the fundamentals of borehole acoustics and refraction, this work will present the development of a transducer array system that treats the sample as an inverted borehole, in which the sample is immersed in water and the transducers are external to the sample. Chapter 3 will detail this laboratory setup and the iterative design changes involved in its creation and optimization.

Chapter 3: Laboratory Setup

This chapter details the laboratory equipment required to perform ultrasonic analysis. Additionally, quality control techniques and newly developed prototype equipment are detailed. The test sample preparation methodology is also explained.

3.1 Hardware

The main components used for ultrasonic analysis correspond to those described in the ASTM standard. Two signal generators, an Olympus 5072 PR ultrasonic pulser/receiver unit and a Keysight 33210A waveform generator, were tested for signal quality. The ultrasonic pulser is capable of generating larger amplitude signals than the waveform generator, but was determined to produce a less uniform frequency composition in the waveforms. The waveform generator was relatively sufficient for all experimental procedures. A Krohn-Hite Model 3364 filter and pre-amplifier was optionally available. Lastly, a Keysight DSOX2024A Oscilloscope was used to capture and export all recorded waveform data via USB.

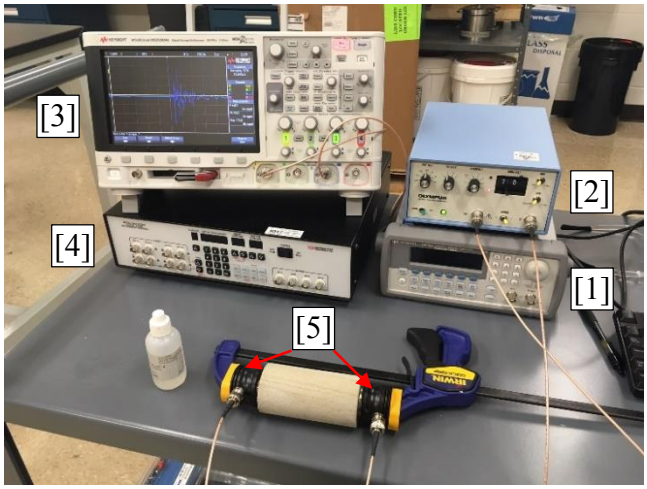

Figure 3.1: Test Setup with [1] Waveform Generator, [2] Optional Pulser, [3] Oscilloscope, [4] Optional Pre-Amplifier, and [5] P-Transducers.

Figure 3.1 shows the equipment setup conventionally for through transmission analysis with a small core sample and a pair of Olympus V101 0.5 MHz P transducers held together via a clamp. Note that this figure shows the use of the pulser, and that all experiments shown were conducted with the waveform generator. These components were all necessary to have in case a test signal from the waveform generator was of insufficient power.

The small bottle in Figure 3.1 is an ultrasonic couplant, glycerin, that was originally used for proper transducers coupling to rocks for conventional testing. Later testing revealed that honey was a much more ideal and readily available couplant, as inspired by previous research (Weidinger, 2008). The use of honey was greatly beneficial for conventional testing with the Olympus V150 0.25 MHz shear transducers. Both the P and S transducers were used to measure benchmark conventional P and S velocities for all samples tested. Since these transducers operate at different frequencies, the input pulse time to excite the transducer corresponds to the resonant frequency to increase the output of the system. This will be discussed in the next section.

3.2 Quality Control

A square wave is an ideal wavelet to send due to its fast rise time. Since the P transducer operates at 0.5 MHz, the pulse width time (W) should correspond to the inverse of half the resonant frequency (ω) of the transducer. Further, the period (T) must therefore be twice the pulse width. Figure 3.2 shows a diagram and equation explaining this logic. This approach was validated by studying test signals of different pulse widths on aluminum.

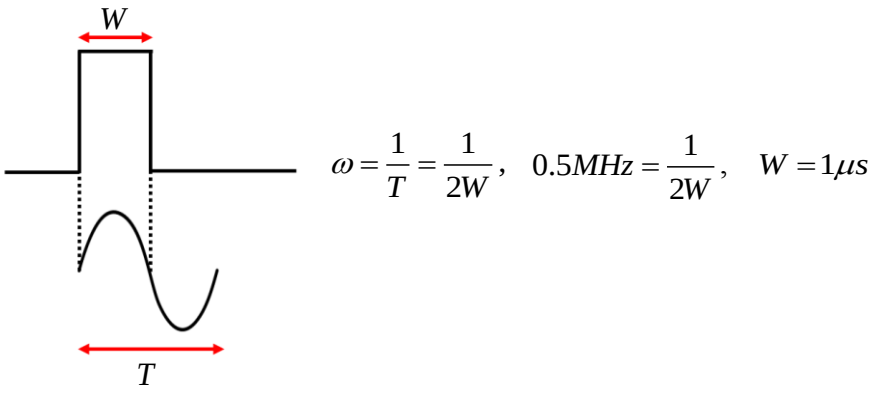

Figure 3.2: Diagram explaining the importance of square signal pulse width.

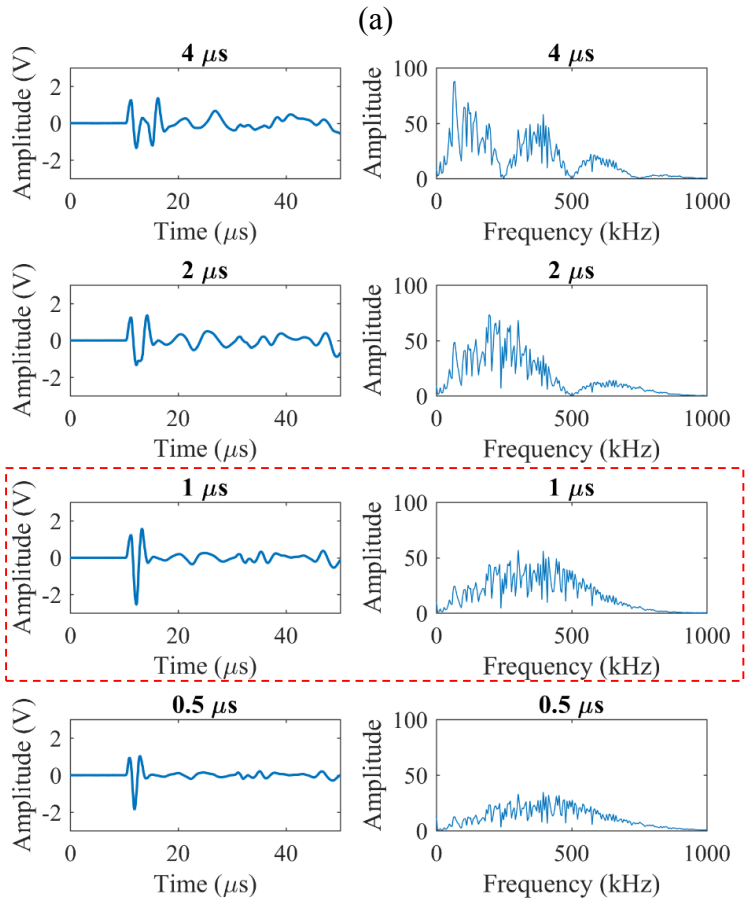

Figure 3.3: P (a) and S-waves (b) as a function of pulse-width for one aluminum sample. The boxed plots show the optimal pulse-width selection.

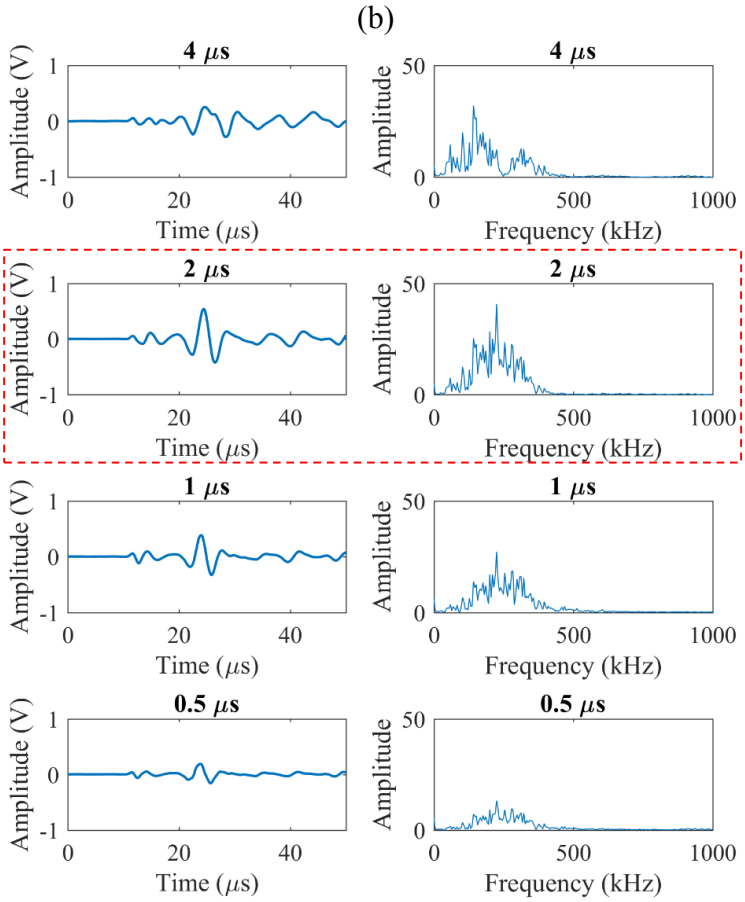

Figure 3.3 continued.

Figure 3.3 shows P and S transducer data on a 4 in outer diameter (OD) by 64 mm long aluminum sample. A pulse width that corresponds to the transducer resonance consistently generated the largest amplitude and most uniform frequency response. This is 1 μs for the P transducer, and 2 μs for the S transducer. Both of which correspond to 0.5 MHz and 0.25 MHz, respectively, which are the rated resonance frequencies of these transducers.

Additionally, the system characteristic lag time may be evaluated with aluminum samples to properly calibrate arrival time selection. Six cylindrical aluminum samples of various lengths were measured. Resulting waveforms are shown in Figure 3.4. The visually

selected P-arrival times are shown with black dotted lines, and S-arrival times are shown with red dotted lines. Note the difficulty of selecting S-arrival times for lengths less than L3 (~75 mm). This is because shorter samples make it difficult to distinguish the change in arrival time from P to S. All selected S-arrivals intersect the waveform at zero amplitude for accuracy.

Arrival time data are plotted against sample length in Figure 3.5. This shows P transducer reliability and slight S transducer uncertainty. Linear regression slopes correspond to the P and S velocities: 6,329 and 3,135 m/s, respectively. These values agree with the literature values of 6,320 and 3,150 m/s for aluminum (Ultrasonic Velocity Table). While the y-intercept of the S data is not useful, the accuracy of the P measurements provides a reliable y-intercept that corresponds to the characteristic system lag-time of 39 ns. This is negligible, but still important to quantify.

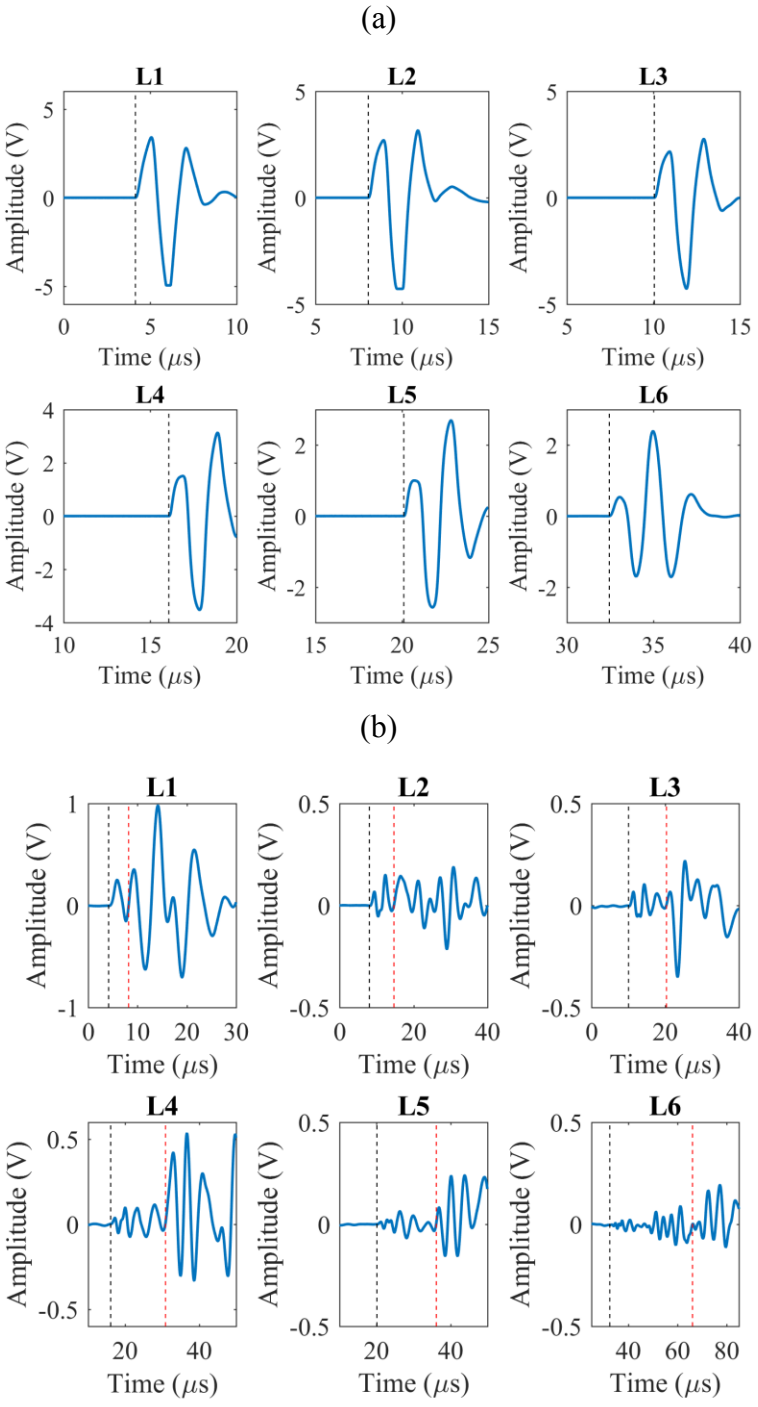

Figure 3.4: P (a) and S (b) waveforms from 2 in OD aluminum samples of various length. Black and red dotted lines indicate P and S arrival times.

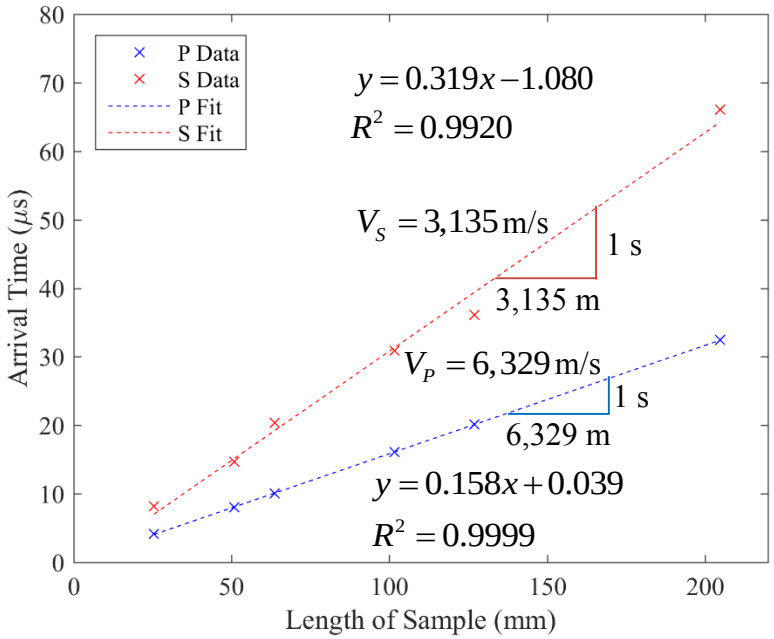

Figure 3.5: P and S-wave arrival time calibration data on aluminum.

3.3 Prototype No. 1 – Transducer Pair Through Transmission

A system of 3D printed parts were developed to hold the transducers in place and ensure their alignment when tangent to the sample. All parts were designed in the AutoDesk Fusion 360 CAD environment, and they were printed out of PLA plastic using a SeeMeCNC Rostock Max v3 printer. The original system consists of a set of transducer holders which are mounted on brackets with a counter-sunk 10-24 machine screw, washer, and nut. This allows the user to adjust the transducer center height. These brackets are then aligned using a sample base that also functions as a sample mount holder. Figure 3.6 shows all of the components. The system frequently makes use of tapered sliding joints that allow for linear translation. This is to simplify user operation for adjusting transducer alignment. Figure 3.7 shows the assembled system without and with a 2 in OD aluminum sample. Since the smallest diameter samples tested are 2 in, the default resting center height of the transducers is designed to correspond to 1 in, i.e., the sample mid-plane for a 2 in OD

sample. This greatly simplifies operation, and adjustments in height are readily made via caliper. The nut can be tightened by hand, and the system is easy to implement or assemble submerged in water, as is the case for all experiments. Water is used to properly couple the transducers to the outer diameter of the sample because a tangent contact in air does not readily transmit ultrasonic energy through the sample.

Prototype No. 1 is used to evaluate modern pressure-core P-wave arrival time estimation techniques. Namely, the effect of changing the height on sample velocity estimation is evaluated. This is important because currently there are minimal standardizations that exist for examining acoustic velocity in this manner.

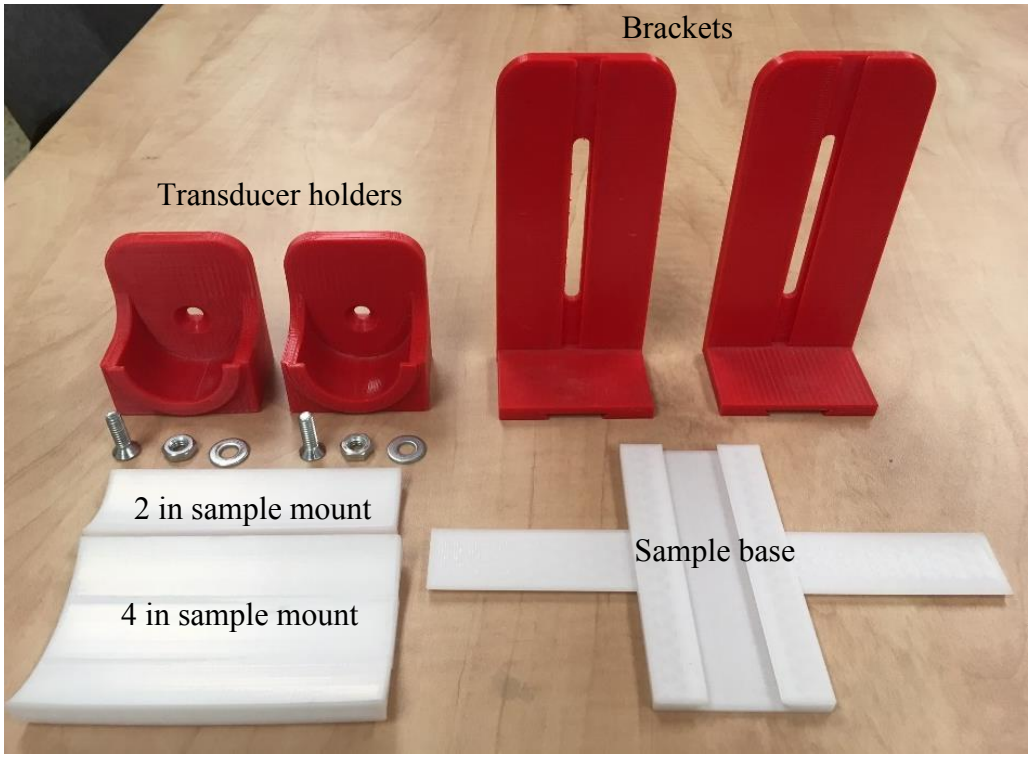

Figure 3.6: Components of prototype No. 1.

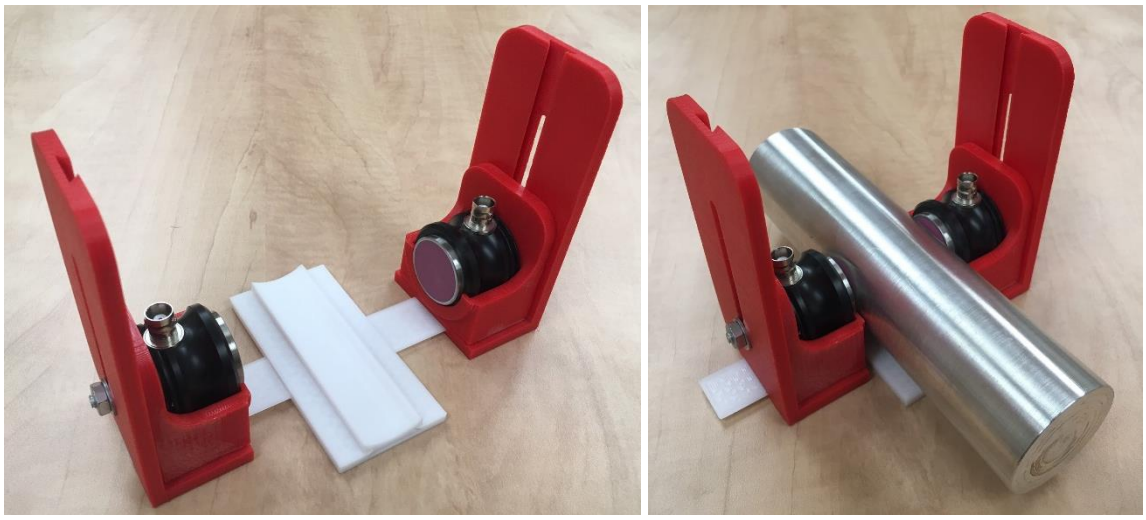

(a) (b)

Figure 3.7: Fully assembled prototype No. 1 with (a) 2 in sample holder and (b) an aluminum sample.

3.4 Prototype No. 2 – Transducer Pair Refraction

A modification to the prototype No. 1 was developed to allow the transducers to rotate adjacent to the sample and probe for refracted and converted waves. This prototype uses round inserts that connect with the previously described brackets (Figure 3.8a). Slight tolerances between the inserts and new base allow them to rotate freely once assembled. The new sample base only has a connection on one side. A series of indents that correspond to 5° increments are designed on angle indicator rings that attach onto the base. These indents are colored with a black marker for clarity. The left and right inserts are marked after the system was fully assembled for the first time and transducer alignment was calibrated. A small mark on the insert front edge is associated with this calibration, and it allows for modification of the incident angle by aligning the mark with the angles indicated.

Figure 3.8b shows the assembled prototype with both transducers rotated 20°, as shown with the zoom of the insert mark aligning with the 20° mark. Figure 3.8c shows a 2 in OD aluminum sample ready for testing. The system allows for adjustment of the sample

to transducer distance. This is useful for avoiding the onset of reflected waves (if desired); the closer the sample, the higher the angle required to induce reflected waves. One major drawback is that the rotation joint causes the transducer center point to follow an arc. Ideally, the transducer center distance would be fixed. This slightly complicates forward modeling of the system, but it can be measured and accounted for. Additionally, the distance between the transducers is fixed by the base. The final prototype addresses both of these issues.

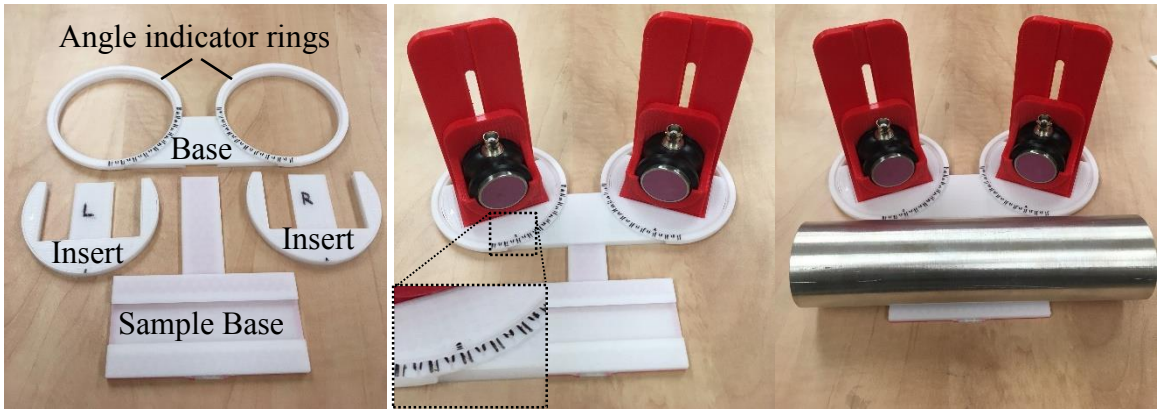

(a) (b) (c)

Figure 3.8: Prototype No. 2 (a) individual parts, (b) assembled and rotated 20°, and (c) with a 2 in OD aluminum sample.

3.5 Prototype No. 3 – Array Refraction

Drawing on the lessons learned from the previous prototype, prototype No. 3 consists of new brackets that allow transducer rotation to occur precisely at the transducer center point. Figure 3.9 shows the individual components of prototype No. 3. The brackets have a physical dial as opposed to a mark, and they also have increased structural rigidity due to an improved edge fillet. The new base consists of two parts, the primary base which connects to the sample holder, and the secondary base which can slide further from the primary if desired. Rotation markings are built into the new base and are similarly marked.

The base has three cylindrical standoffs that connect to the brackets. The left and center standoffs are 100 mm apart, and the right standoff is by default 100 mm from the center. This standoff distance may be increased up to 200 mm. The dotted line between the primary and secondary base shows the difficult to see interface between the two separate parts. Experiments were run in the default configuration as this is designed effectively for 8 in long samples. Figure 3.10a shows the assembled system with three P transducers.

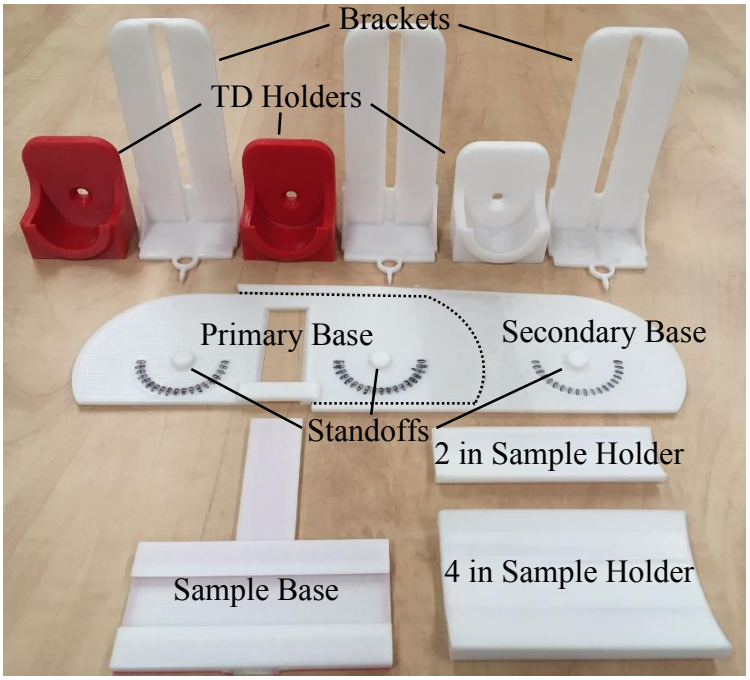

Figure 3.9: Components of prototype No. 3 detailing the new brackets and base.

All transducers are rotated 20°, with the two on the left acting as receivers and the one on the right as the transmitter. Figure 3.10b depicts a typical iteration of a test setup for an 8 in long sample. The system is capable of testing angles up to 65° using both receivers. By removing the middle transducer, prototype No. 3 effectively behaves as an optimized prototype No. 2.

(a) (b)

Figure 3.10: Assembled prototype No. 3 depicting 20° rotation with (a) no sample and (b) 2 in OD x 8 in long aluminum sample.

3.6 Sample Preparation

All experiments were performed on the following materials: Aluminum 2024, Berea sandstone, and Texas Cream limestone. The samples of each material are approximately 2 and 4 in OD by 8 in length. The samples are shown in Figure 3.11. The aluminum functions as an ideal homogenous, isotropic media that is used as a control. The sample length is important for testing with prototype No. 3, but inconsequential for testing with prototype No. 1. Namely, the transducer size and resulting size of prototype No. 3 dictate the use of relatively long samples.

The rock samples were tested dry and fully water saturated. The samples were dried in an oven for 48 hours prior to any testing or water saturation procedure. Granted, all testing requires the samples to be submerged in water. But the testing of the dry samples took place fast enough to avoid significant spontaneous water saturation interference. To create fully water saturated cores, the 1998 API Recommended Practices for Core Analysis liquid saturation guidelines were followed. Namely, after drying, the cores were placed under hard vacuum for 12 hours to rid them of any adsorbed air.

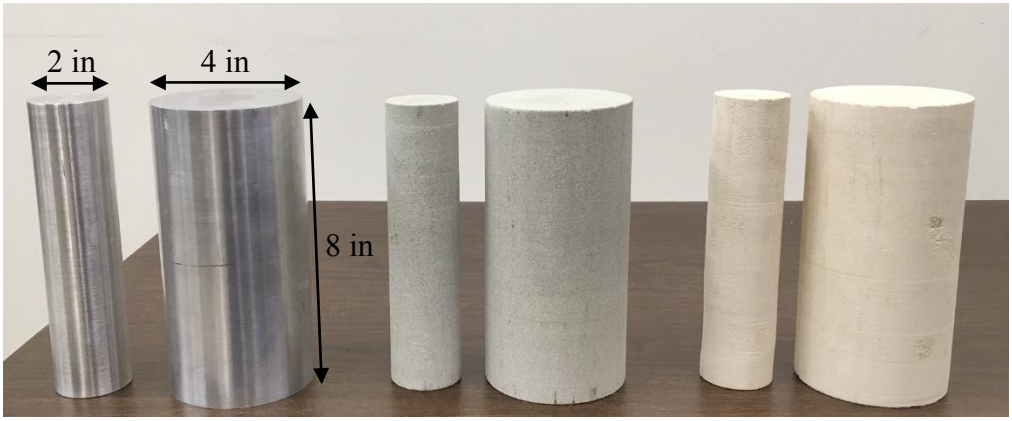

Figure 3.11: Aluminum 2024, Berea sandstone, and Texas Cream limestone samples.

Deaerated water was then introduced into the system under vacuum until the sample was fully submerged, and the vacuum was continued for one hour. Then, the sample was returned to atmospheric pressure for another 4 hours (API, 1998).

Dry and water saturated bulk densities are estimated by measuring the dried weight, water saturated weight, and volume (sample dimensions). Porosity is then determined via the following relation,

$$\phi = \frac{\rho_{mat} - \rho_b}{\rho_{mat} - \rho_f}. \tag{3.1}$$

This was performed for the 2 in OD samples, as the 4 in OD samples were too heavy to be weighed precisely with the existing laboratory scales. The data are summarized in Table 3.1, with fluid density set to zero for the dry case and 1 g/cc for the fully water saturated case. The matrix density is calculated by assuming that dry and water saturated porosity are equal, that is:

$$\phi_{dry} = \frac{\rho_{mat} - \rho_{b,dry}}{\rho_{mat}} = \frac{\rho_{mat} - \rho_{b,sat}}{\rho_{mat} - 1} = \phi_{sat}. \tag{3.2}$$

The matrix densities are close to that of pure quartz (2.65 g/cc) and limestone (2.71 g/cc). This validates the results.

Sample	$M_{dry}(g)$	$M_{sat}(g)$	V (cc)	$\rho_{b,dry}$ (g/cc)	$\rho_{b,\text{sat}}$ (g/cc)	ρ_{mat} (g/cc)	Φ (%)
Berea sandstone	841.72	924.74	403.25	2.09	2.29	2.61	19.90
Texas Cream limestone	770.97	885.95	401.81	1.92	2.20	2.67	28.12

Table 3.1: Summary of 2 in OD core porosity calculation parameters.

Chapter 4: Numerical Modeling

This chapter details the 2D forward models used to evaluate the experimental data. The models predict the refracted wave ray-path travel time as a function of fluid and sample velocities and system geometry.

4.1 Prototype No. 1 Model

Prototype No. 1 estimates P-velocity across the sample diameter. To evaluate the effectiveness of this technique, experiments will change the transducer center height offset, H_C, with respect to the sample. The more general height above the sample mid-plane will be referred to as the height offset or y-axis height, y (Figure 4.1). The experiments start with the transducer center axis aligned to the sample mid-plane, and experiments are conducted in transducer center height offset increments of 0.2 in until the transducer center axis is tangent to the top of the sample. Figure 4.1 depicts the experimental setup with a 4 in OD Texas Cream core. The transducer faces are pressed against the core at each height increment, which reduces the separation distance between the transducers with increasing height.

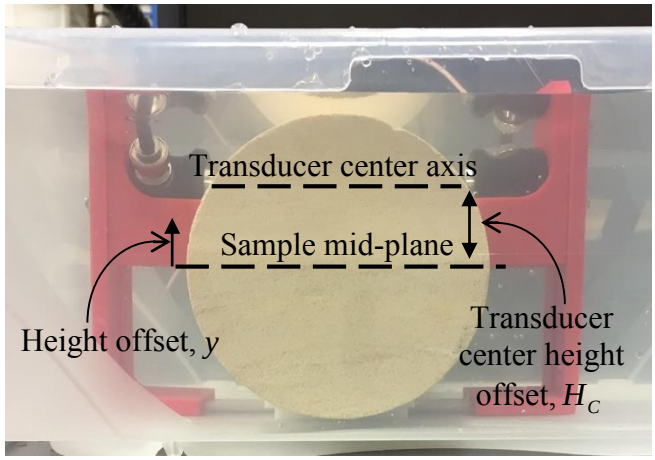

Figure 4.1: Prototype No. 1 experiment iteration showing both the general height offset axis H, and the transducer center height offset (independent variable) H_C.

The forward model assumes a simplified 2D system geometry and calculates the transducer separation distance as a function of center height offset. The model treats the transducer face as a collection of point sources and determines the critical incident angles at which a waveform will travel parallel to the mid-plane. This is done because this waveform is the fastest to travel between the transducers. Figure 4.2 depicts a schematic of the model. For a given transducer center height offset, there will be a range of height offsets that acoustic energy will emanate from; that is, $H_C \pm (d/2)$.

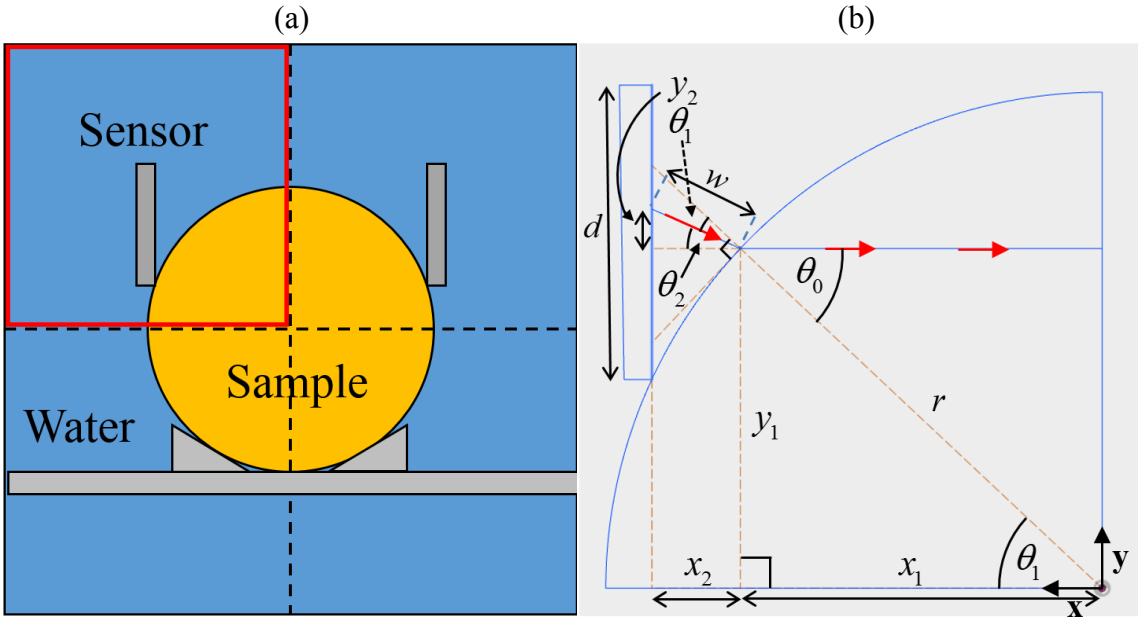

Figure 4.2: Prototype No. 1 (a) diagram indicating modeled quadrant and (b) forward model schematic.

Model inputs are the P-wave velocity in water and the sample, and the dimensions of the system. The model then varies the location of the transducer face assuming a sample contact constraint occurs at the bottom of the transducer. A point source of sound is simulated to originate across the entire transducer face of height d, and the model solves for the corresponding θ_0 from each point. The model then calculates the half-distance travelled in water (w) and the half distance travelled in the sample (x_1). Based on these

distances, a composite arrival time can be determined. A velocity estimate is made by dividing the total transducer separation ($x_T = 2(x_1 + x_2)$) by the arrival time.

(a)

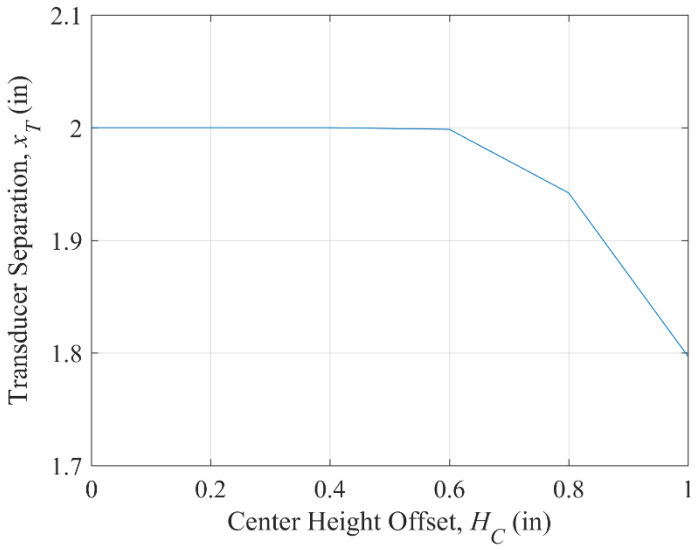

(b)

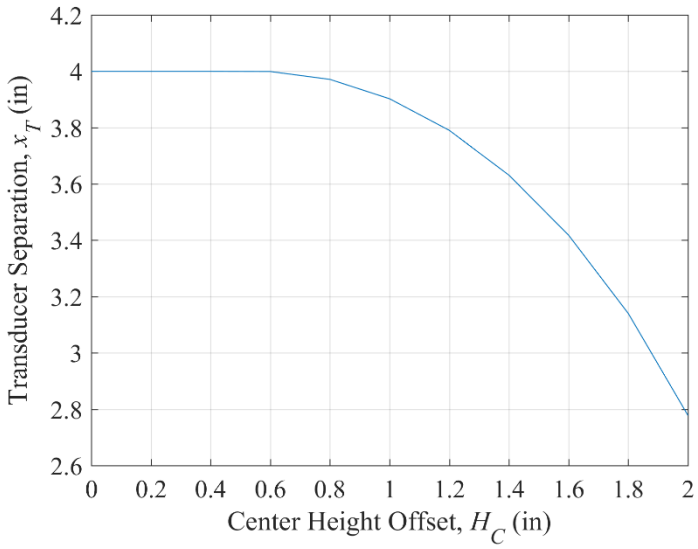

Figure 4.3: Transducer separation (x_T) vs. center height offset for 2 in (a) and 4 in (b) OD samples. Separation is constant under 0.6 in of center height offset.

Note that the transducer contact constraint means that the transducer will be tangent to the sample until the height increase is greater than half of the transducer height. Figure 4.3 shows the reduction in transducer separation as a function of transducer center height offset for both 2 and 4 in OD samples. Figure 4.3a is not smooth because experimentally the height will only increase by increments of 0.2 in. Thus, we expect the transducers to be perfectly tangent to the samples at height offsets from 0 to 0.6 in.

For demonstration, we apply the model on a sample of aluminum with $V_P = 6330$ m/s and water velocity $V_W = 1483\,\text{m/s}$. The simulation generates plots showing a distribution of arrival times, as in Figure 4.4 on the next page. The legend refers to the transducer center height offset, H_C, in inches. Since the circular transducer face is roughly 1.25 inches in diameter, the plots show how the maximum height above the sample mid-plane, y, is approximately 0.625 in when the center height offset is zero. Note that the potential error in travel time is reduced for the larger diameter sample, as locally a large diameter will better approximate a planar interface and reduce the presence of water between the sample and transducer. The transducer will continue to be tangent to the sample until the center height offset is 0.8 in, at which the curves begin to spread apart because the separation distance between the transducers is decreasing. This is not significant until the center height offset is 1 in or greater, as shown in the light blue lines in Figures 4.4a and 4.4b.

Interestingly, as H_C increases, travel time estimates diverge. The decrease in arrival time occurs because the total transducer separation distance is decreasing and less of the sample is measured; i.e., the bottom-most point of the transducer essentially transmits a non-refracted wave straight through the sample. However, the upper-most portion of the transducer engages more water, which has a much lower velocity than aluminum.

(a)

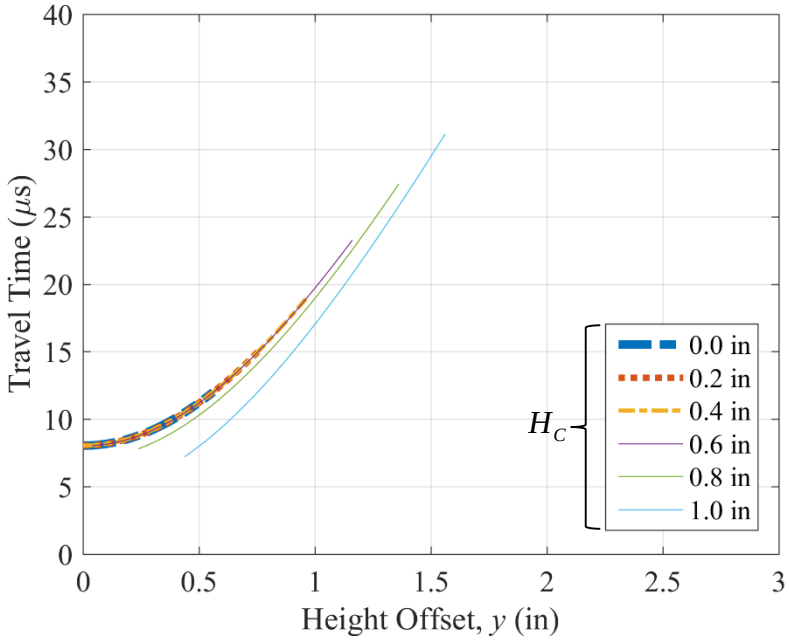

(b)

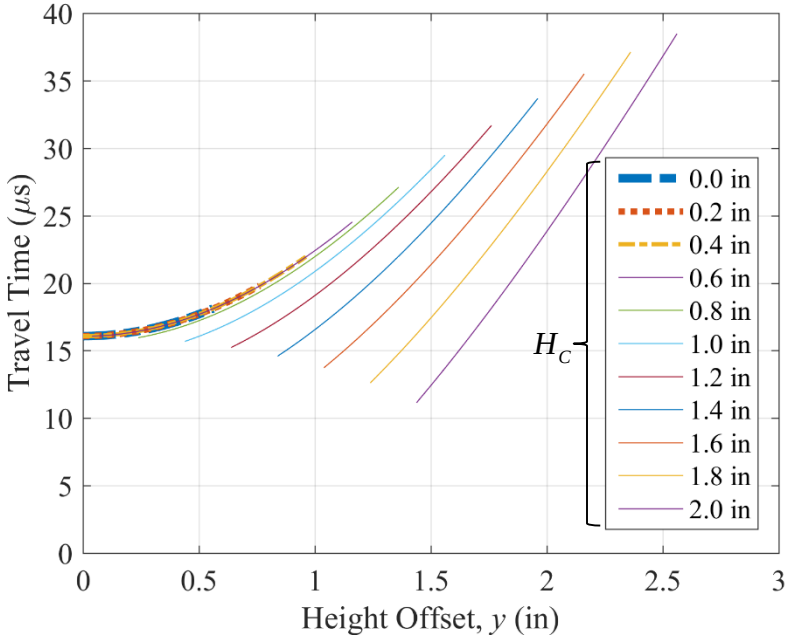

Figure 4.4: Travel time vs. height offset for (a) 2 in and (b) 4 in OD aluminum.

(a)

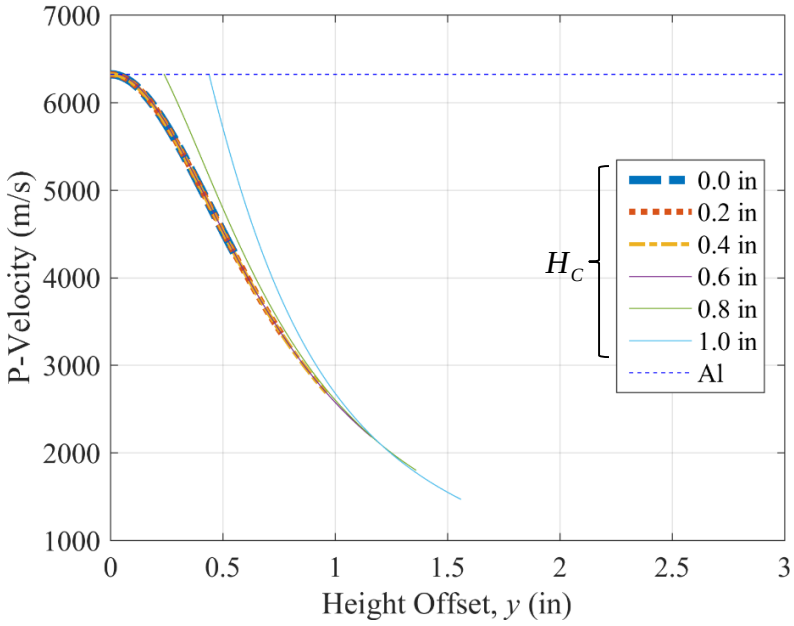

(b)

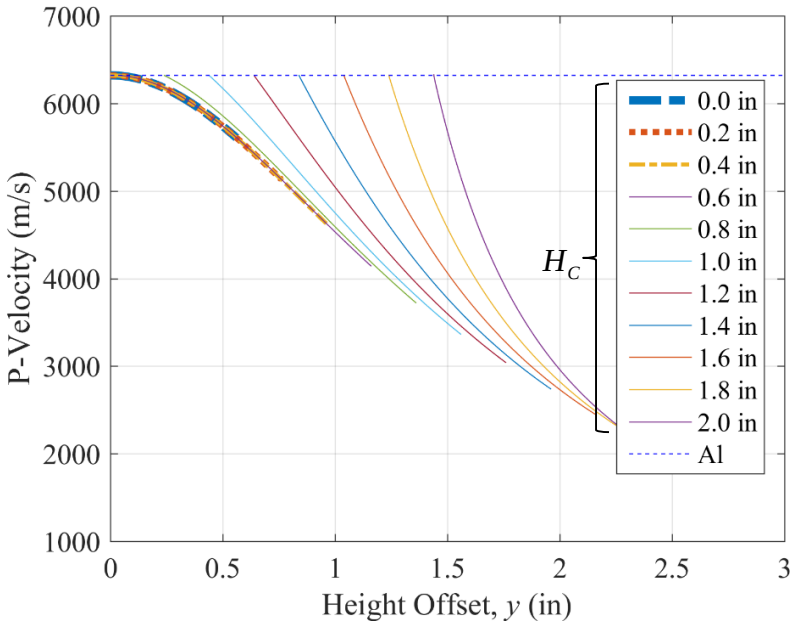

Figure 4.5: P-wave velocity estimation for aluminum as a function of height offset and center height offset for (a) 2 and (b) 4 in OD samples.

Thus, the resulting arrival time will depend on how evenly the transducer transmits energy from its face. This will be evaluated with the laboratory data in Chapter 5.

The P-wave velocity estimates are determined assuming the user only measures the total transducer separation, not the total distance travelled by a critically refracted ray path. This is a reasonable approximation, especially for small θ_0. Figure 4.5 shows these estimates. The model shows that at any height offset, y, it is possible to measure the correct velocity (intersection of dashed line and solid lines)—but this would only occur if there is significant energy transferred at the transducer-sample contact, which is unlikely because some fluid is required to couple the energy to the sample. Even though this shows a distribution of velocity estimates, in reality there will only be a single arrival time and calculated velocity for each center height offset, H_C. As center height offset increases, the range in velocity estimates increases due to the previously discussed divergence of arrival times. A priori, the simulations indicate that the most ideal testing geometry is with the transducer aligned to the mid-plane of the sample. This makes realistic sense, as this geometry minimizes the distance travelled in water. Further, the simulations show the benefit of using a larger diameter sample.

4.2 Prototype No. 2 and 3 Model

Both refracted wave prototypes rely on the same principles that were used to model the prototype No. 1. The main difference is that analyzing this system requires observation of the entire wave train, not just the first arrival. The model discussed is applicable to the single receiver configuration of prototype No. 2, and both the single and dual receiver configuration of prototype No. 3. In this system, the transducer center height is at the sample mid-plane for all samples. Figure 4.6 shows an aerial view of prototype No. 3 in the dual receiver configuration with a 2 in OD by 8 in long aluminum sample. Transducer

rotation occurs at the transducer center, and therefore the transducer center to sample distance is constant. The transducer center spacing distance is also constant.

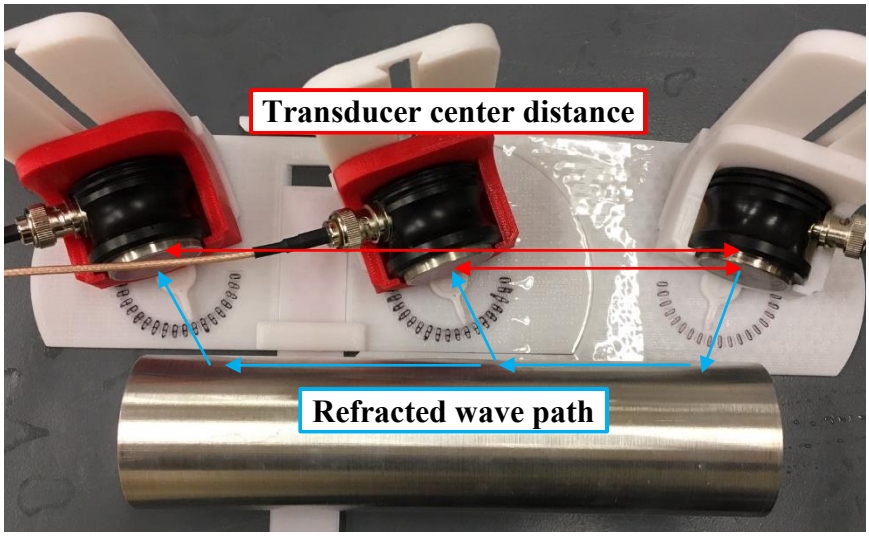

Figure 4.6: Aerial view of prototype No. 3 with dual receivers showing sketched refraction ray-traces and the constant transducer center distance.

By assuming that both transmitter and receiver(s) are rotated at the same incident angle, the system geometry can be greatly simplified. Only half of the system needs modeling, similar to the prototype No. 1 model. This system does not need to take into account transducer height changes; the transducer center height offset is set to zero. However, the model must take into account the converted S-wave. Figure 4.7 shows a sketch of a transducer face with the center separated a distance x_1 and y_1 from the origin. The dark grey represents the sample, and the blue lines between the sample and transducer face correspond to the critical P and S-wave ray traces that originate from the left, center, and right of the transducer at critical angles θ_{pc} and θ_{sc}. In reality, they will originate across the entire transducer face. The red and green arrows indicate the path of the critical P and S-waves from the transducer center.

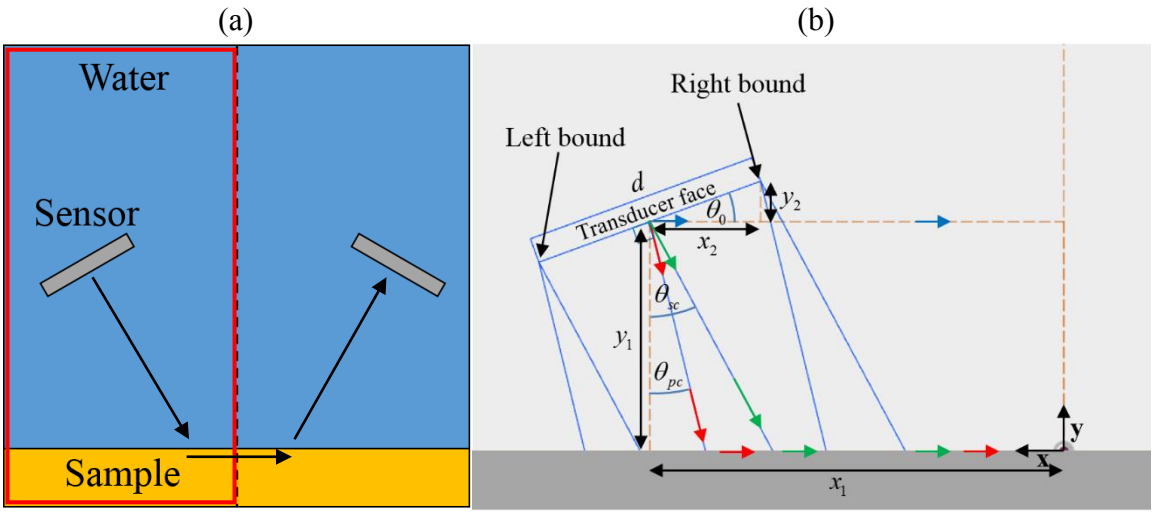

Figure 4.7: Prototype No. 2 and 3 diagram (a) and schematic (b) for refracted wave modeling as a function of angle.

The assumption is made that at every point along the transducer face, in 2D, a circular wave front propagates out from the transducer. At all angles θ_0 from 0 to 90°, there will therefore be some energy transmitted at the critical angle. The transducer x and y offset (x_2 and y_2) from the transducer center must be calculated at each θ_0 to determine the left and right sensor boundary points for the model. These boundary points allow for the calculation of a range of arrival times as a function of the distance travelled in the water and sample. Further, the model calculates the arrival time of a direct fluid mode propagating parallel to the sample (blue arrows). This is important to monitor for quality control purposes, as depending on the distance between the transducers and the sample, sometimes this wave front may arrive first. This is only modeled directly between the transmitter and receiver. When two receivers are used, the middle receiver interrupts the transit of the direct fluid mode to the second receiver.

Consider an aluminum sample with $V_P = 6330$ m/s and $V_S = 3135$ m/s immersed in water with $V_W = 1483$ m/s. The half-distance between the receivers, x_1, is 50 mm, and

the separation between the transducer center and sample, y_1, is 25 mm. Based on the ratio of the velocities, Snell's Law predicts critical angles of 13.6° and 28.3° for refracted P and S-waves, respectively. With an effective transducer length of 28.5 mm (d), the following variation in predictive ability will result. Figure 4.8 shows arrival time as a function of transducer rotation, θ_0. Focus on the center P-wave arrival (P). The critically refracted P-wave from the transducer center always arrives at the same time because the transducer center is fixed during rotation. The same is true for the S-wave (S).

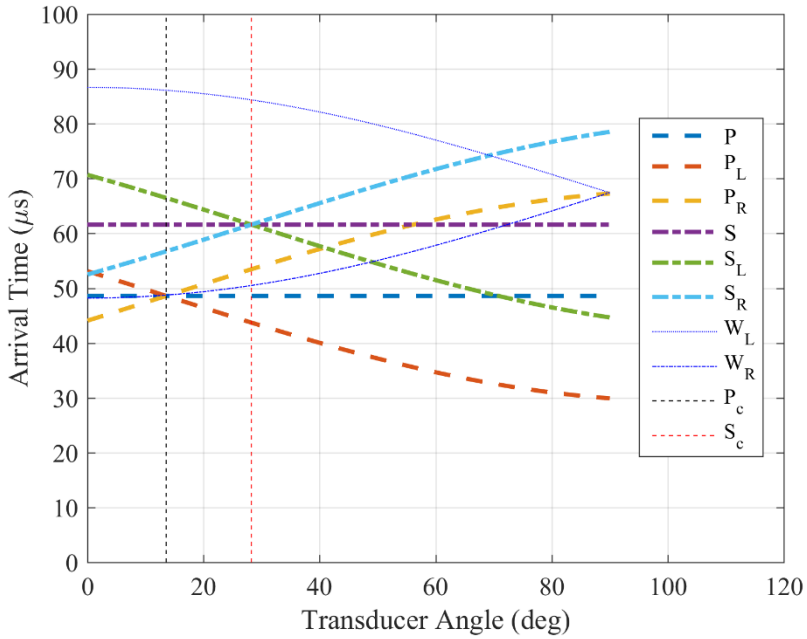

Figure 4.8: Arrival time vs. transducer angle for refracted P and S-waves in aluminum. The direct fluid arrival between the transducers is also shown.

The P-wave from the left bound (P_L) arrives slowly at first and then progressively more quickly as the left transducer edge (bound) moves closer to the sample. The inverse is true for the right bound (P_R). The S-wave left and right bounds similar behavior (S_L and S_R).

When θ_0 is equal to the critical angle, indicated by P_C and S_C, notice how the arrival times from entire transducer face coincide. At these angles, the maximum amount

of refracted energy should arrive at the same time. And finally, the blue lines indicate the left and right bounds for direct fluid arrival (W_L and W_R). The energy of this arrival is likely minimal until the transducers begin to face one another at high angles. At 90°, the transducers are perfectly parallel, and the fluid mode will arrive at the same time with the highest energy.

Figure 4.9 shows these arrivals times converted to the velocity domain assuming that the distance the wave travels in the sample and fluid is constant and equal to the critically refracted ray path distance from transducer center to center. This is intended to highlight how the model converges to the true velocity if a user wanted to use a constant distance to simplify estimation. Within approximately ± 3° of the critical angle, the velocity estimate is accurate.

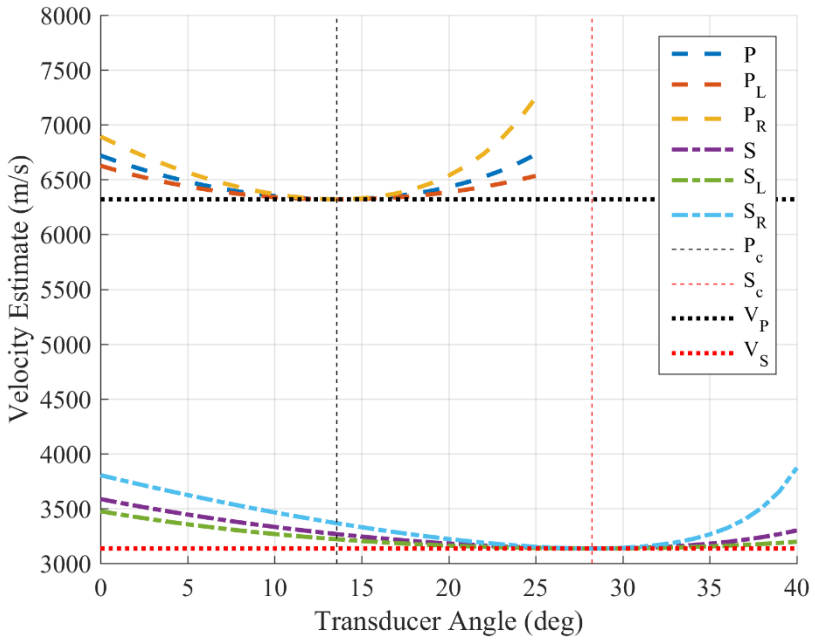

Figure 4.9: Forward model velocity estimate vs. transducer angle for aluminum. Estimate is accurate between ± 3° of the critical angle.

Generally, with these measurements it is best to remain in the arrival time domain as in Figure 4.8 because multiple wave arrivals must be distinguished (P, S, fluid, reflected, etc.). The forward model is intended to help highlight areas of interest on the experimental waveform data. Since the model assumes velocities, it is best to calibrate the model by adjusting the P and S-wave velocities of the samples to produce arrival times that agree with the data. In this way, the velocities are effectively estimated. For the data shown, however, the model inputs are the velocities measured conventionally to verify the model and technique.

Although only a single transmitter and receiver are modeled, the same rules apply for the dual receiver system. The simulation simply needs to be run a second time with a different transducer half spacing, x_1. Ironically, one of the advantages of using two receivers is that it compensates for the travel time in the fluid, meaning the forward model is not necessarily required to evaluate arrival times. With a pair of waveforms, the difference in arrival time between the first and second waveform can be used to calculate both P and S velocities if the receiver spacing is known. Unfortunately, the presence of reflected modes at angles near the critical angle often complicate the use of the array in this fashion. An array with multiple (3+) receivers would be more ideal to analyze waveforms in this way. For the experiments performed, the forward model is critical to reduce uncertainty in understanding the waveforms.

Chapter 5: Experimental Results and Discussion

This chapter showcases the experimental and forward model results for all samples. The results are analyzed with respect to the forward model predictions, with a focus on agreements and discrepancies.

5.1 Prototype No. 1 – Aluminum Control

Experiments were conducted on 2 in and 4 in OD cylindrical aluminum samples as a control. Figures 5.1 and 5.2 show P-waveforms with indicated first arrival times. Note that the amplitudes are only constant along each row. In both cases, most energy is transmitted when H_C is 0.2. This was first suspected to be the fault of improper system setup. However, setup dimensions were verified and this is a valid result. The transducers likely better transmit energy through the samples when enough water is present to couple the transducer and sample.

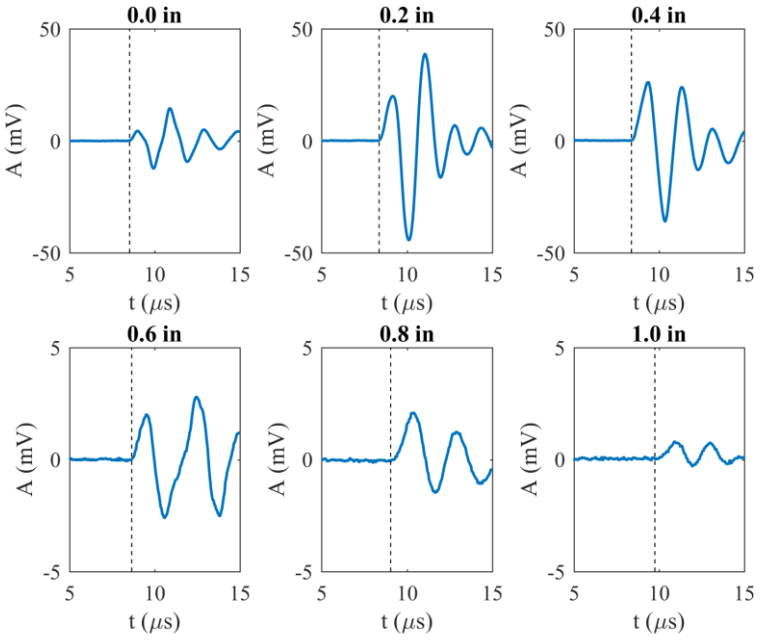

Figure 5.1: Waveforms for 2 in OD aluminum as a function of center height offset (in).

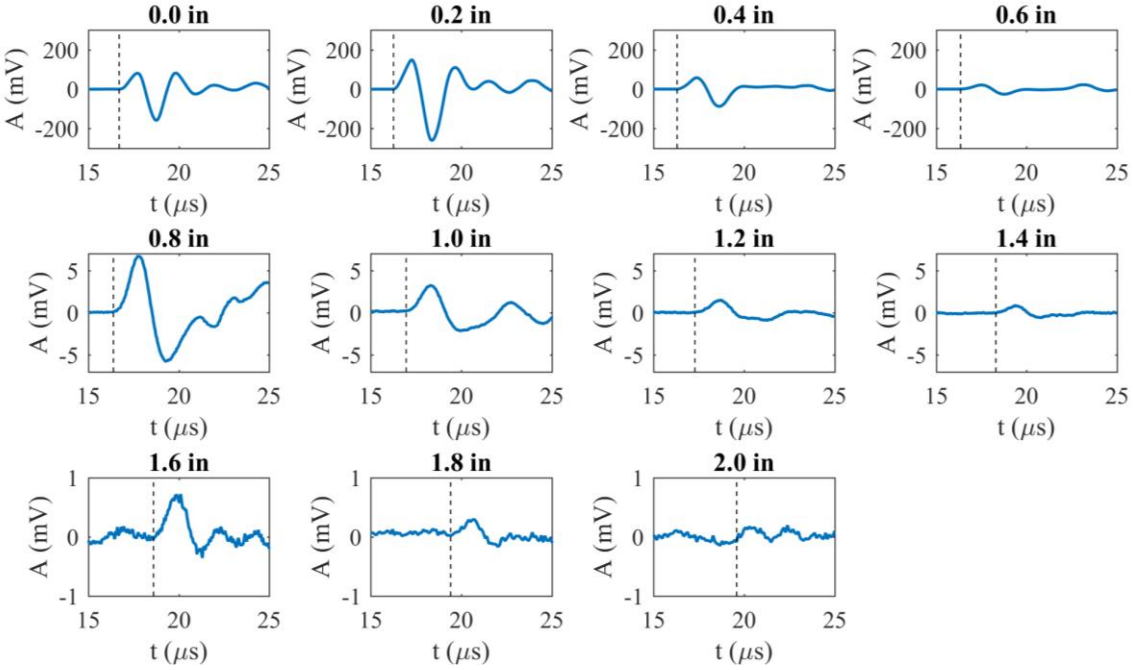

Figure 5.2: Waveforms for 4 in OD aluminum as a function of center height offset (in).

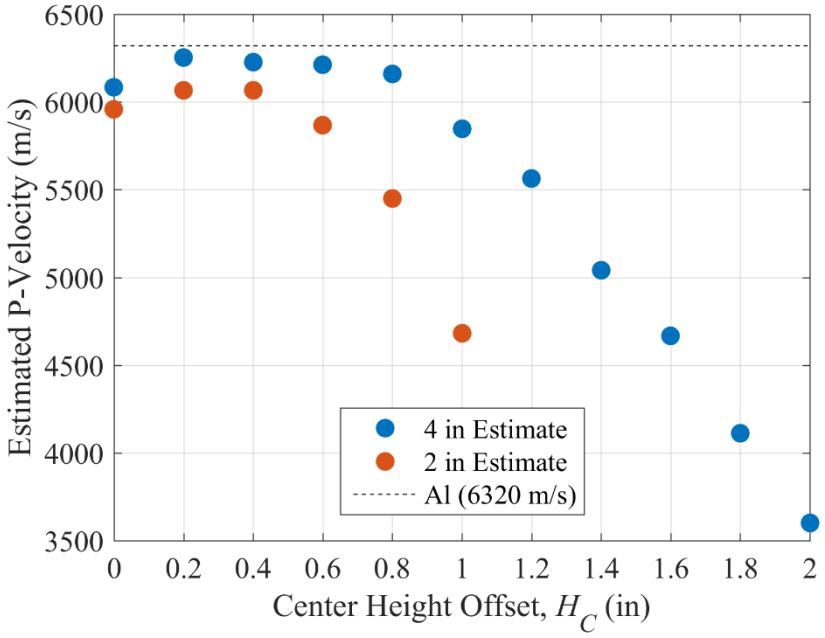

Figure 5.3: Estimated P-wave velocity as a function of transducer center height offset for aluminum.

The velocities are estimated by dividing the transducer separation distance over the selected arrival times shown in the black dotted vertical lines in Figure 5.1 and 5.2. Figure 5.3 depicts the velocity estimates as a function of transducer center height offset for both samples. Only measurements on the 4 in sample produce results that approach the true velocity of aluminum (black dotted line). The 2 in sample results underestimate by about 250 m/s. This is likely due to the incident wavelet wavelength, which is approximately 0.5 in for aluminum from a 500 kHz source. For a 2 in OD sample, at a maximum the specimen is only four times the wavelength in length, which does not meet the ASTM D2845 standard specifying sample length be greater than five times the incident wavelength. The 4 in sample does meet this requirement, which helps explain the better agreement. It could be argued that the first arrival is not emanating from exactly the transducer-sample contact. The wave therefore must travel through water prior to interacting with the sample, which will slow the estimated velocity. Further, the 2 in case will have more water between the transducer and sample due to the increased sample curvature. Comparison with the forward model will help highlight this trend, if it exits.

In both cases, the best estimates occur at a center transducer height of 0.2 to 0.4 in above the sample mid-plane. The maximum amount of energy is transferred through the sample at 0.2 in above the sample mid-plane. Both experiments show slower than expected velocities when aligned to the sample mid-plane. This suggests poor transducer center coupling to the sample. Estimated velocities are shown in Figure 5.4 in relation to the forward model prediction. The P-wave velocity estimates measured are generally less than that of the sample, likely due to the presence of water as the coupling medium. The legend indicates the transducer center height offset, H_C, whereas the x-axis refers more generally to the height offset, y. The data to the left of the dashed line indicate realistic experimental height offsets less than 1/8 of the sample diameter (0.25 in, and 0.5 in, respectively).

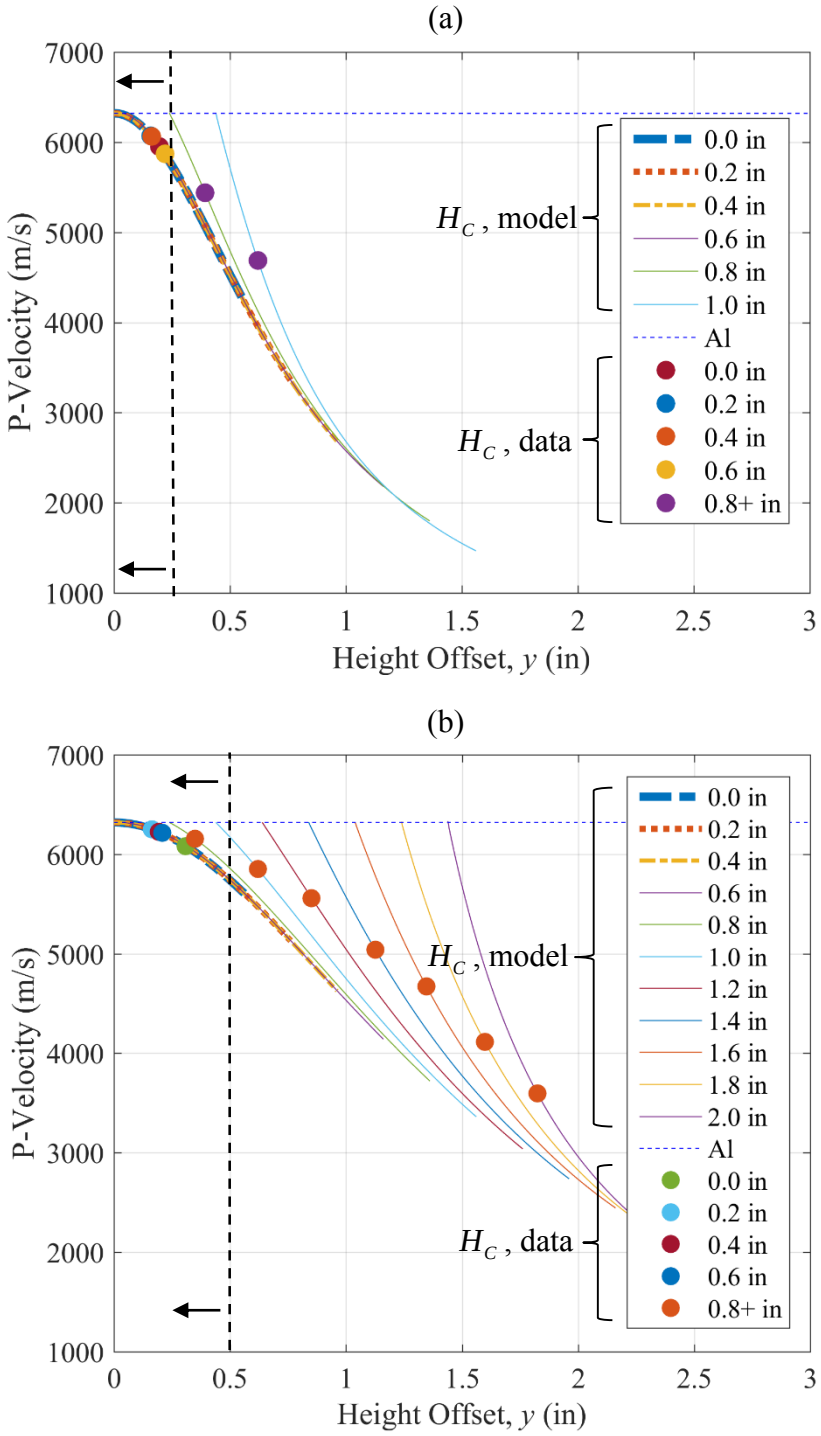

Figure 5.4: Forward model comparison of P-wave velocity estimate as a function of transducer height offset for (a) 2 and (b) 4 in OD aluminum.

This region is useful in estimating the sample P-wave velocity. The 4 in sample estimates better approximate the velocity due to the reduced sample curvature, with the $H_C = 0.2$ in data in both cases providing the most accurate estimate.

Figure 5.5 shows the relationship between the origin of the wavelet as a function of transducer center height offset. The y-axis source location is predicted from the forward model, and the x-axis is the independent variable changed in the experiments (Figure 4.1). Recall that the transducer radius is 0.625 in, which explains why deviation occurs at center height offsets above 0.6 in. First arrival energy tends to interact with the sample 0.2 in above the sample mid-plane for aluminum. This data suggests that there is not a location on the transducer face that preferentially emanates energy because changing the transducer center height offset does not change the estimated height at which the first arrival wave originated from. More realistically, there is a minimum amount of fluid required to couple the acoustic energy. Agreement between the 2 in and 4 in sample experiments is interesting, because it suggests that sample curvature has a minimal effect.

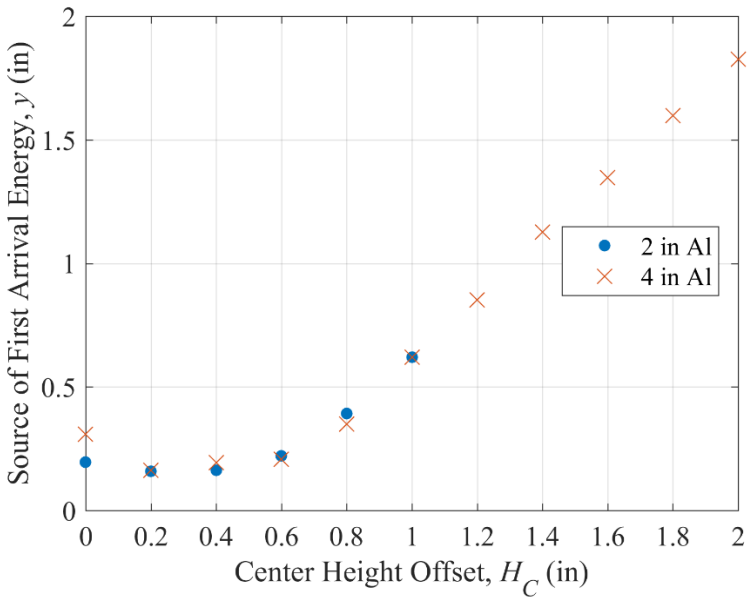

Figure 5.5: Modeled origin of the first arrival energy from the transducer.

5.2 Prototype No. 1 – Dry and Water Saturated Cores

Next, the same experiments were performed on cylindrical rock samples, both dry and fully water saturated. Figures 5.6 through 5.9 show the raw waveforms for both 2 and 4 in Berea sandstone and Texas Cream limestone with superimposed arrival times. As expected, the waveforms indicate that the fully water saturated samples have faster arrival times and larger amplitudes. The arrival time contrast is much more noticeable in the Berea sandstone, which suggests that this rock is more porous and/or has a lower bulk modulus than the Texas Cream limestone. The late-time high amplitude peaks present in the Berea sandstone testing are due to the direct fluid arrival. These are also present in the limestone data, but are not displayed to better contrast arrival times.

Estimated sample velocity as a function of center height offset are shown in Figure 5.10, with a baseline reference corresponding to the conventionally measured P-wave velocity for both dry and fully water saturated rocks. While the aluminum control experiments largely underestimated the velocity in accordance with the forward model, these experiments show a different trend. For Berea sandstone (Figure 5.10a), at offsets below 1 inch the velocity is often over-estimated. Underestimation is still dominant for the Texas Cream limestone (5.10b). Due to rock heterogeneity, care was taken to measure across the same sections of each rock sample. One explanation for the over-estimation present, especially in the fully water saturated Berea sandstone, is that the section of rock measured has a locally higher velocity. A lengthwise, conventional estimate measures the full 8 in of core as compared to a diameter-wise estimate which measures only 2 or 4 in of core in a different direction. The forward model is not useful to analyze this data because it does not predict the presence of an over-estimation. The forward model is much better suited for isotropic, homogenous materials.

(a)

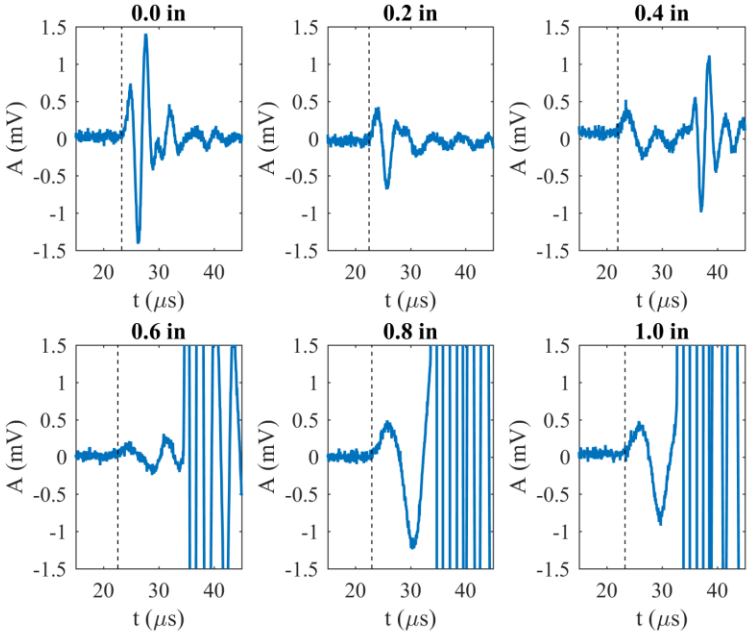

(b)

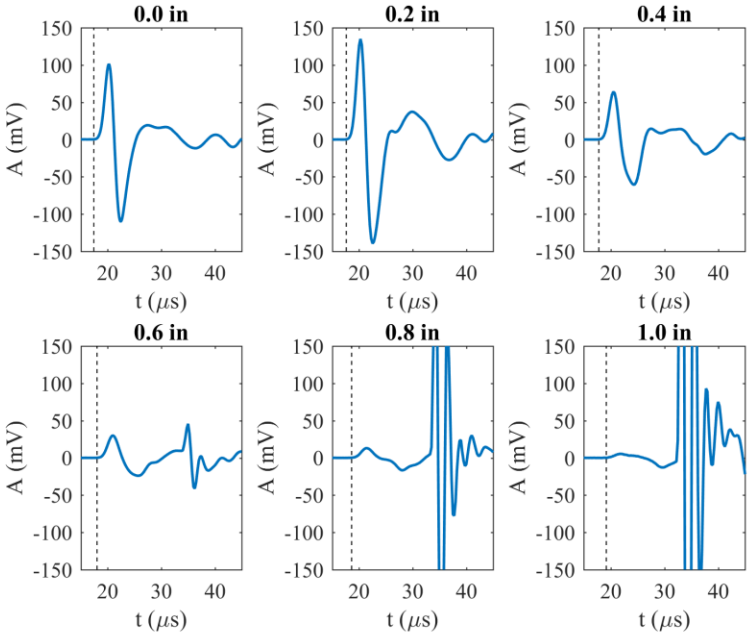

Figure 5.6: Dry (a) and fully water saturated (b) P-waveforms for 2 in OD Berea sandstone as a function of center height offset (in).

(a)

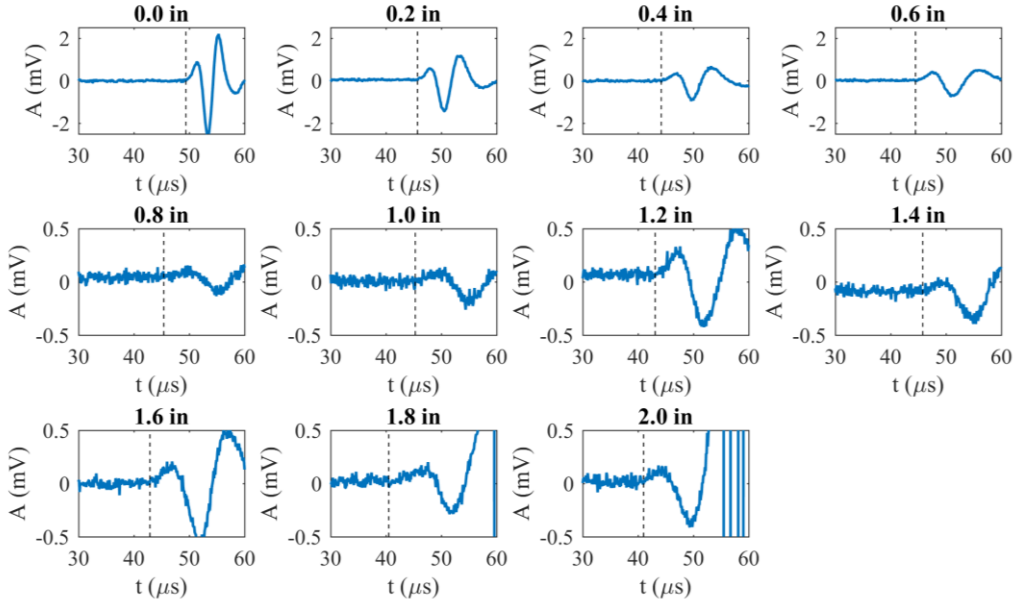

(b)

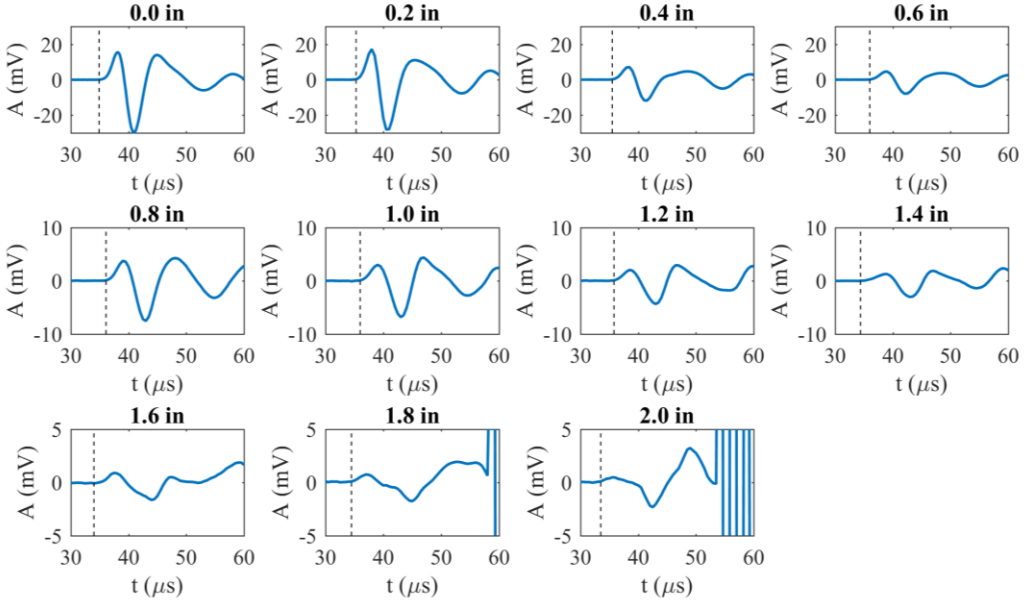

Figure 5.7: Dry (a) and fully water saturated (b) P-waveforms for 4 in OD Berea sandstone as a function of center height offset (in).

(a)

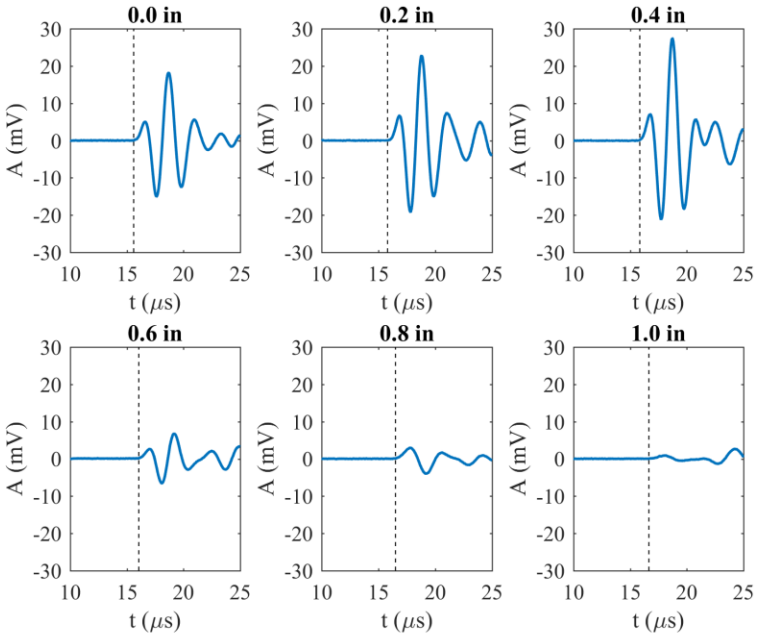

(b)

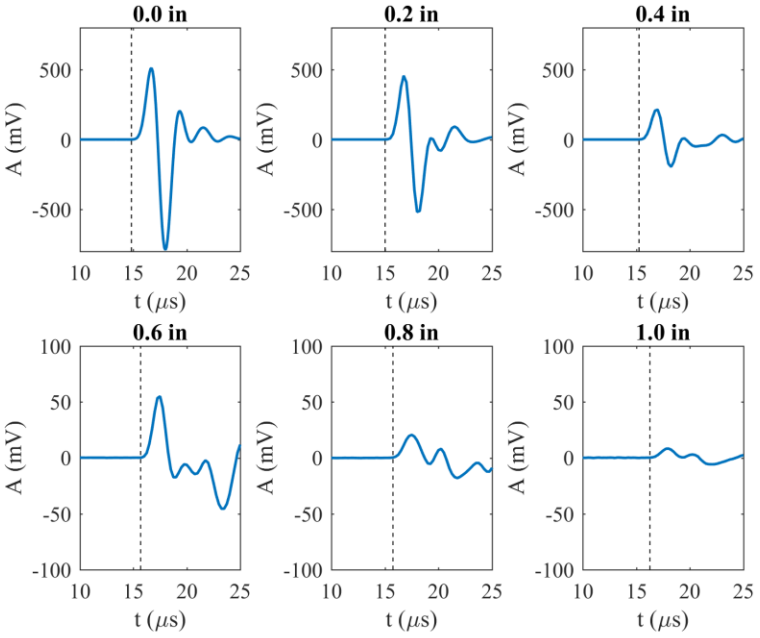

Figure 5.8: Dry (a) and fully water saturated (b) P-waveforms for 2 in OD Texas Cream limestone as a function of center height offset (in).

(a)

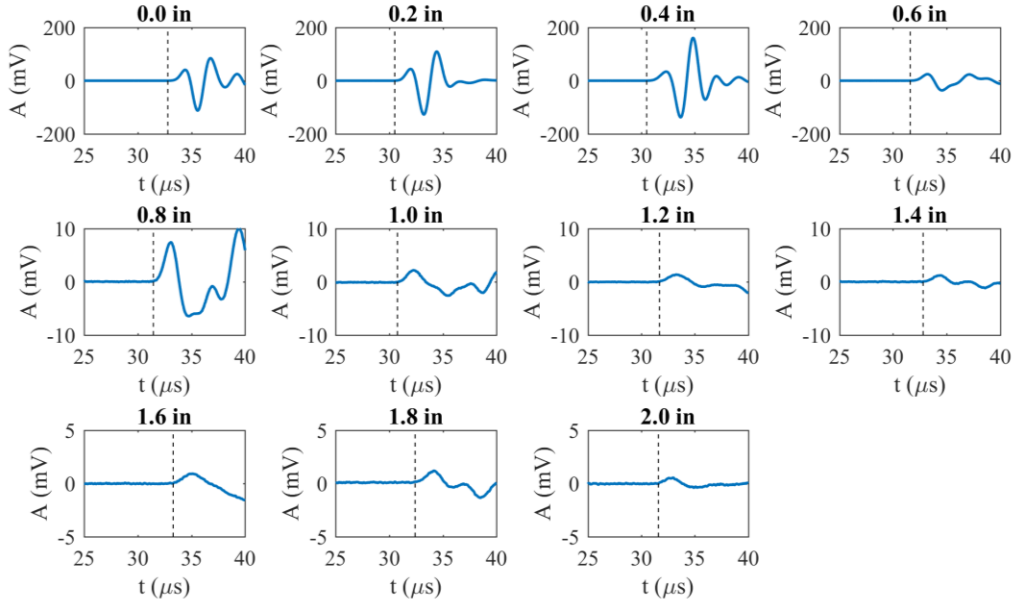

(b)

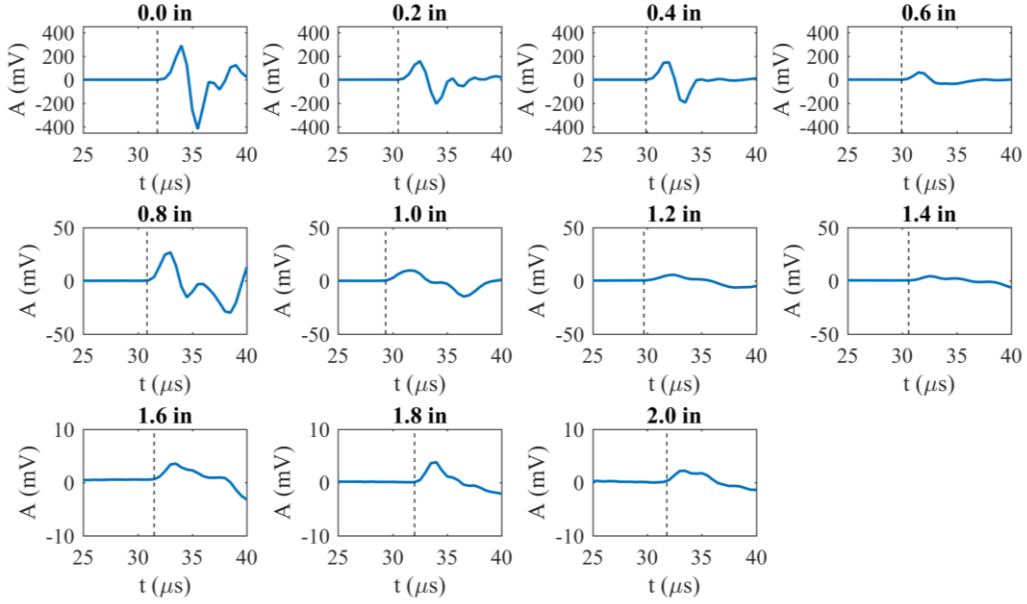

Figure 5.9: Dry (a) and fully water saturated (b) P-waveforms for 4 in OD Texas Cream limestone of center height offset (in).

For all experiments, the ideal center height offset to measure the velocity is approximately 0.2 to 0.6 in. This confirms the unexpected trend seen in the aluminum testing: measuring at zero center height offset with these transducers does not produce reliable velocity estimates. The only seemingly accurate estimate taken at zero height offset was that of the 2 in fully water saturated Texas Cream limestone. The data suggest that these transducers are more effective when there is some water between the center of the transducer and the sample. For future corroborative testing, the transducers need not be tangent to the sample. This will likely allow the fluid to better couple the incident wave, and velocity estimates of the sample may be obtained if the velocity of the fluid is known.

Importantly, this data needs to be viewed in the context of Gassmann's equations. Table 5.1 shows the measured data required for analysis from conventional core analysis in addition to the assumed bulk moduli constants. The only non-conventionally acquired measurements used in the calculations are the dry P-velocity estimates shown in Figure 5.10. First, the bulk and shear moduli of the dry rock are calculated. Using Gassmann's

Sample	$\rho_{b,dry}$ (g/cc)	$\rho_{b,\text{sat}}$ (g/cc)	ρ_{mat} (g/cc)	Φ (%)	$V_{S,dry}$ (m/s)	K_{mat} (GPa)	K_w (GPa)
Berea Sandstone	2.09	2.29	2.61	19.90	1560	36.6	2.15
Texas Cream Limestone	1.92	2.20	2.67	28.12	1910	76.8	

Table 5.1: Relevant experimental constants for Gassmann's equation application.

equations, the bulk moduli of the fully water saturated rock are calculated. And finally, the P-velocity estimates for the fully water saturated rock are calculated as a function of the saturated bulk modulus, bulk density, and assumed constant shear modulus (from $V_{S,dry}$). The results of the predicted P-wave velocity are shown in Figure 5.11.

(a)

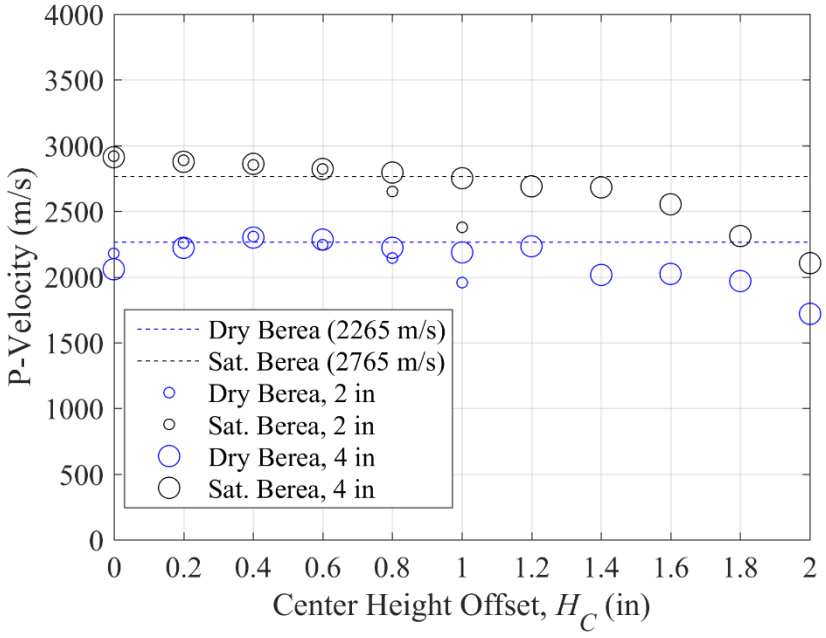

(b)

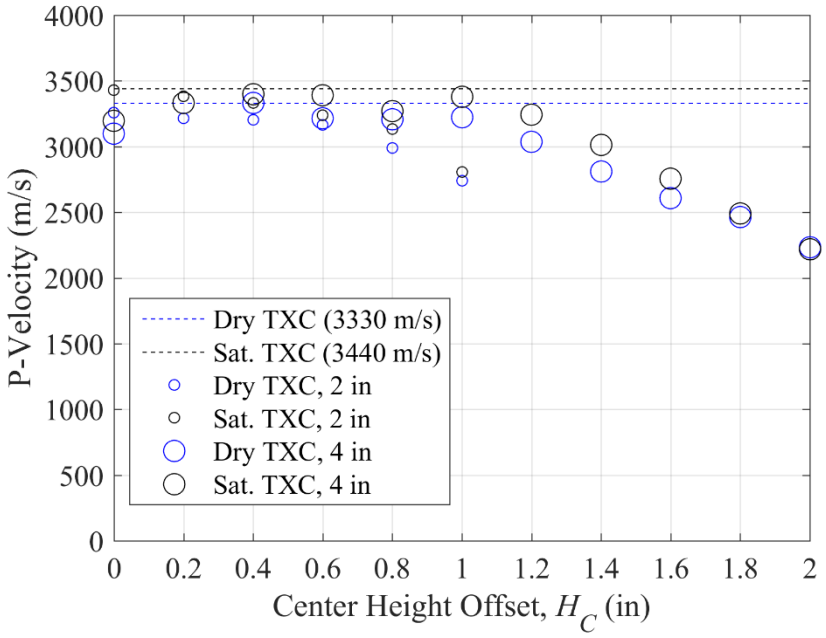

Figure 5.10: Comparison of P-wave velocity estimate vs. center height offset for 2 and 4 in OD Berea sandstone (a) and Texas Cream limestone (b) cores.

(a)

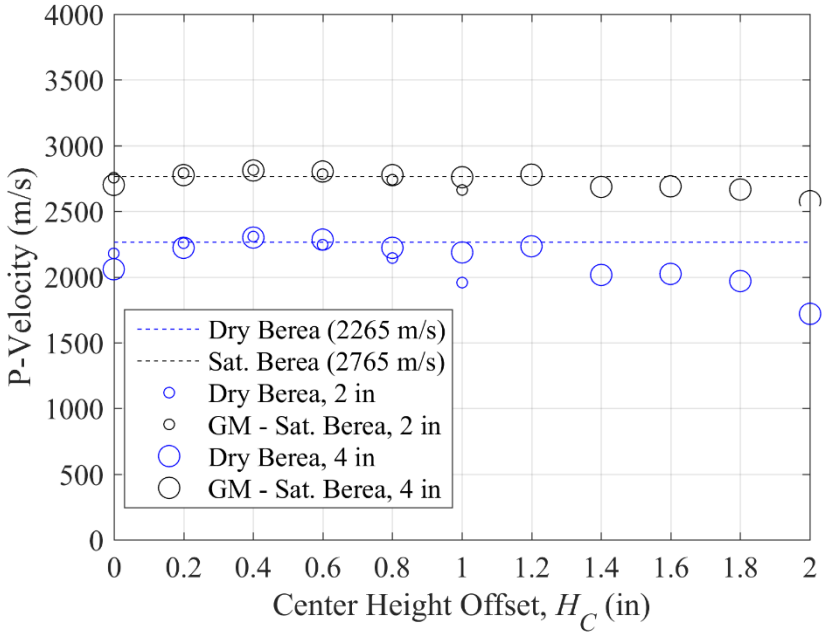

(b)

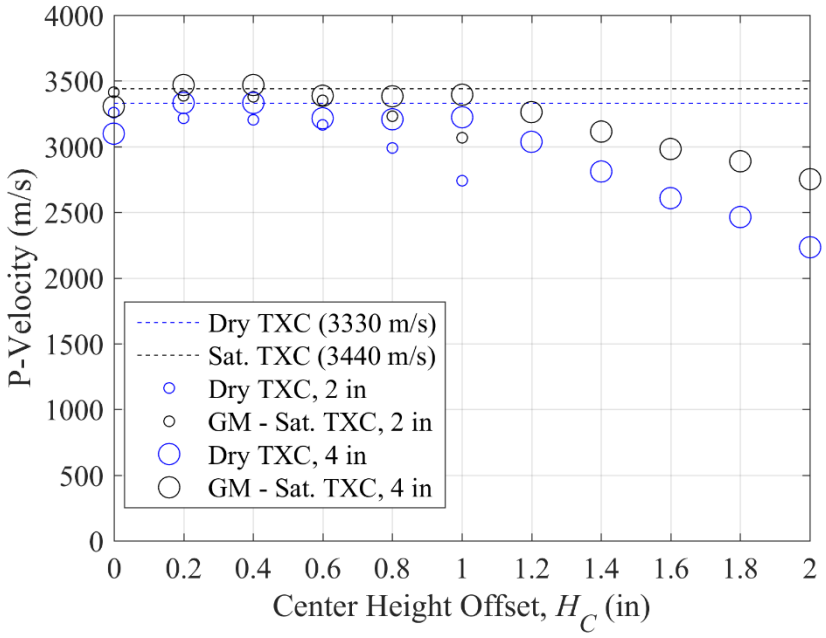

Figure 5.11: Gassmann fluid substitution estimates from dry (air saturated) to fully water saturated for Berea sandstone (a) and Texas Cream limestone (b).

Gassmann's equations corroborate the experimental results. Granted, the methodology does slightly lessen the data variance seen in the original dry data (blue and red). To get an idea of the accuracy of the method with respect to the conventionally acquired ultrasonic P-velocity data, compare the dry data points that lie close to the dotted lines with their associated water saturated points. Gassmann's equation in this context induces a slight over-estimation for both rocks.

However, it may not be wise to compare the conventional measurements due to the previously mentioned rock heterogeneity and change in both measurement direction and zone of analysis. Results from both types of measurements agree with the magnitude of change predicted by Gassmann's equations by less than a 2% error margin. This validates the use of either method to accurately measure rock acoustic velocities.

5.3 Prototype No. 3 – Aluminum Control

Recall that prototype No. 3 is an improved version prototype No. 2 with an additional receiver. As with prototype No. 1, the rock experiments are benchmarked to aluminum samples of the same size. Table 5.2 summarizes the forward model inputs used to predict arrival times and assist understanding of the waveforms. The variables $x_{1,1}$ and $x_{1,2}$ refer to the emitter/receiver half spacing for the first and second receiver, respectively; $y_{1,2}$ and $y_{1,4}$ refer to the sample distance from the transducer center for the 2 and 4 in samples. P_C and S_C are the calculated critical P and S angle rounded to the nearest 5°.

V_P (m/s)	V_S (m/s)	$x_{1,1}$ (mm)	$x_{1,2}$ (mm)	$y_{1,2}$ (mm)	$y_{1,4}$ (mm)	P_C	S_C
6320	3135	50	100	29	33	15°	30°

Table 5.2: Forward model inputs for 2 in and 4 in OD aluminum samples.

Experimental data are collected at transducer rotations from 0 to 65° in increments of 5°. The figure subtitles refer to this angle, with a 2 subscript denoting the second receiver. The relevant data are in Appendix A and B for 2 in and 4 in aluminum. The black lines indicate the range of plausible P-wave arrival times, and the red lines indicate the same for the S-wave arrival. The blue lines model the range of the direct fluid arrival, which is more of an issue for the study of rocks, as they have a lower speed of sound than aluminum. This wave mode will only interfere for the first receiver.

Based on the model, the most important waveforms should be those generated at a transducer rotation that corresponds closely to the critical angle of refraction for both the P and S-wave, as indicated in Table 5.2. These waveforms are shown in Figures 5.12 and 5.13. The P-wave arrival is evident and agrees with the model in all cases, except it is of low amplitude at the second receiver for the 2 in sample. The S arrival transition is nicely shown, and is of much larger amplitude than the P arrival. Refer to Appendix A and B for a complete view of the waveform progression as a function of angle.

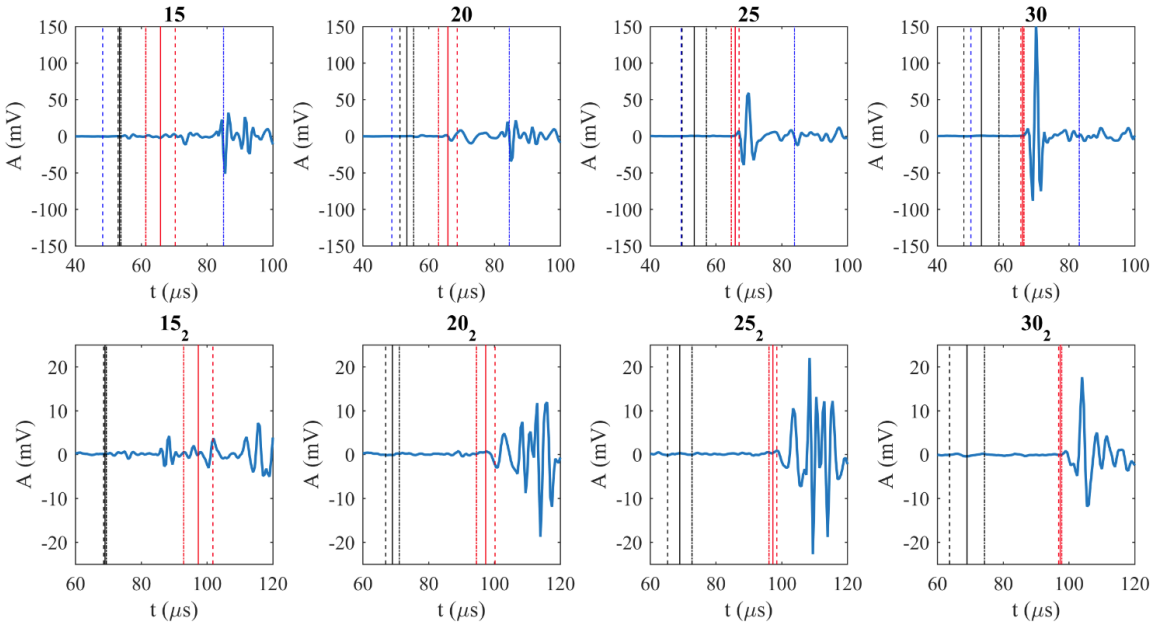

Figure 5.12: 2 in OD aluminum waveforms. P: Black, S: Red, Direct: Blue.

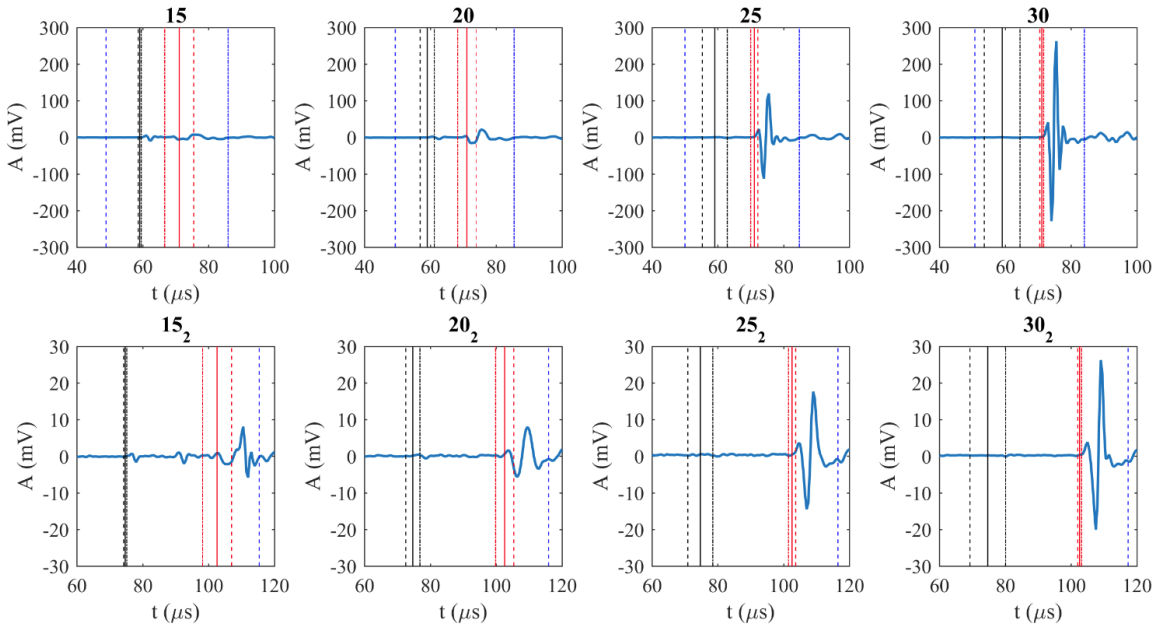

Figure 5.13: 4 in OD aluminum waveforms. P: Black, S: Red, Direct: Blue.

Shear energy exists at angles near the critical angle, but the amplitude is maximized at the critical angle. Note the agreement between the arrival time predictions and data for both P and S-waves. Overall, the data are of higher quality on the 4 in sample. This is likely because the sample is larger and better approximates a planar interface. The aluminum control tests readily agree with modeling and validate the use of such a system to estimate velocities and associated dynamic elastic properties of cylindrical samples.

5.4 Prototype No. 3 – Dry and Water Saturated Cores

The forward model inputs for dry and fully water saturated Berea sandstone are shown in Table 5.3. The velocity inputs are determined from conventionally measuring P and S-wave velocity of the samples. Appendices C and D show the data for dry Berea sandstone, and Appendices E and F for the fully water saturated Berea sandstone. The pertinent dry data are shown in Figures 5.14 and 5.15.

	V_P (m/s)	V_S (m/s)	$x_{1,1}$ (mm)	$x_{1,2}$ (mm)	$y_{1,2}$ (mm)	$y_{1,4}$ (mm)	P_C	S_C
Dry	2265	1560	50	100	29	33	40°	70°
Sat.	2765	1490	50	100	32	26	30°	85°

Table 5.3: Forward model inputs for 2 in and 4 in OD Berea sandstone cores.

In all measurements, reflected waves exist from approximately 50° to 60°. These may occlude the desired wave arrivals. The reflection only interferes with measurements for the first receiver; the second receiver will not measure a direct reflection. The dry data show that the P-wave arrival is of minimal amplitude and cannot be readily identified at the critical angle. Even though the first receiver at 40° shows an arrival at the black line, the P and S-wave arrivals (black and red lines) overlap.

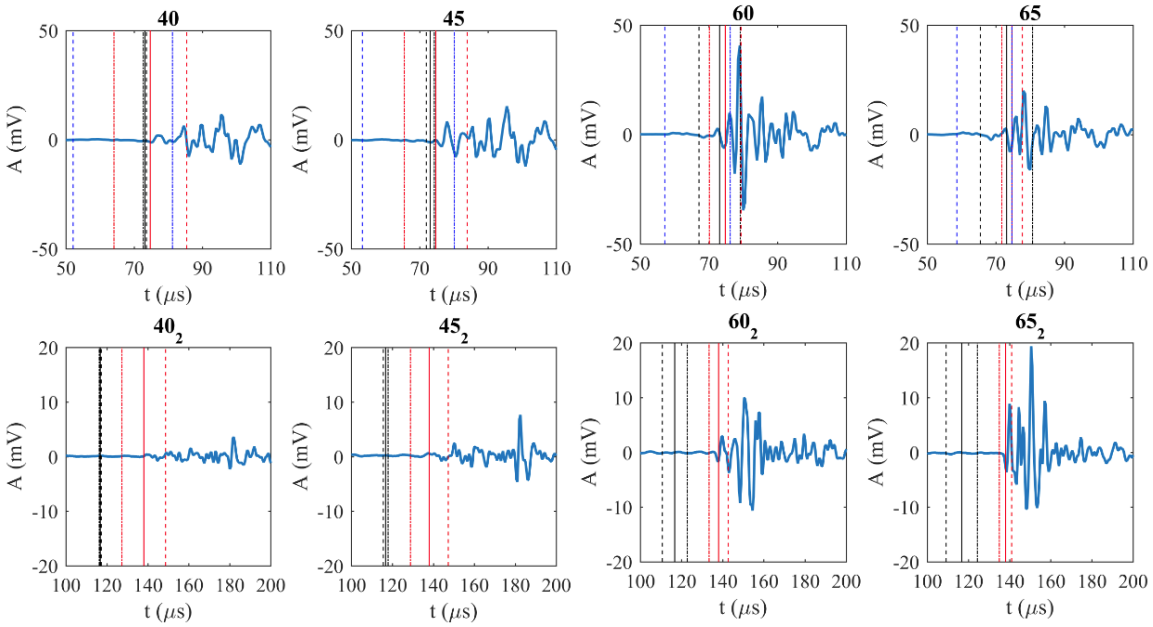

Figure 5.14: 2 in OD dry Berea waveforms. P: Black, S: Red, Direct: Blue.

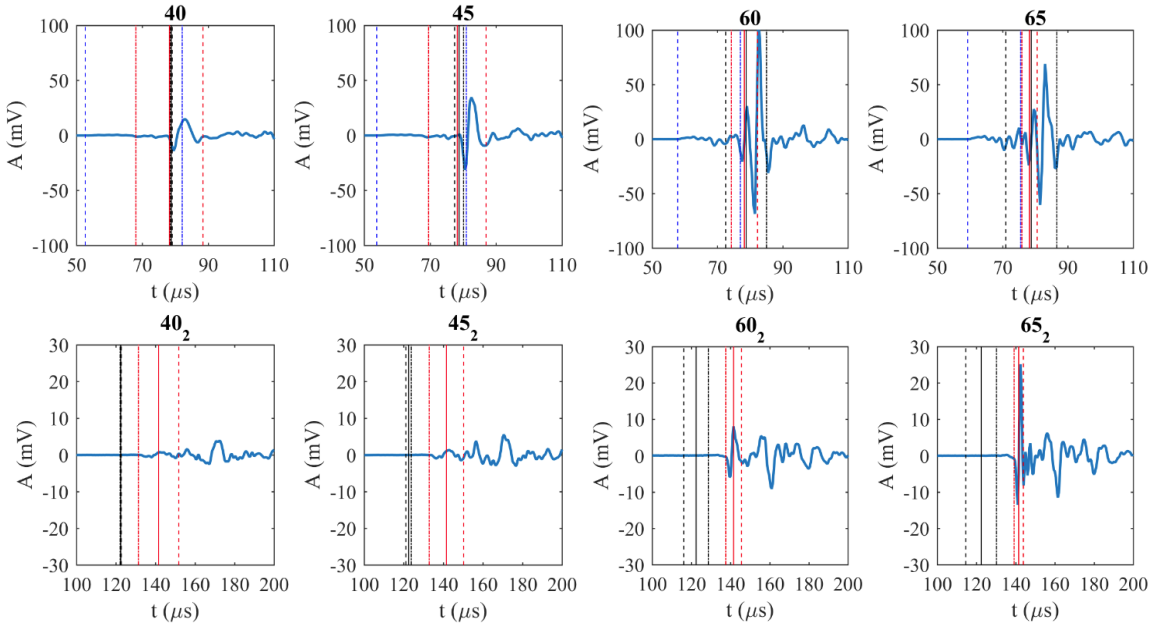

Figure 5.15: 4 in OD dry Berea waveforms. P: Black, S: Red, Direct: Blue.

It is likely we are seeing mostly shear energy at 40°, as evidenced by the lack of a clear P arrival on both second receivers at 40°. However, S-wave arrival is accurately predicted for both receivers at angles approaching the critical angle of 70°. Perhaps the air in the pore space creates a high impedance contrast and greatly reduces the amplitude of the P-mode.

The relevant fully water saturated Berea sandstone data from Appendix E and F are shown in Figures 5.16 and 5.17. The data are zoomed in amplitude to highlight arrival trends. The previously shown data did not warrant exact windowing in an effort to remain consistent with amplitude; the data in the appendix remain amplitude consistent for simplified viewing. Note the fluid arrival indicated by the dashed blue line for all first receiver cases around 53 µs. This signal is weak and does not interfere with the P-wave arrival shown (black lines) at 30°. However, the S-wave arrival at 65° is occluded by the high amplitude direct fluid mode for the first receiver. The second receiver shows the proper trend. The data for both the 2 and 4 in samples are consistent and show how fluid in the pore space enhances recognition of the P-wave arrival in rocks.

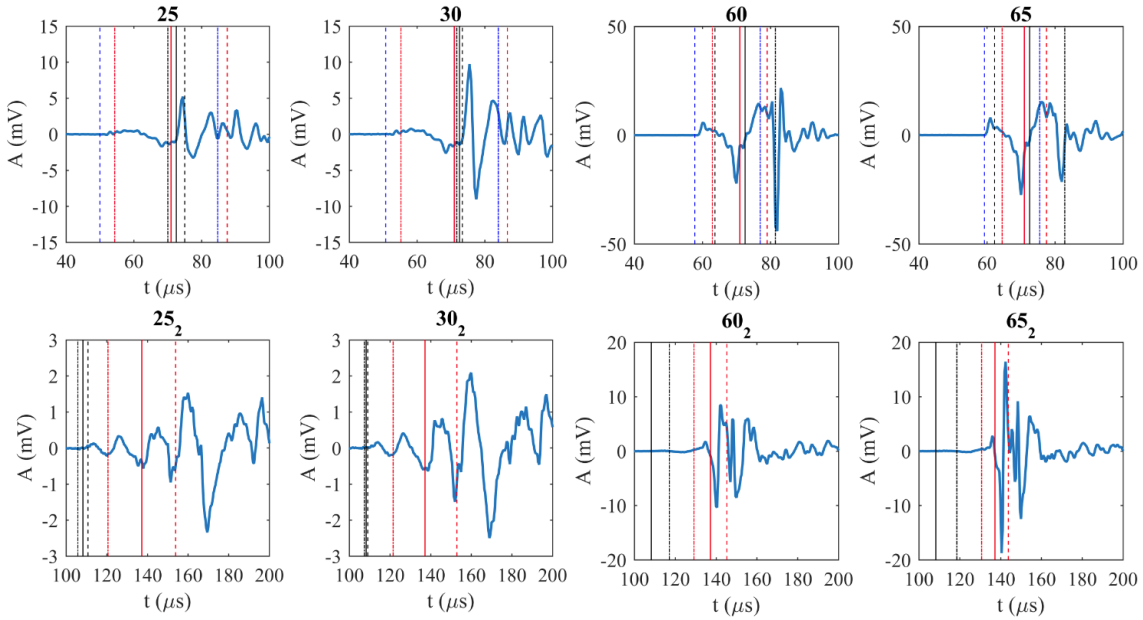

Figure 5.16: 2 in OD saturated Berea waveforms. P: Black, S: Red, Direct: Blue.

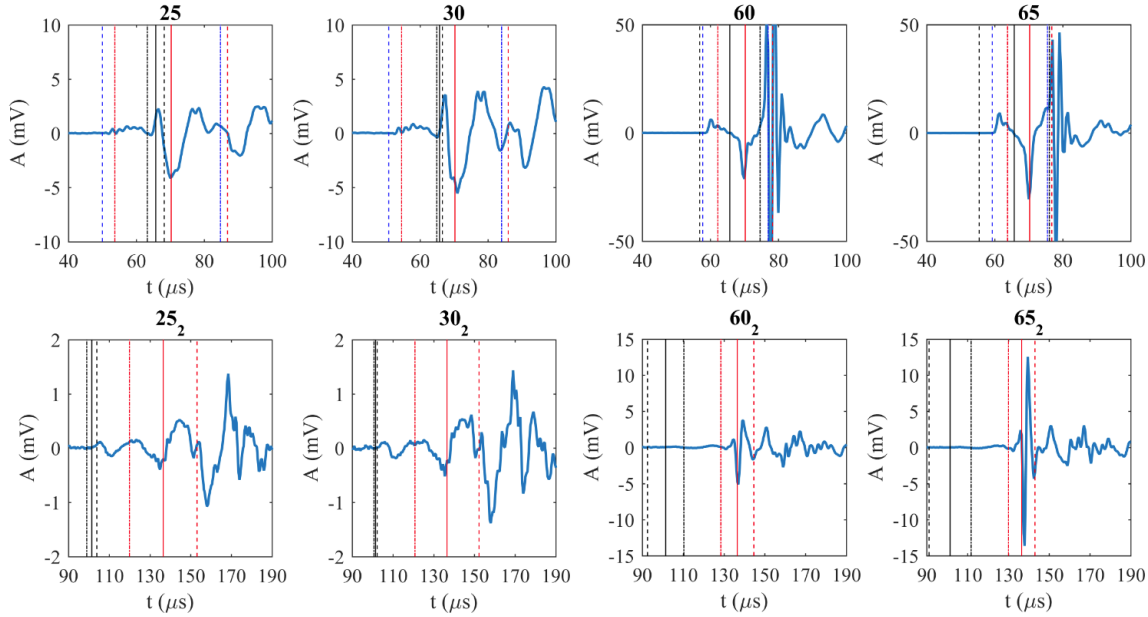

Figure 5.17: 4 in OD saturated Berea waveforms. P: Black, S: Red, Direct: Blue.

Table 5.4 shows the forward model inputs and critical angle outputs for dry and fully water saturated Texas Cream limestone. Appendices G and H show the data for dry

samples, and Appendices I and J for the water saturated samples. The dry rock data of interest is shown in Figures 5.18 and 5.19 for 2 in and 4 in samples, respectively. For the 2 in sample, there is a P-arrival at the first receiver at 25°, and a much smaller amplitude arrival at the second receiver. The 4 in sample shows a clear P-arrival at both receivers, but the model predicts a slightly faster arrival time for the second receiver. This could be due to sample heterogeneity, or possibly alignment issues.

	V_P (m/s)	V_S (m/s)	$x_{1,1}$ (mm)	$x_{1,2}$ (mm)	$y_{1,2}$ (mm)	$y_{1,4}$ (mm)	P_C	S_C
Dry	3330	1910	50	100	32	33	25°	50°
Sat.	3440	1780	50	100	32	26	25°	55°

Table 5.4: Forward model inputs for 2 in and 4 in OD Texas Cream limestone cores.

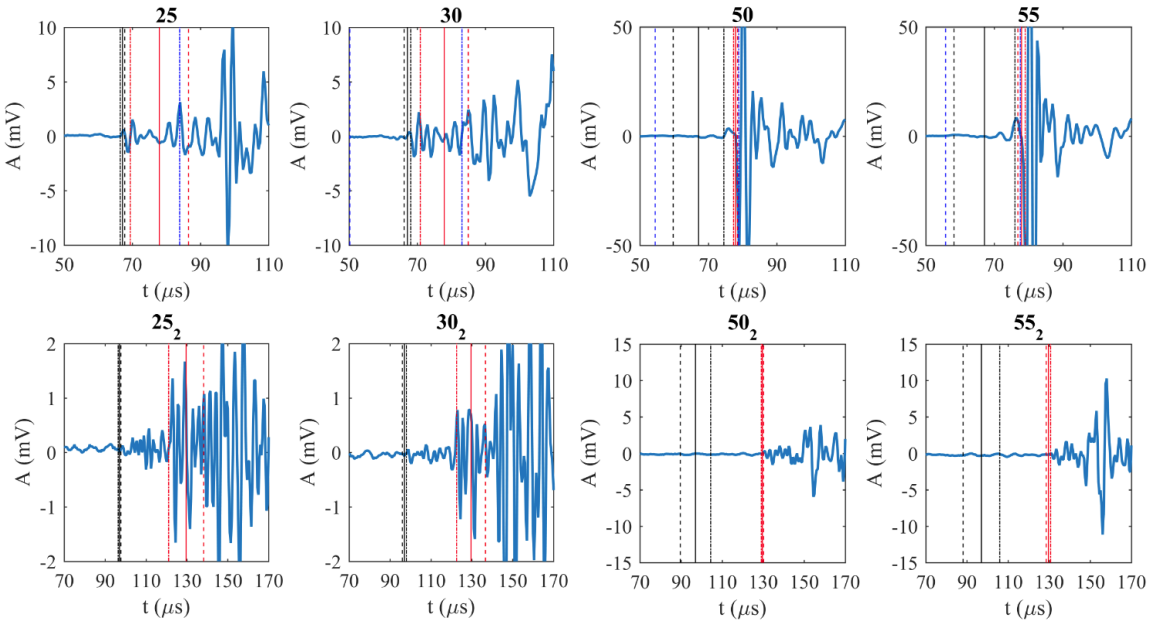

Figure 5.18: 2 in OD dry Texas Cream limestone waveforms. P: Black, S: Red, Direct: Blue.

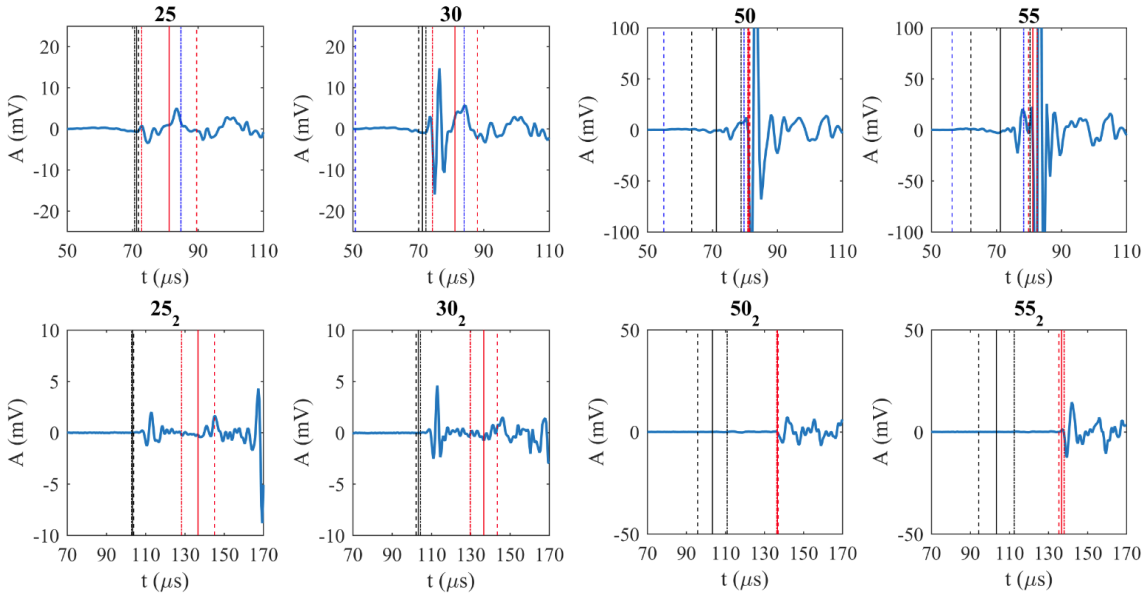

Figure 5.19: 4 in OD dry Texas Cream limestone waveforms. P: Black, S: Red, Direct: Blue.

The forward model assumes that the transducer centers and sample edge are perfectly parallel. A slight deviation could result in changes in arrival, which would be easier to notice at the second receiver. Further, regarding model sensitivity, a ± 1 mm change in the sample-transducer spacing (y_1) can produce a ± 2 μs change in the predicted arrival time. These issues highlight the necessity of properly measuring and calibrating the setup prior to data acquisition.

The S-arrival is difficult to discern at the first receiver due to the presence of a direct reflection. The S-wave behavior is shown accurately at the second receiver for both sample sizes at a critical angle of 50°. The maximum amplitude at the critical angle is not shown in this data. Additionally, note the difference in waveforms for the 2 and 4 in shear waves. The 4 in data show shear arrivals similar to those seen in aluminum, and the 2 in data show what appears to be a shear body wave following the shear head wave (refracted wave). This

is likely due to the sample size. Perhaps it is easier to induce shear body waves in smaller samples.

Comparison with the dry Berea data suggest the following: 1) Obtaining dry rock P-wave velocity is easier for stiff rocks; 2) Dry rock S-wave velocity is better identified when the sample is large. Arguably, the amplitude of the signals is not as high as desired. While the signal generator is sufficiently powerful, the low amplitudes shown and lack of P-arrival for the dry Berea sandstone data suggest that a higher amplitude impulse signal would be ideal for corroborative experiments.

The fully water saturated Texas Cream limestone data are shown in Figures 5.20 and 5.21. Note the direct fluid mode presence for all first receiver data. Both samples show a clear P-wave arrival at both receivers at 25°. The S-wave arrival at 55° is hidden by the direct reflection for the first receiver but properly shown at the second receivers.

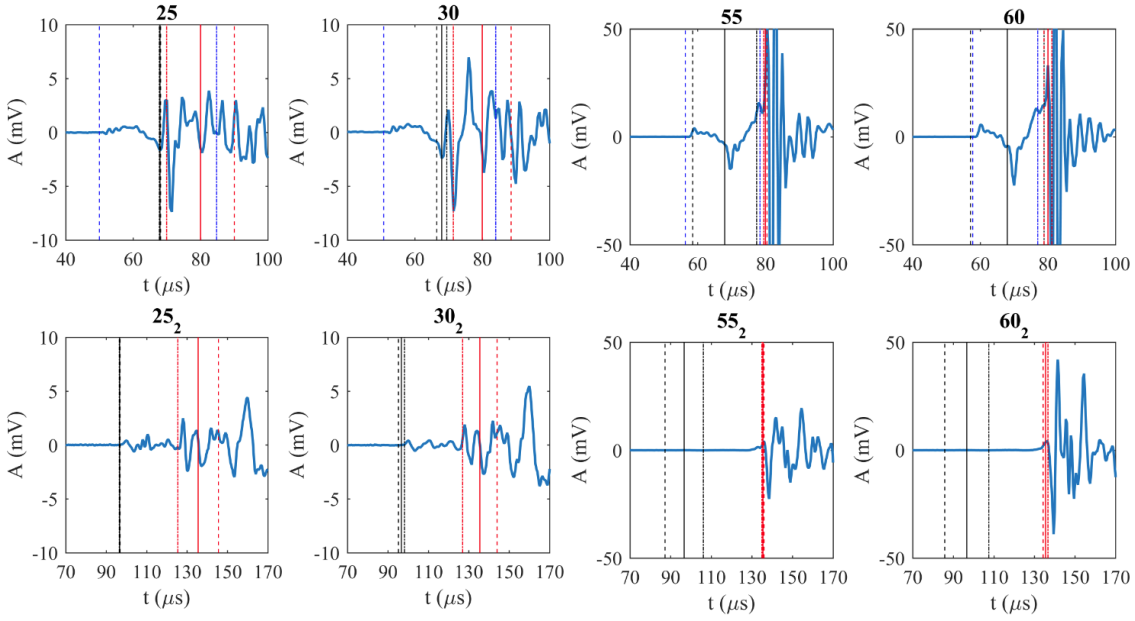

Figure 5.20: 2 in OD saturated Texas Cream limestone waveforms. P: Black, S: Red, Direct: Blue.

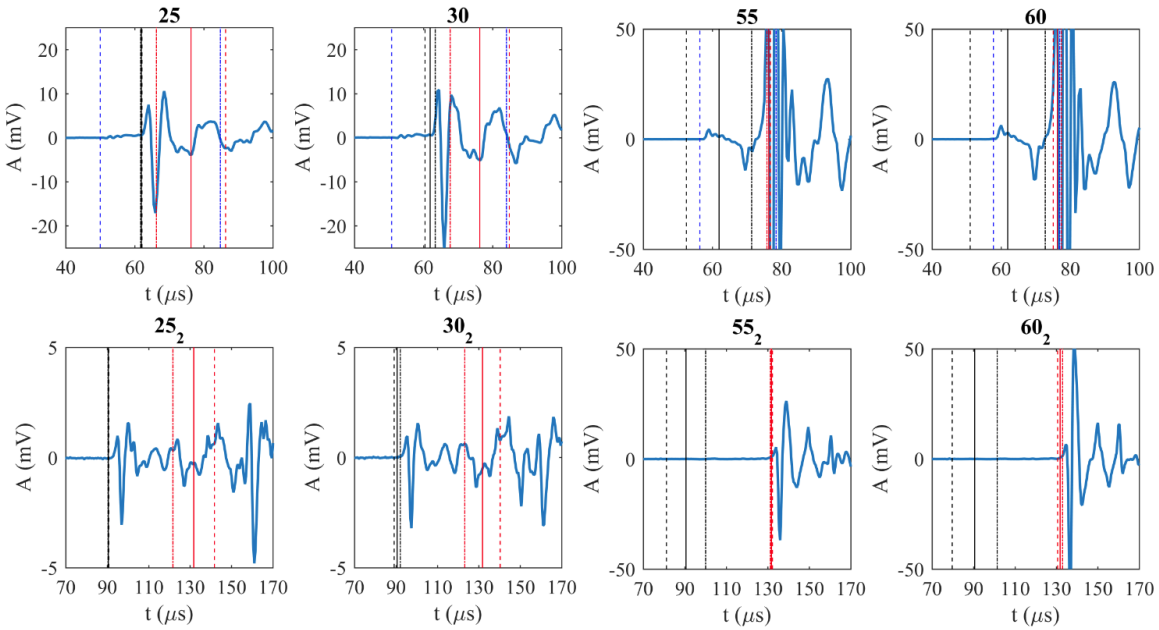

Figure 5.21: 4 in OD saturated Texas Cream limestone waveforms. P: Black, S: Red, Direct: Blue.

Both sample sizes exhibit ideal trends, with the 4 in sample showing larger P and S-wave arrival amplitudes. Not surprisingly, waveform complexity increases when comparing aluminum samples to dry and water saturated rock samples. This is a function of rock heterogeneity and overall lower acoustic velocities, which can make it more difficult to isolate proper wave modes. Alternatively, waveforms may be examined independently of the forward model in a comparative sense to estimate P and S-wave velocities. However, without the forward model, one is subject to bias when selecting arrivals and waveforms, and the data may overwhelm such visually simplistic analysis—especially with only two receivers. An array with three or more receivers would be more appropriate for conventional wireline acoustic analytical methods.

To summarize all of the raw waveform results, the arrival times predicted are compared to the actual arrival times of the waveforms. Additionally, the measured arrival times are used to calculate a velocity estimate assuming a critically refracted ray-path from

transducer center to center. The comparison of the true sample velocities (i.e., the velocities measured conventionally and used as an input for the forward model) with the experimental velocities are shown in Figure 5.22.

(a)

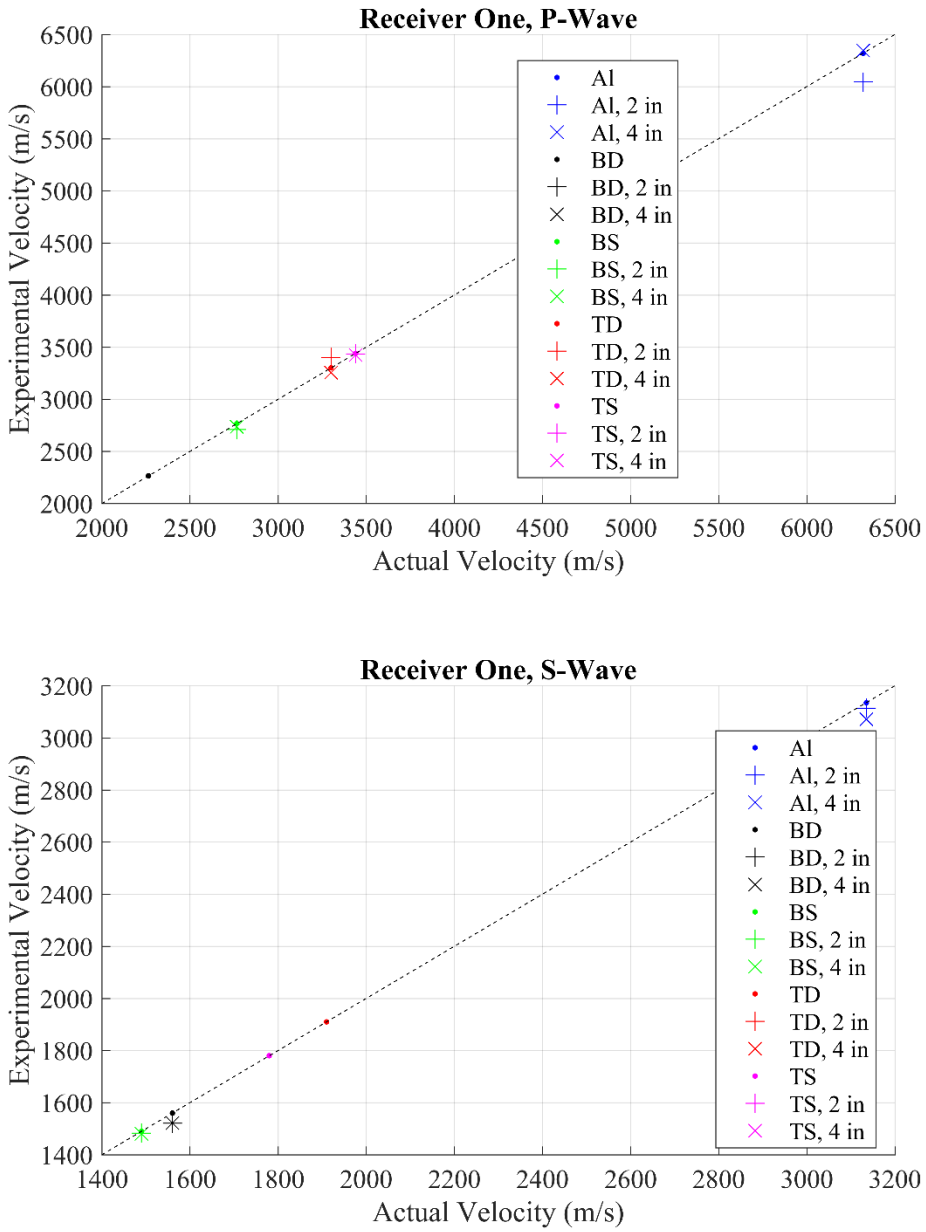

Figure 5.22: Comparison of the actual sample velocity with the experimental velocity acquired with prototype No. 3 using receiver one (a) and two (b).

(b)

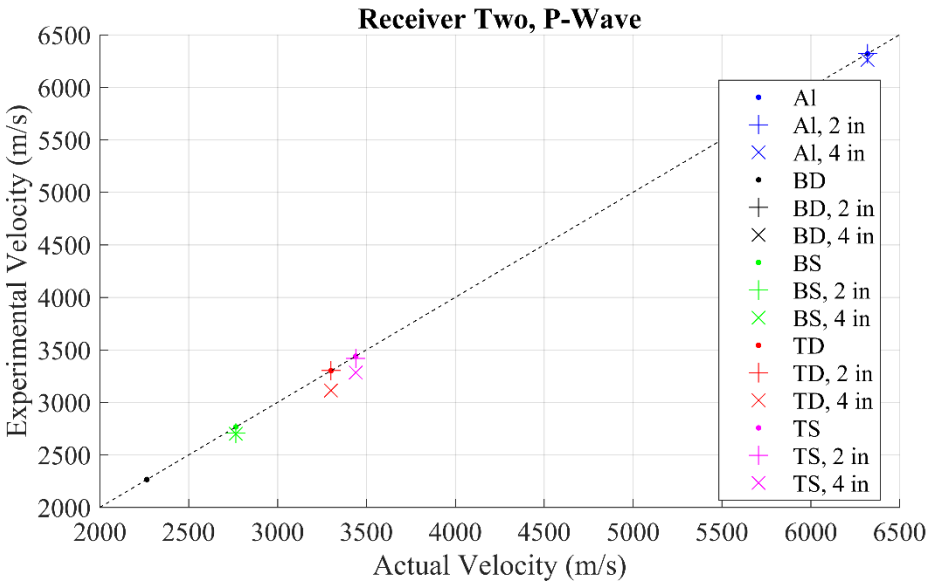

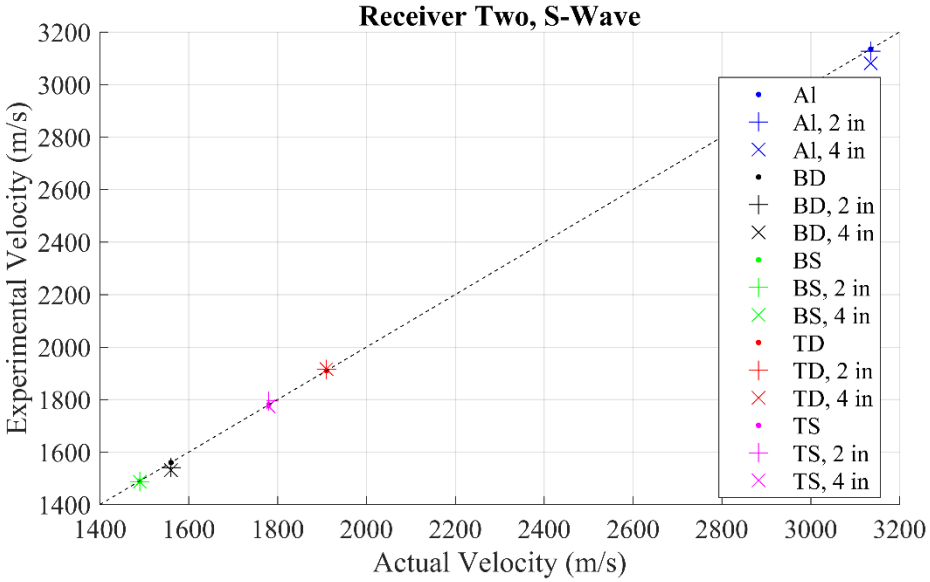

Figure 5.22 continued.

In the legend, B and T stand for Berea sandstone and Texas Cream limestone, with D and S denoting dry and saturated experiments. Note the lack of Texas Cream limestone shear data at receiver one due to reflected mode occlusion and lack of dry Berea sandstone P-wave data due to insufficient signal power. The velocity estimates are consistently within

about 250 m/s of the true sample velocity. However, it is best to quantify the disagreement by calculating the errors.

The relationship between the errors in both arrival time and velocity estimation are shown in Figure 5.23. The data are only shown when there is no occlusion due to reflected modes. Results indicate percent errors less than 4% and 6%, respectively, in both arrival time and velocity domains. Note the larger slope between arrival time and velocity estimate error for receiver one. Shorter transducer separation will increase the error in velocity with respect to error arrival time; longer spaced transducers will show a decreased slope. See the slope comparison between both P-wave sub-figures. The system is best able to estimate the S-wave velocity using the data collected at receiver two, with errors generally below 2%.

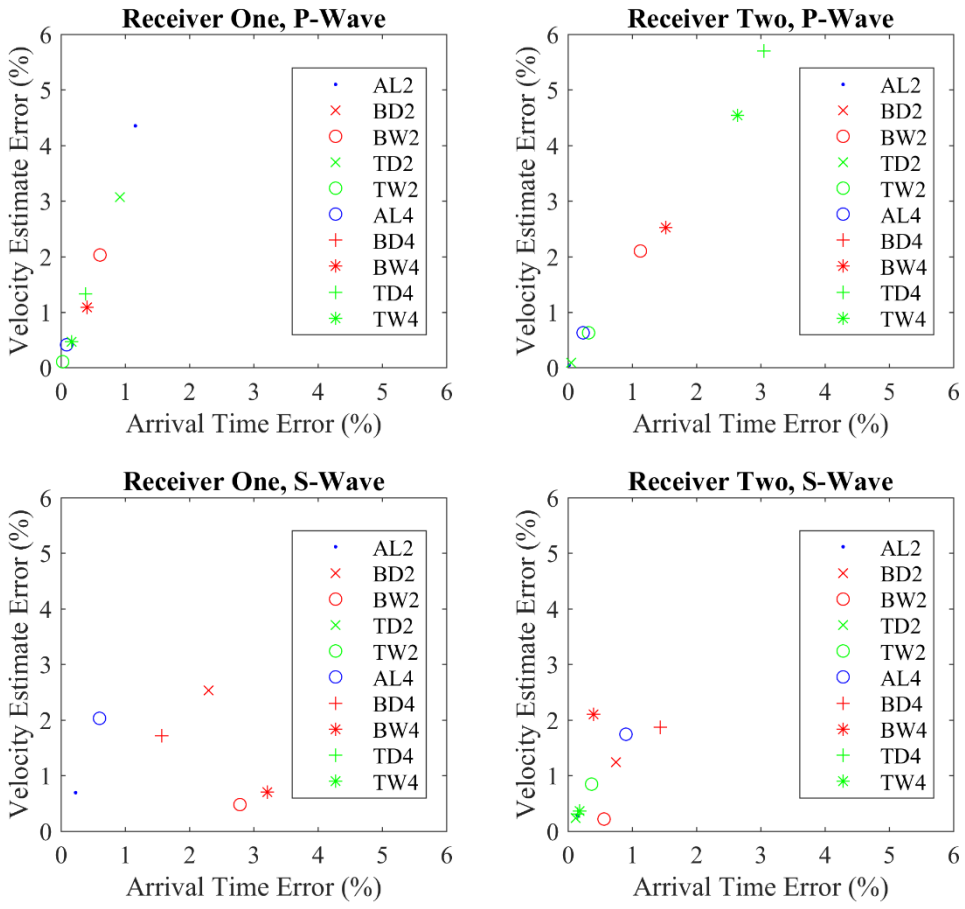

Figure 5.23: Velocity estimate vs. arrival time error for all samples for both P and S-waves at each receiver. All measurements and velocity estimates are approximately within 5% of the true parameters.

Chapter 6: Conclusions and Future Work

6.1 Conclusions

The main purpose of this research is to better understand alternative methods to ultrasonically examine rock samples, with a focus on full-core acoustic analysis. Forward modeling of both the cross-diameter P-wave and refracted P and S-wave techniques allows for isolation of the relevant arrivals and proper understanding of the entire physical system. Additionally, the forward models are easy to custom tailor to any sized transducer and system geometry so long as the principals of acquisition are the same. Model utility is largely dependent on how well the initial conditions of the experiment are measured.

Data for the cross-diameter P-wave analysis suggest that there is an ideal minimum amount of fluid required to properly couple the energy to the sample and highlight the need for using larger diameter samples and/or smaller transducers, if possible. Measurements acquired on both dry and fully water saturated core samples agree with the results as predicted by Gassmann's fluid substitution theory, but suggest that the conventional wisdom of placing the transducers against the sample directly at the sample mid-plane may not be the best when using these transducers due to improper coupling.

Results from the refracted wave tests are ideal for all samples tested, with errors in velocity estimation consistently below 6%. The data sometimes show interference of the direct fluid arrival and occlusion due to reflection for the first receiver for samples with slower acoustic velocities. In some cases, the velocities approach the velocity of water. The use of a second receiver spaced further away from the source enhances isolation of the relevant wave modes. The method is accurate for analyzing rock properties as long as the user can properly understand the different wave arrivals shown. The techniques are valid for slow formations if the fluid and reflected modes are properly isolated—which is largely achieved by the second receiver. Overlain raw waveform data with forward model

predictions is critical for analytical consistency. The forward model acts as a reality check for the user to either repeat the experiment or double check the model conditions should model disagreements arise.

6.2 Future Work

The results would benefit from corroboration using smaller and preferably higher powered transducers. Smaller transducers would reduce the effects of sample curvature and, most importantly, increase the resolution of the system. The cross-diameter P-wave results as a function of transducer height should be repeated at a constant transducer separation that is larger than the sample diameter. This would allow for ample fluid to exist between the transducer and sample and perhaps eliminate the odd result that +0.2 in is the optimal position to place the transducer center. As for the refraction experiments, recall that 8 in long samples were used. This was the minimum length that three of the selected transducers could be setup to analyze samples as an array due to their large size. The local resolution in length is therefore about 4 in for each receiver. An array of smaller receivers would be more effective. This would also allow for conventional coherence stacking analysis of the waveforms.

Going forward, it would be possible to rotate the core sample to collect data circumferentially around the sample to provide a better picture of the system anisotropy and heterogeneity. However, considering the large number of individual waveforms measured for these experiments when only studying one side of the core, there is a need for automation. The 3D printed prototypes were a first step in that direction, without which these experiments would approach infeasibility due to the time required to properly orient and align the transducers. It would not be a stretch to design a system that incorporates stepper motors to automatically position the transducers for each iteration. In the same light, the transducers themselves may automatically measure and calibrate transducer-

sample separation by measuring a so-called “pitch-catch” reflection off of the sample. The overall system is ripe for optimization, but more work needs to be done regarding proper transducer selection and understanding the relative depth of investigation into the core samples. Recall that the forward model predicts the presence of refracted waves, which suggest a minimal depth of investigation. There are other body waves present that may be analyzed later in the wave train, but these require more complex modeling methods to predict and understand.

There is also the opportunity to study amplitude vs. offset akin to modern seismic analysis. This should allow direct insight into the sample P and S-wave velocity via the Zoeppritz equations, which greatly reduces the complexity of analysis, as the amplitude of the reflection as a function of angle is the only pertinent variable (Zoeppritz, 1919). Indeed, this system was designed and studied, but the data thus far suggest counter-intuitive results. The trends predicted by the Aki-Richard’s approximation are shown as solid lines in Figure 6.1 (Aki and Richards, 1980). Tests on 4 in OD aluminum show a trend similar to the theory, but the rock trends (plus signs) do not agree. Flat rock samples (crosses) show a much more improved response. The system requires further study to reduce curvature effects on amplitude reduction. But even so, the fact that the trends are appropriate for aluminum but seemingly opposite for the rocks is puzzling. As concluded previously, smaller transducers are potentially the solution. This method of analysis remains under active research.

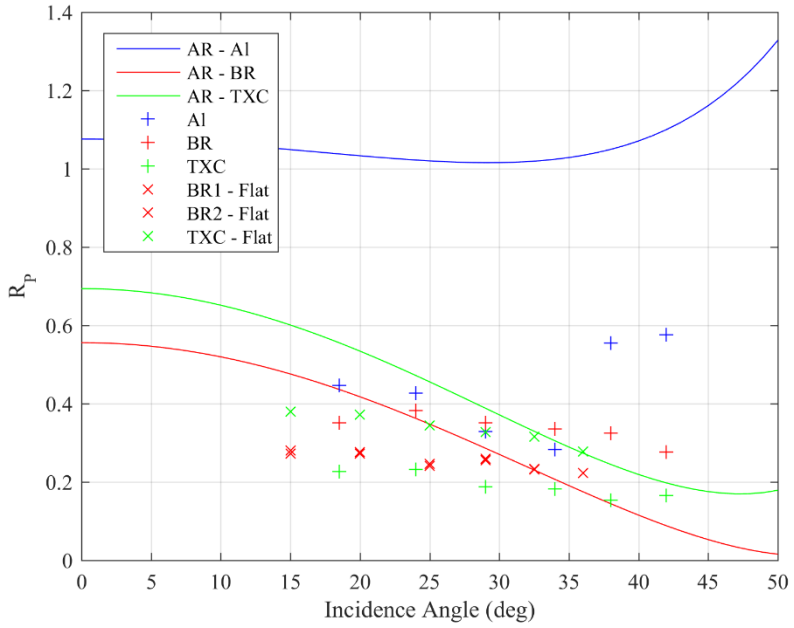

Figure 6.1: Attenuation corrected reflection coefficient, R_P ,vs. incidence angle with Aki-Richards Approximation for 4 in OD (+) and 2x2x3 in rectangular prism (x) samples.

Appendices

Appendix A: Aluminum waveforms, 2 in OD

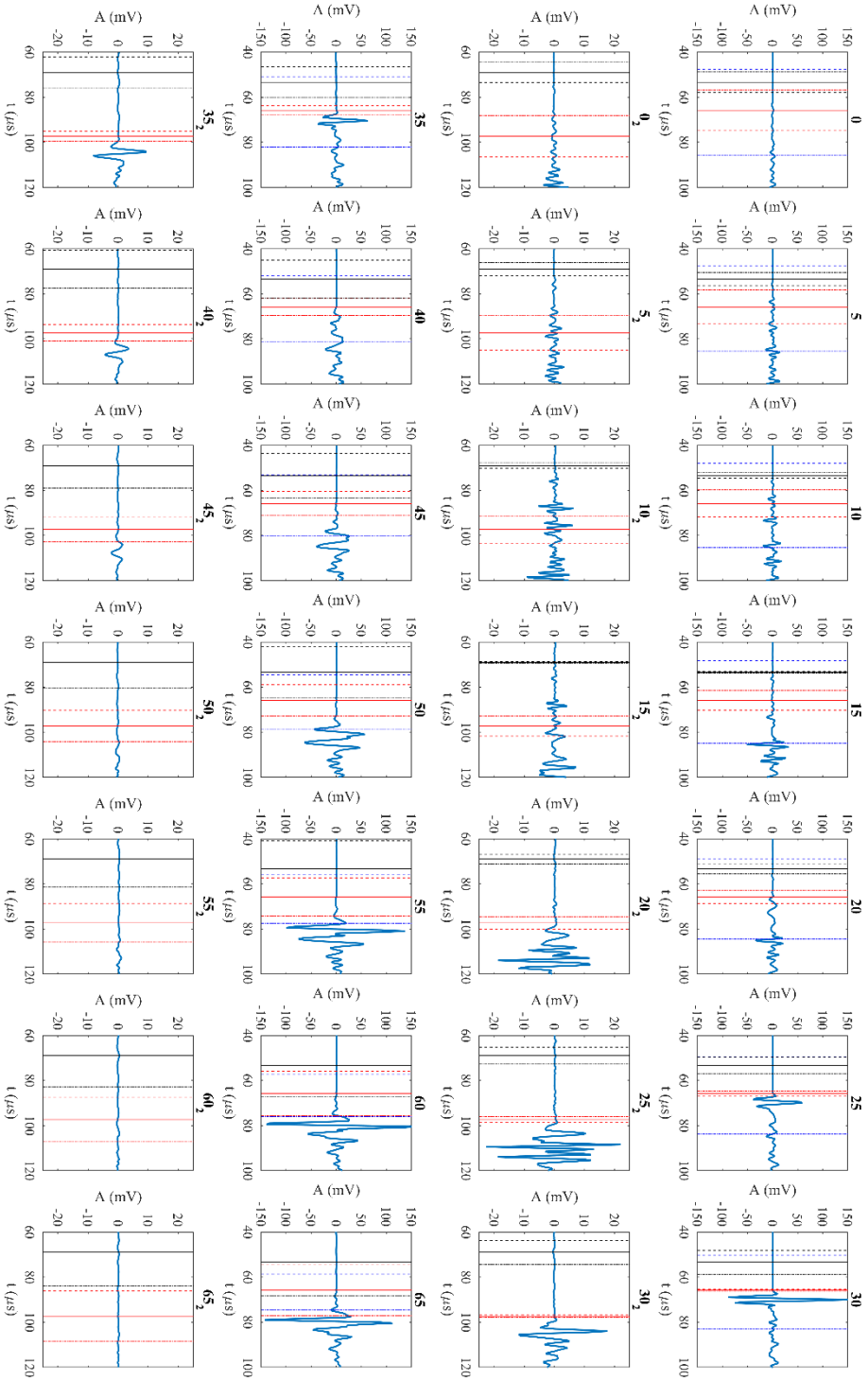

Appendix B: Aluminum waveforms, 4 in OD

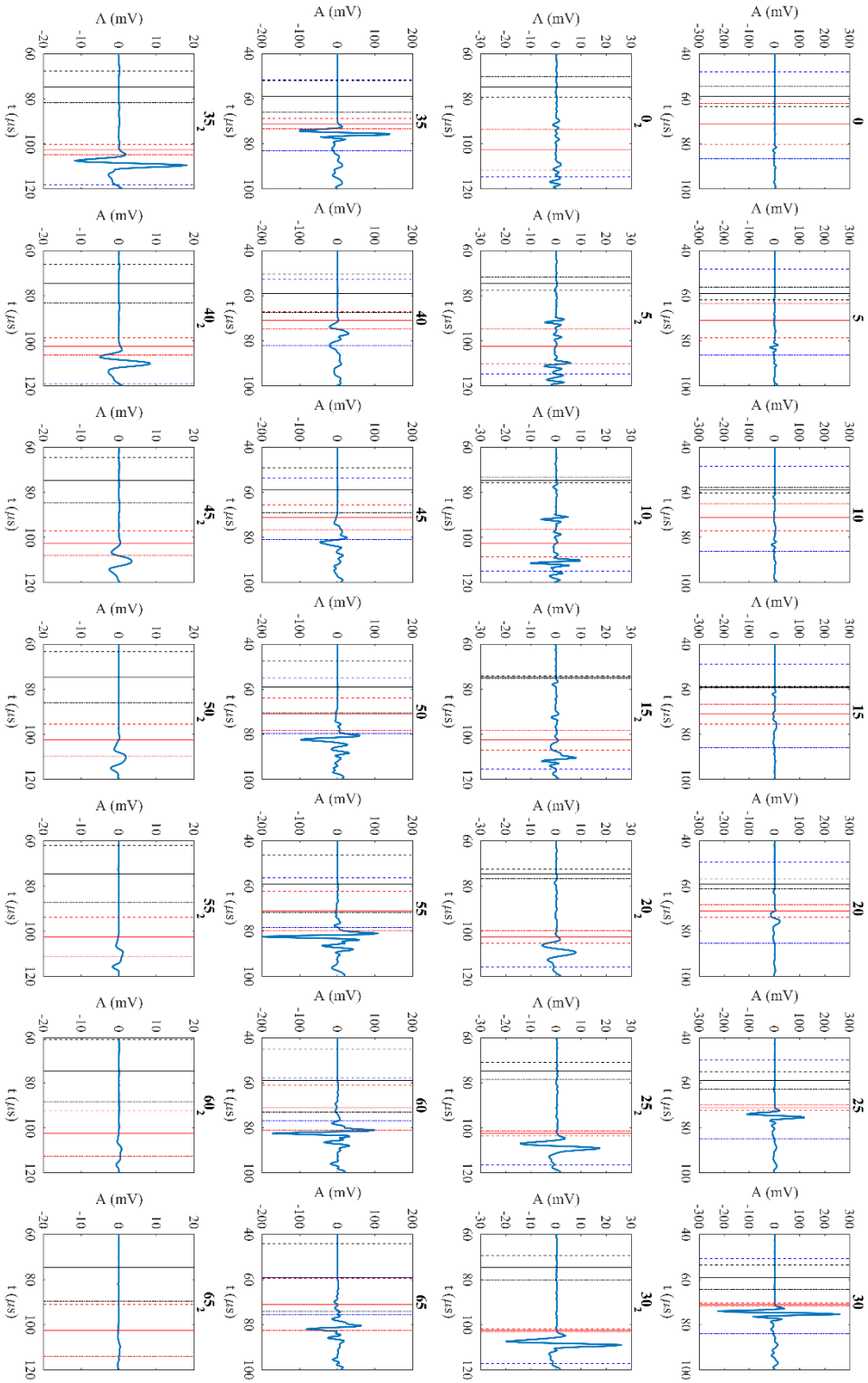

Appendix C: Dry Berea sandstone waveforms, 2 in OD

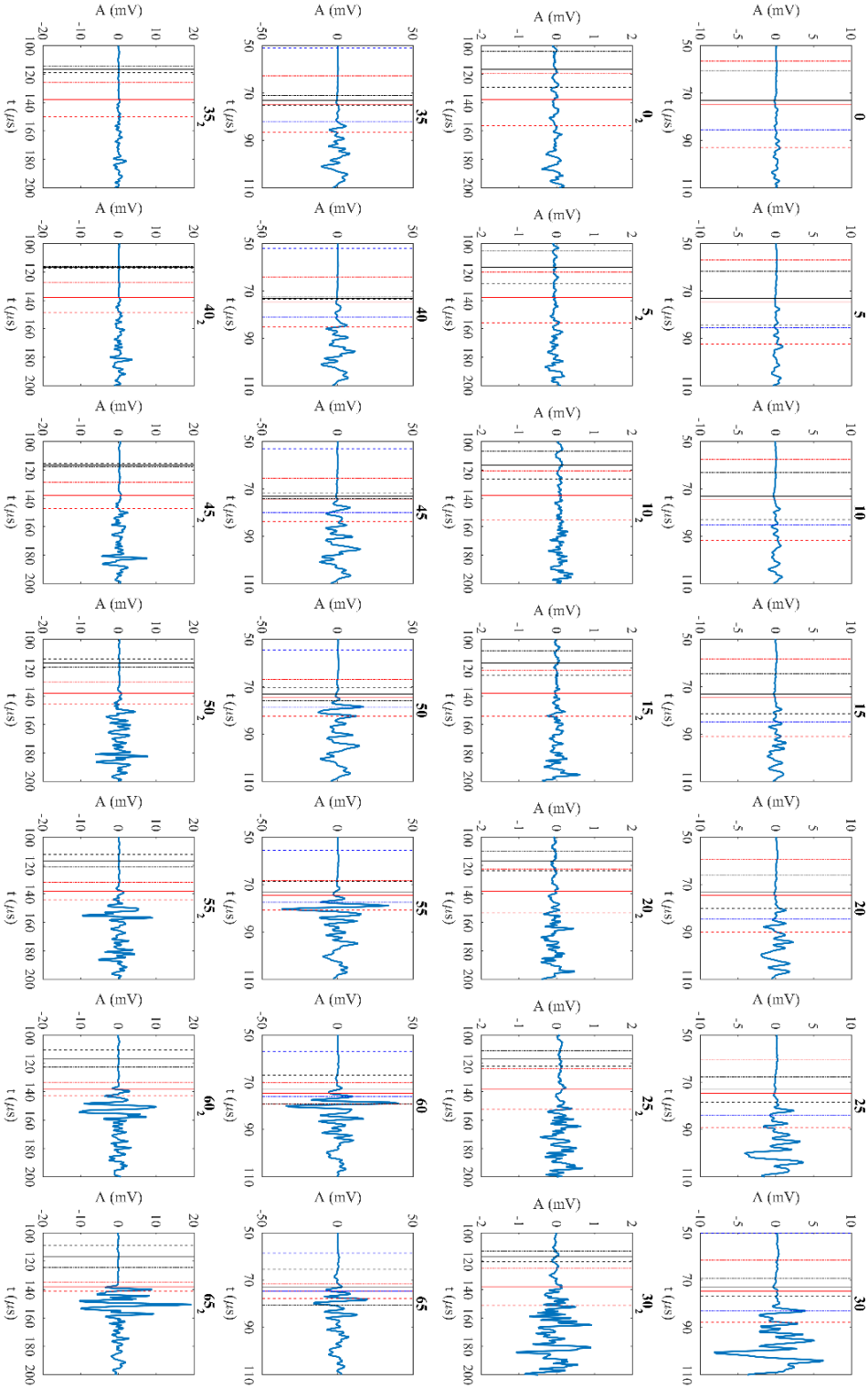

Appendix D: Dry Berea sandstone waveforms, 4 in OD

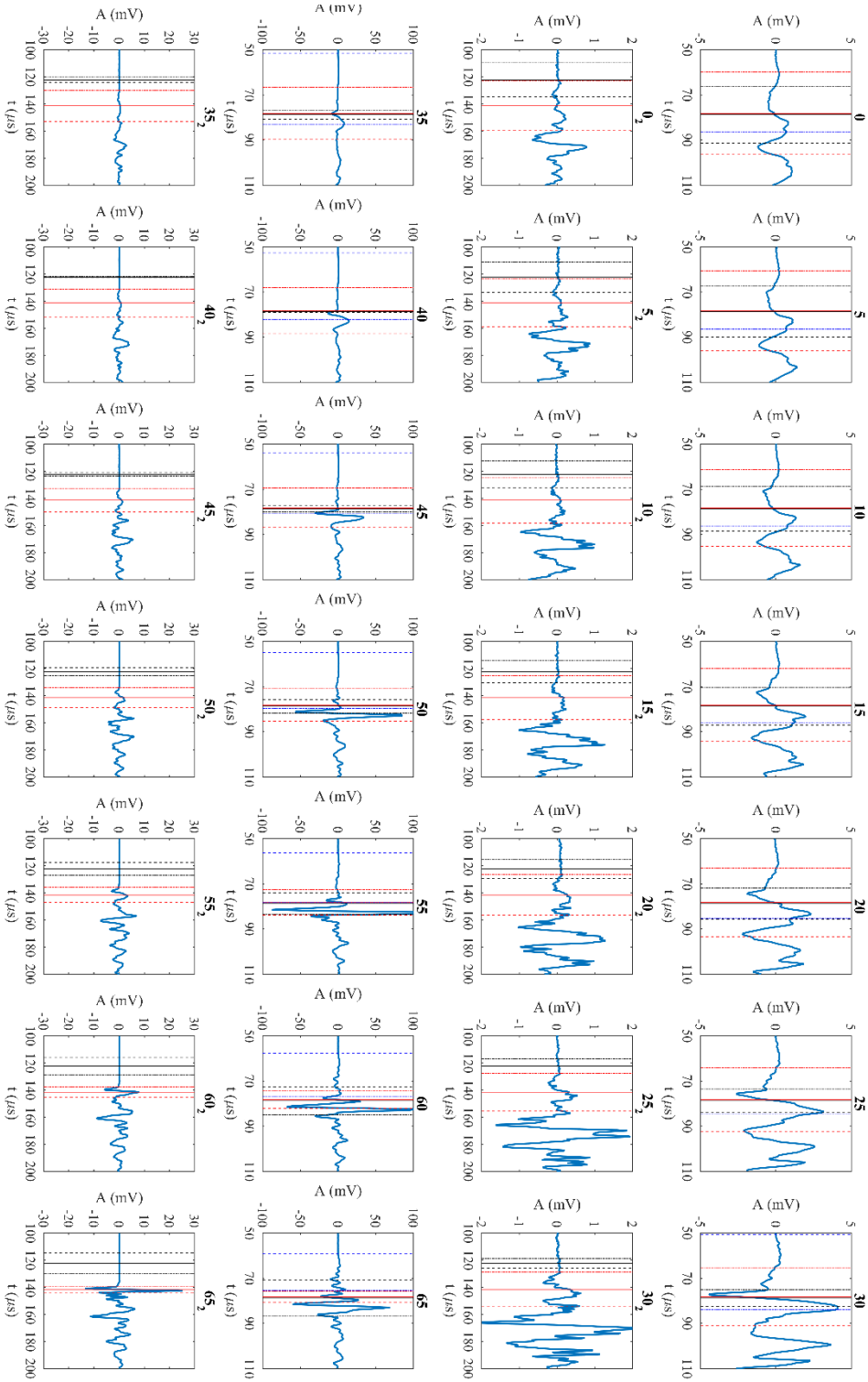

Appendix E: Saturated Berea sandstone waveforms, 2 in OD

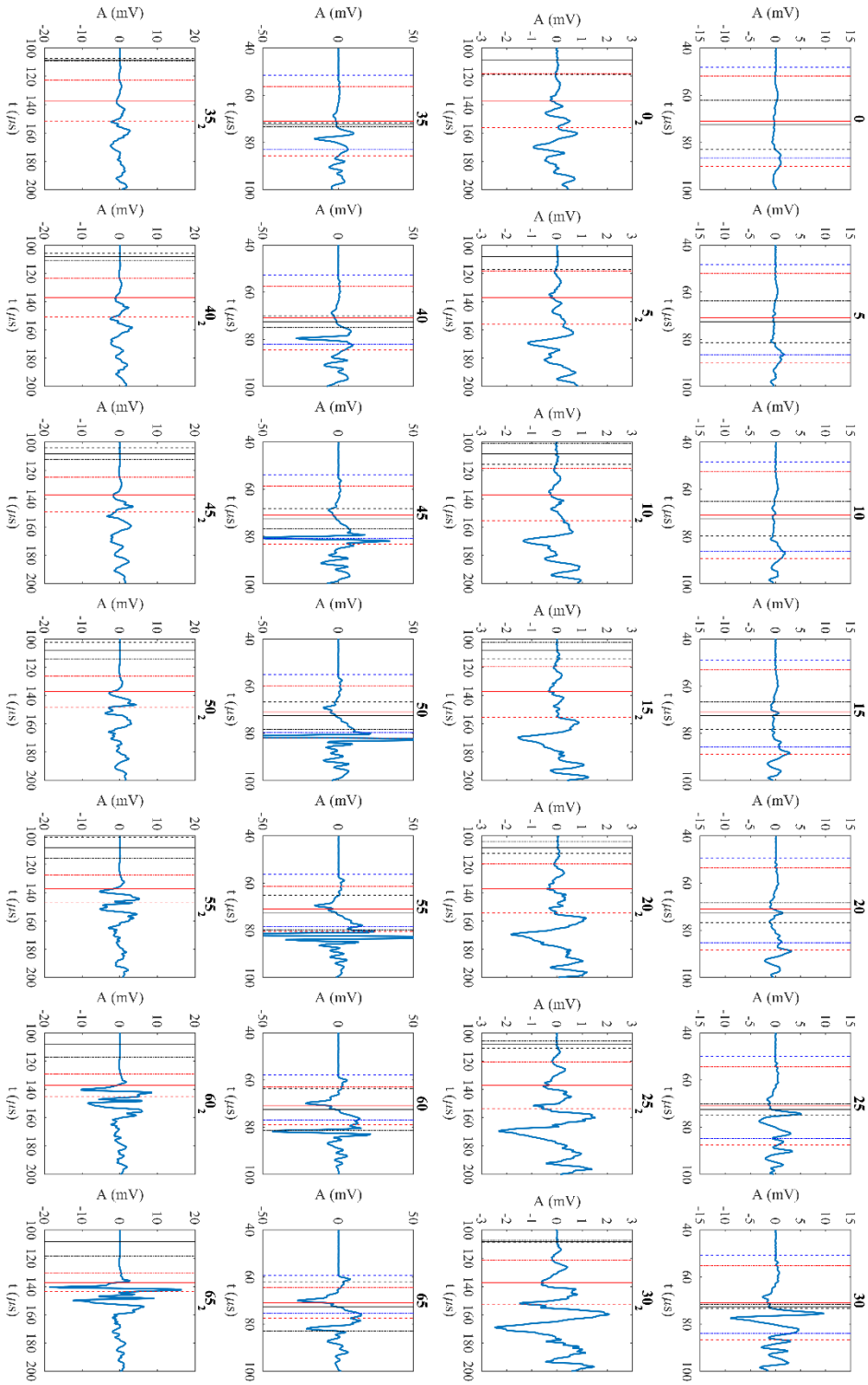

Appendix F: Saturated Berea sandstone waveforms, 4 in OD

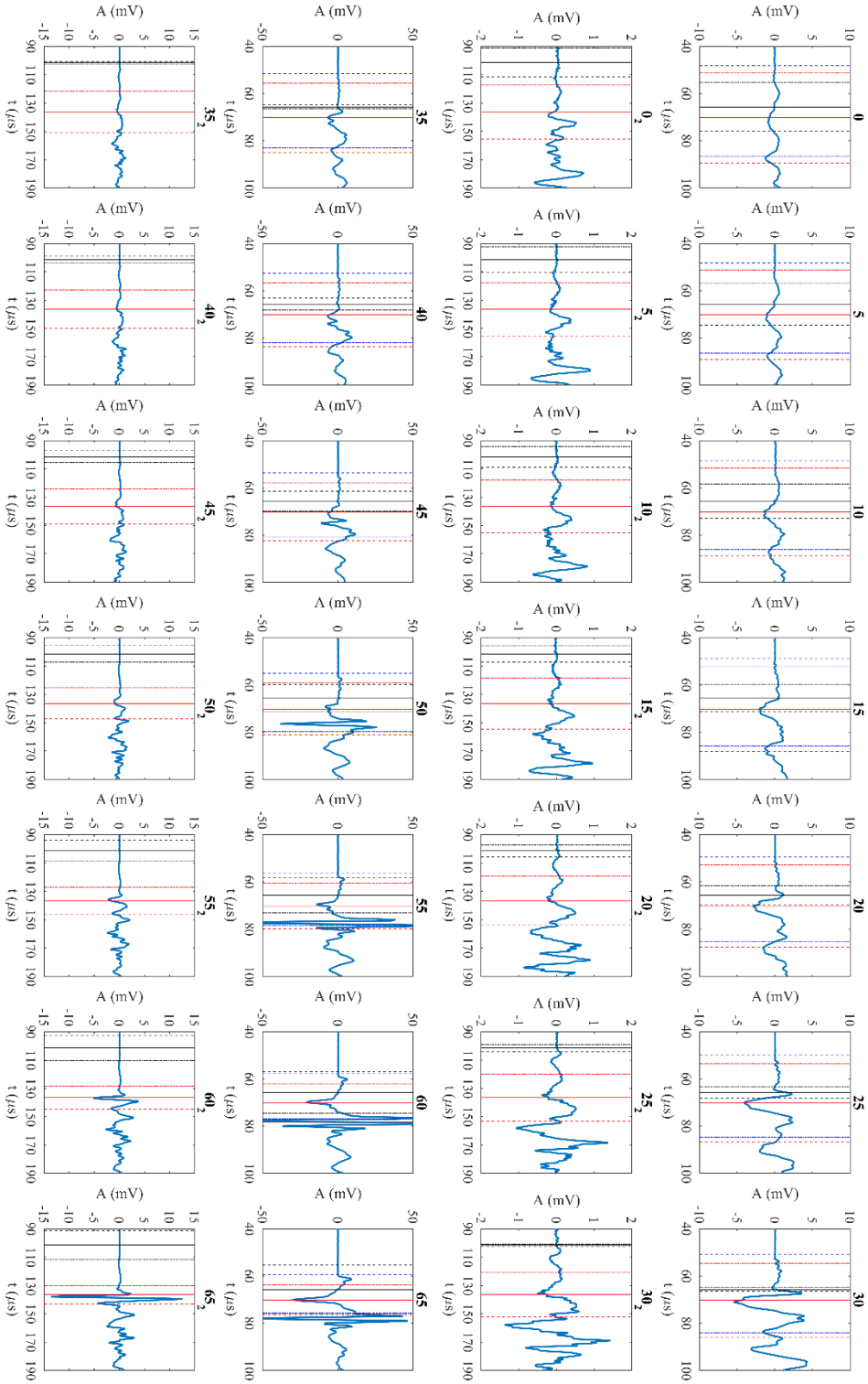

Appendix G: Dry Texas Cream limestone waveforms, 2 in OD

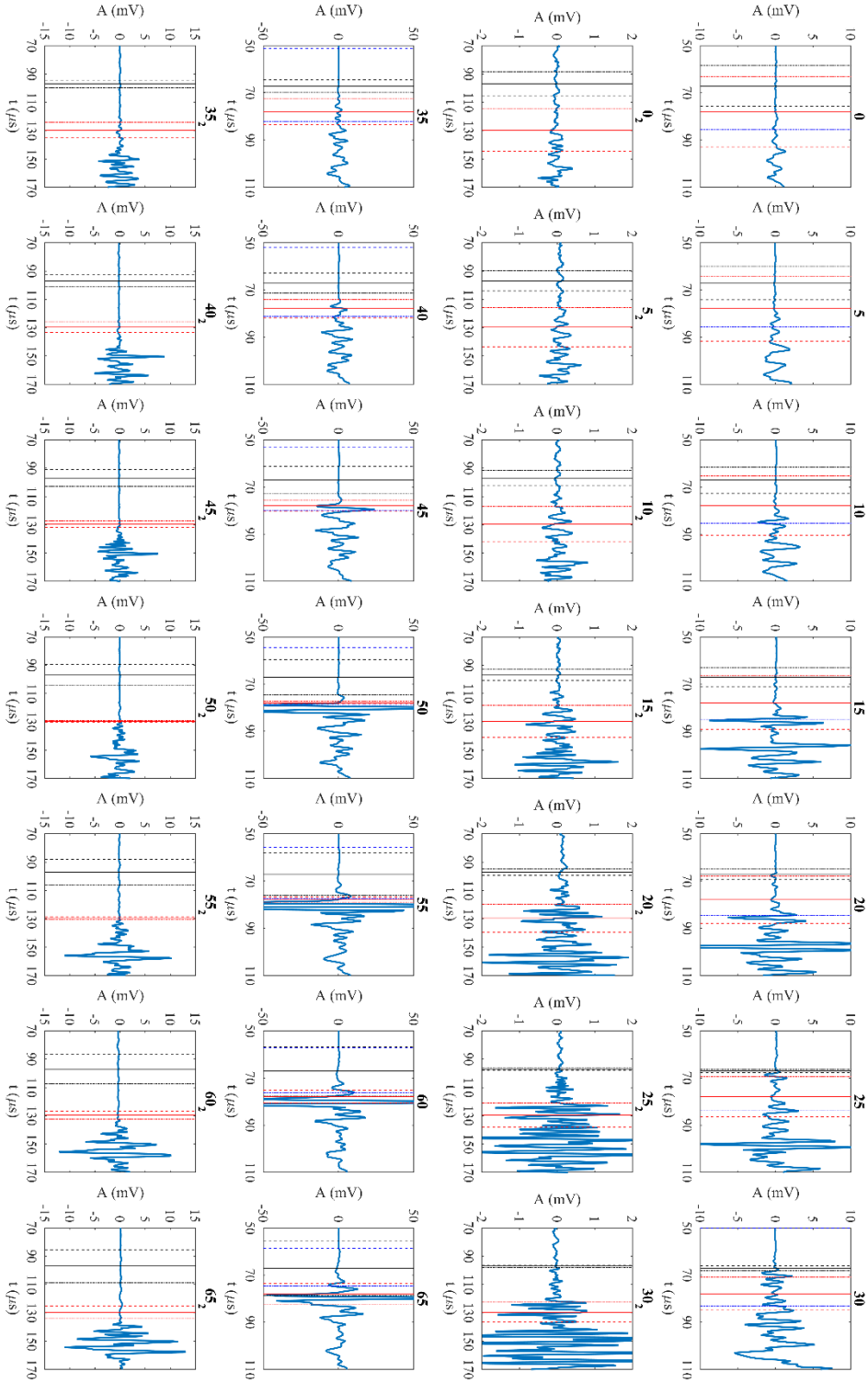

Appendix H: Dry Texas Cream limestone waveforms, 4 in OD

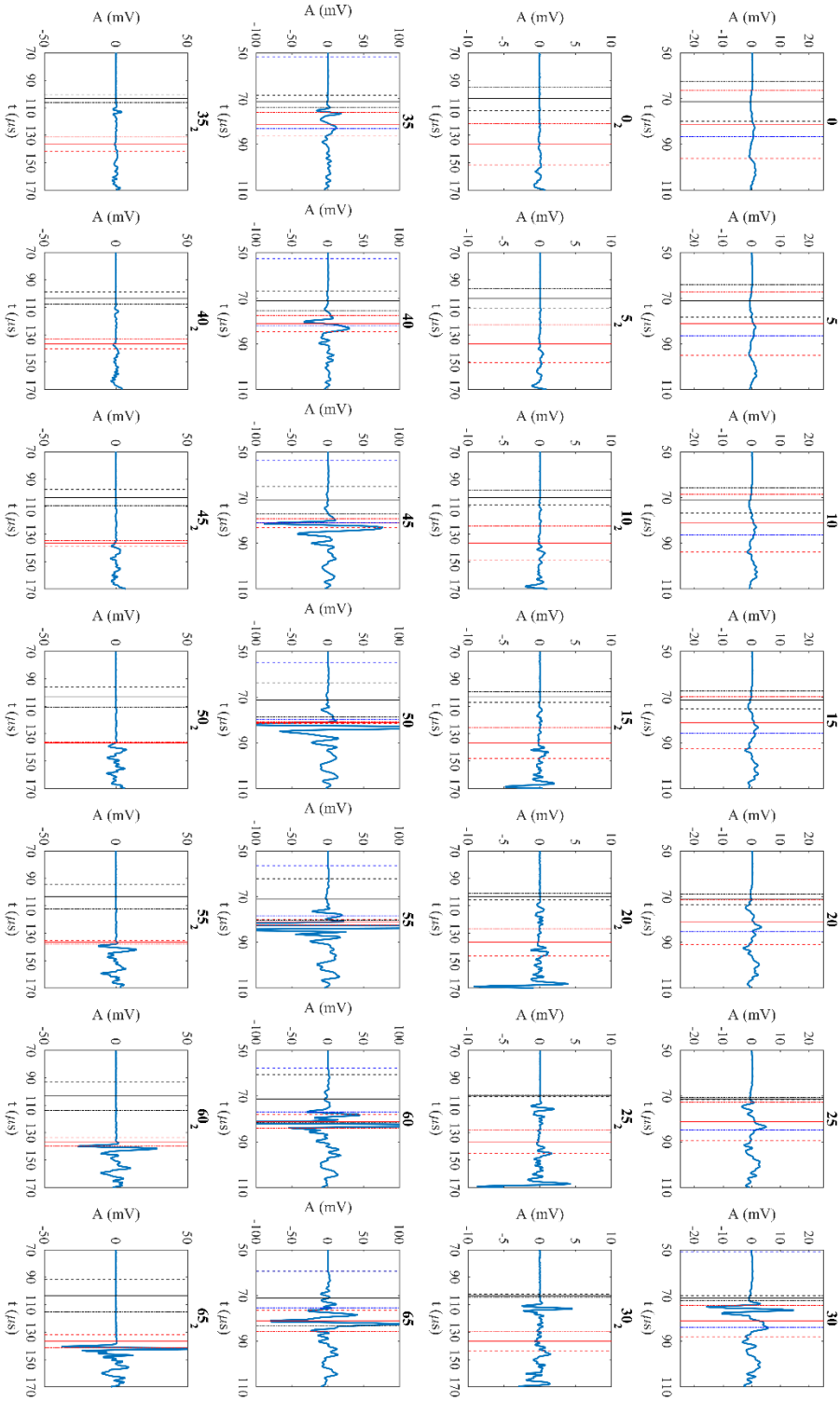

Appendix I: Saturated Texas Cream limestone waveforms, 2 in OD

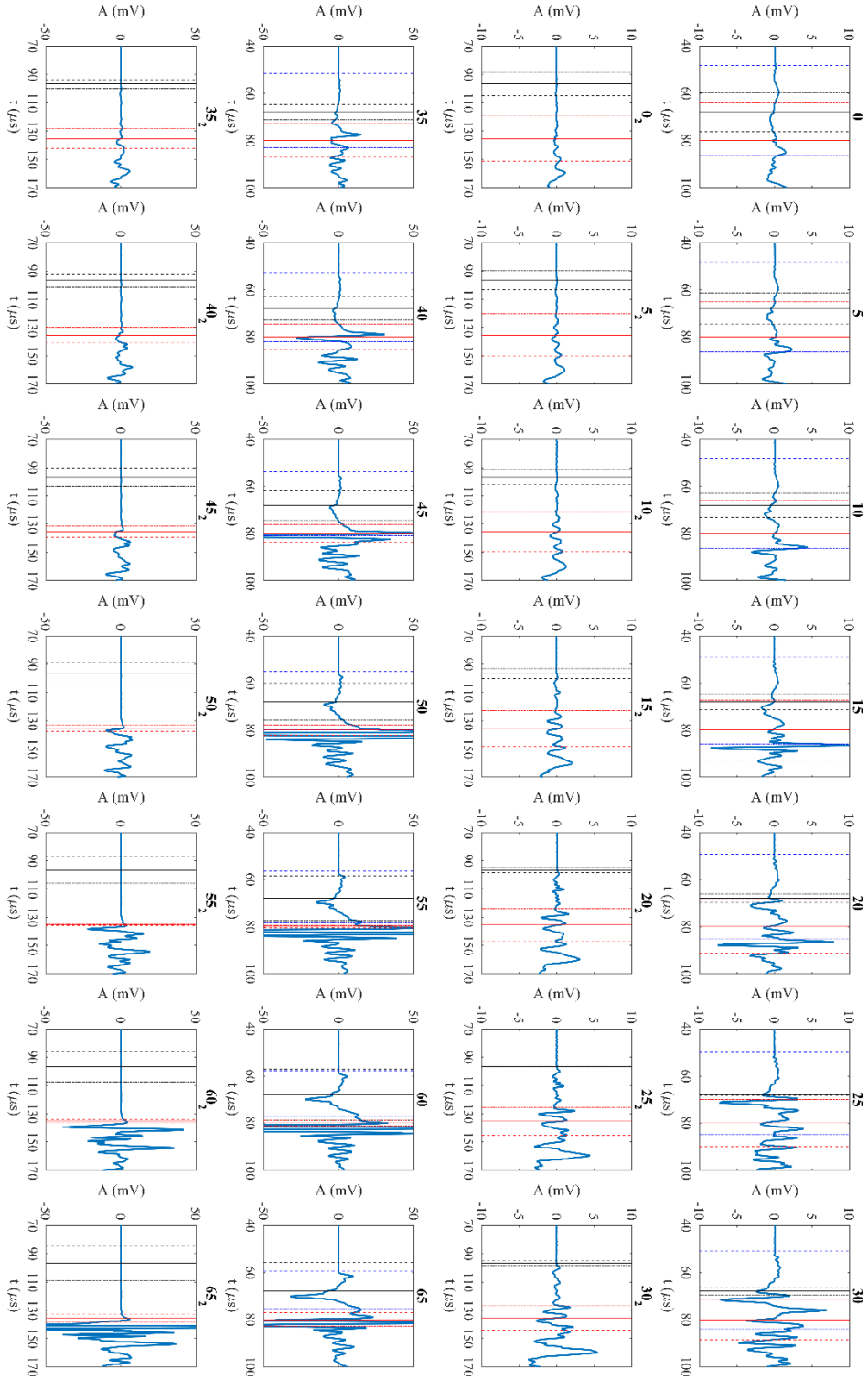

Appendix J: Saturated Texas Cream limestone waveforms 4 in OD

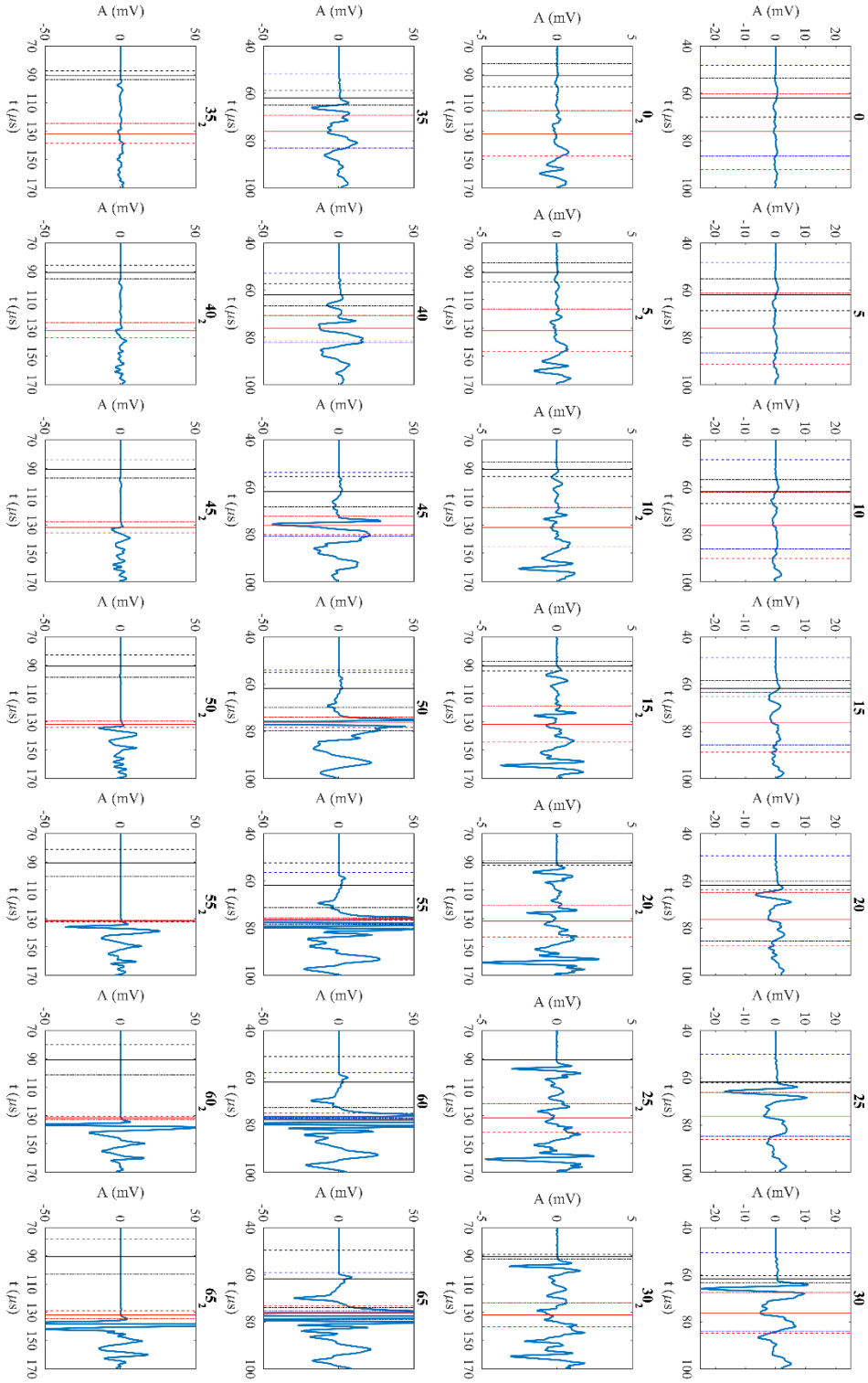

References

Aki, K. and Richards, P. G., 1980, Quantitative seismology: Theory and Methods, Vol. 1: W. H., Freeman & Co.

ASTM D2845-08, Standard Test Method for Laboratory Determination of Pulse Velocities and Ultrasonic Elastic Constants of Rock (Withdrawn 2017), ASTM International.

Berryman, J. G. 1999, Origin of Gassmann's Equations, *Geophysics* 64.5:1627-629, DOI**:** 10.1190/1.1444667.

Cerri, R., Di Martino, S., Balossino, P., Gioacchini, L., Colombo, I., Spelta, E., Bartosek, M., and Bjorum, M., 2015, Combined Application of Pressure Coring and Desorption Analysis for Barnett Shale Gas Evaluation, *SPE Middle East Unconventional Resources Conference and Exhibition*, 26-28 January, Muscat, Oman.

Geotek Ltd., Geotek P-Wave Sensor Technology, http://www.geotek.co.uk/products/arc/

Haldorsen, J. B.U., Johnson, D. L., Plona, T., Sinha, B., Valero, H. P., and Winkler, K., 2006, Borehole Acoustic Waves, *Oilfield* Review **18** (1), Schlumberger.

Kovari, K., Tisa, A., Einstein, H., and Franklin, J., 1983, Suggested Methods for Determining the Strength of Rock Materials in Triaxial Compression: Revised Version, *International Journal of Rock Mechanics and Mining Sciences and Geomechanics Abstracts* **20** (6): 285-290. DOI: 10.1016/0148-9062(83)90598-3

RP 40*, Recommended Practices for Core Analysis*, 2nd Edition 1998, API.

Schultheiss, P. J., Francis, T. J. G., Holland, M., Roberts, J.A., Amann, H., Thjunjoto, Parkes, R. J., Martin, D., Rothfuss, M., Tyunder, F., and Jackson, P.D., 2006, Pressure Coring, Logging and Subsampling with the HYACINTH System, *Geological Society, London, Special Publications* **267** (1): 151-63.

Stokoe, K. H., II, Joh, S. H., and Woods, R. D., 2004, Some Contributions of in Situ Geophysical Measurements to Solving Geotechnical Engineering Problems*, International Conference on Site Characterization*, 19-22 September, Porto, Portugal.

Ultrasonic Velocity Table, Advanced NDT Ltd., http://www.advanced-ndt.co.uk/index_htm_files/Reference%20Chart%20-%20Velocity%20Chart.pdf

Weidinger, D. M. 2008, *Laboratory analysis of small strain moduli in compacted silts*, MS Thesis, Paper 6834, Missouri University of Science and Technology, Rolla, Missouri.

Yale, D. P., and Jameison, W.H. Jr., 1994, Static and Dynamic Rock Mechanical Properties in the Hugoton and Panoma Fields, Kansas, SPE Mid-Continent Gas Symposium, Amarillo, Texas, May 22-24. DOI:10.2118/27939-MS.

Yun, T.S., Narsilio, G.A., Santamarina, J.C., and Ruppel, C., 2006, Instrumented pressure testing chamber for characterizing sediment cores recovered at in situ hydrostatic pressure, *Marine Geology* **229** (3): 285-293.

Zoeppritz, K., 1919, Erdbebenwellen VIIIB, Ueber Reflexion and Durchgang seismischer Wellen durch Unstetigkeitsflaechen: Goettinger Nachrichten, I, 66-84.